CARBON ALLOTROPE DEPENDENCE ON TEMPERATURE AND PRESSURE DURING THERMAL DECOMPOSITION OF SILICON CARBIDE

THESIS

Munson J. Anderson, Captain, USAF

AFIT-ENG-14-M-07

DEPARTMENT OF THE AIR FORCE
AIR UNIVERSITY

AIR FORCE INSTITUTE OF TECHNOLOGY

Wright-Patterson Air Force Base, Ohio

AFIT-ENG-14-M-07

CARBON ALLOTROPE DEPENDENCE ON TEMPERATURE AND PRESSURE DURING THERMAL DECOMPOSITION OF SILICON CARBIDE

THESIS

Presented to the Faculty

Department of Aeronautics and Astronautics

Graduate School of Engineering and Management

Air Force Institute of Technology

Air University

Air Education and Training Command

In Partial Fulfillment of the Requirements for the

Degree of Master of Science in Electrical Engineering

Munson J. Anderson, BS

Captain, USAF

March 2014

AFIT-ENG-14-M-07

CARBON ALLOTROPE DEPENDENCE ON TEMPERATURE AND PRESSURE DURING THERMAL DECOMPOSITION OF SILICON CARBIDE

Munson J. Anderson, BS

Captain, USAF

Approved:

_____// Signed //_____	__21 Feb 2014__
Michael C. Pochet, Maj, USAF (Chairman)	Date
_____// Signed //_____	__21 Feb 2014__
Dr. John J. Boeckl (Member)	Date
_____// Signed //_____	__21 Feb 2014__
Dr. Ronald A. Coutu, Jr. (Member)	Date

Abstract

Bulk carbon nanotube (CNT) films and graphene films form on silicon carbon (SiC) using a metal-catalyst-free thermal decomposition approach. In this work, the background vacuum pressure and temperature used in the decomposition process are varied to investigate their impact on the type and quality of carbon allotrope formed on the SiC substrate. The carbon nanostructure growth is performed using two approaches, both of which involve intense heating (1400-1700°C) and moderate vacuum conditions (10^{-2} – 10^{-5} Torr) without the aid of carbon rich feed gases or metal catalyst commonly used in Chemical Vapor Deposition (CVD) growth approaches. The first growth method uses a conventional graphite resistance furnace capable of annealing wafer-scale samples over 1700°C under vacuum. Using this approach, post-growth characterization is performed using both scanning electron microscopy and Raman spectroscopy. The second growth approach uses a high-intensity laser to apply heat to a micro-meter scale spot size on the SiC substrate. The high-intensity laser heats the illuminated area of the SiC substrate while under vacuum conditions, resulting in a small-scale growth process similar to the conventional resistance furnace technique. Unique to this micro-scale approach is that in-situ Raman spectroscopy is performed yielding instantaneous characterization of the resultant carbon nanostructure from the thermal decomposition of the SiC substrate.

Given the arduous nature of the growth and characterization of films formed using the furnace based approach, this work focuses on using the laser-induced growth technique to refine ideal growth parameters of bulk nanostructure films. The laser-

induced growth mechanism enables the impact of varied background vacuum pressures and temperatures to be evaluated in-situ, with the possibility to evaluate hundreds of parameter sets. This work reports the results and findings for various parameter sets implemented during growth, and provides insight into the physical mechanism influencing the growth process.

Table of Contents

Acknowledgments

I would like to express my sincere appreciation to my faculty advisor, Major Michael Pochet, for his guidance and support throughout the course of this thesis. I would also like to thank my committee members Dr. Ron Coutu and Dr. John Boeckl for their insight and laboratory resources. The experience and technical knowledge offered by AFIT cleanroom technicians, Mr. Rich Johnston and Mr. Tom Stevenson, were instrumental in processing samples and are greatly appreciated.

Lastly, I would like to thank my lovely wife. Your support, patience and encouragement proved to be the critical variable in the successful completion of this endeavor.

Munson J. Anderson

List of Figures

List of Tables

CARBON ALLOTROPE DEPENDENCE ON TEMPERATURE AND PRESSURE DURING THERMAL DECOMPOSITION OF SILICON CARBIDE

I. Introduction

1.1 Chapter Overview

The purpose of this chapter is to highlight the importance of understanding carbon nanotube (CNT) growth mechanics during thermal decomposition of silicon carbide (SiC), as well as to give an overview of the research methodology presented in this thesis. The background section briefly discusses the chemical and physical properties of graphene and CNTs. The problem statement section declares the main problem this research effort is focusing on; how temperature and pressure determine physical characteristics of carbon nanostructures (graphene and CNTs). The scope, limitations and assumptions section discusses means to simplify growth experiments, such as excluding water concentration and chamber gasses present in the chambers, and summarizes previous research efforts. The methodology section describes key processes required to produce relevant data, including assumptions used to develop the experimental processes implemented in this research effort. In the analysis and results section, key findings discovered during this research are discussed. Lastly, the thesis structure section outlines the contents of the following thesis chapters.

1.2 Background

Silicon has been the standard material from which microchips have been fabricated for over 50 years. During that time: electronic device size has decreased, power consumption has decreased, while processing speed has increased. For example,

1

some smart phones today are faster and more powerful than computers that were made five to ten years ago. These properties evolved as a result of improved lithographic and etching processes used in the fabrication of microchips. Microchips are comprised of tiny transistors that act like switches. These transistors regulate the flow of electrons enabling signal amplification, and the realization of silicon carbide blocks, and memory states. There are two important factors which determine the speed of a chip: feature size and material properties. The physical size of the features that the electrons need to pass through is directly proportional to the speed at which the electrons can move from one area to another. The smaller the transistors are, the faster the electrons can flow through the chip, allowing a functional block of transistors on a microchip to operate more quickly. In addition to the physical size of a device, the material from which it is made also affects its operational speed.

The electrical conductivity of a given material determines whether it is a metal, insulator or semiconductor. Electrical conductivity (σ) is defined as a material's ability to conduct an electrical current and is measured in Siemens per meter (S/m) [1]. At room temperature, metals have high conductivities (Ag = 6.3 x 10^7 S/m [1]), insulators have low conductivities (rubber = 10^{-14} S/m [1]), and conductivity values for semiconductors are found between metals and insulators (1.56 x 10^{-3} S/m [1]). A key characteristic parameter of a crystal structure, electron mobility (μ), is defined as how quickly an electron can move through a semiconductor when an electric field is applied, and is measured in (cm^2 $V^{-1}s^{-1}$). Equation (1-1) defines mobility as drift velocity (v_d) divided by the applied electric field (E) [2].

$$\mu = \frac{v_d}{E} \tag{1-1}$$

With a large dependence on temperature and doping characteristics, the mobility of semiconductors can vary by a factor of ten. Silicon at room temperature, for instance, has an electron mobility ranging from 1424 to 115 cm^2 V^{-1}s^{-1}, given a phosphorus doping concentration ranging from 10^{13} to 10^{19} cm^{-3}, respectively [2]. Equation (1-2) provides a means to relate the electron (or hole) mobility (μ_e or μ_h) of a given semiconductor at room temperature, to its electrical conductivity, while considering its dopant concentration (n or p) [2].

$$\sigma = ne\mu_e \ \ OR \ \ \sigma = pe\mu_h \tag{1-2}$$

As previously stated, temperature effects must be considered when calculating a semiconductor's electron mobility. Numerical examples provided thus far only relates to Si at room temperature. During normal operation, though, Si tends to heat up, causing an increase in lattice vibrations, which in turn impedes the movement of free electrons [2]. Equations (1-3) and (1-4) are used to calculate electron (or hole) mobility in Si based on total dopant concentration (N) at a given temperature (T_n = T/300 with T measured in Kelvin) [2].

$$\mu_n = 88 \ T_n^{-0.57} + \frac{1250 \ T_n^{-2.33}}{1 + \left[\frac{N}{1.26 \times 10^{17} \ T_n^{2.4}}\right] 0.88 \ T_n^{-0.146}} \tag{1-3}$$

$$\mu_p = 54.3 \ T_n^{-0.57} + \frac{407 \ T_n^{-2.33}}{1 + \left[\frac{N}{2.35 \times 10^{17} \ T_n^{2.4}}\right] 0.88 \ T_n^{-0.146}} \tag{1-4}$$

Given silicon's mobility, combined with industries smallest features, today's computer processing speeds have reached their maximum limit of 5 GHz [3]. While this

is sufficient for today's applications, future commercial and military applications will undoubtedly require faster microchip speeds, operating well beyond 5 GHz. Today, microwave devices in the GHz bands are required for frequency agile radar and communication, and are commonly based on higher mobility group III-V semiconductor material [4]. That being said, even today's "fast" III-V materials have their limitations. Two dimensional carbon nanostructures, namely CNTs and graphene, have extraordinary electrical properties [5]. In order to reach faster speeds required for future applications, graphene and CNTs are being examined as replacements for silicon. Other high mobility materials under use and continued development include GaN, GaAs, and InGaAs [2].

Of the various allotropes of carbon that exist, diamond and graphite are the most common [6]. Extensive research and experiments have been done on these allotropes for more than 200 years. In 1772, Antoine Lavoisier showed that diamonds are a form of carbon by burning samples of charcoal and diamonds, and found that both released the same amount of carbon dioxide per gram [6]. Carl Wilhelm Scheele carried out a similar experiment with graphite in 1779, disproving prior thoughts that graphite had been a form of lead [7]. Michael Faraday (1820), William and Lawrence Bragg (1913), John D Bernal (1922) and Kathleen Lonsdale (1966) also had important contributing experiments which furthered the knowledge of carbon. However, it was not until 1985 when Richard Smalley, Robert Curl and Harry Kroto discovered the first all-carbon molecule, did a new allotrope get discovered [8].

Carbon – 60 (C_{60}), as shown in Figure 1, was the first fullerene, a molecule made entirely of carbon, to be discovered since Lavoisier's experiments in 1772. C_{60}, Buckminsterfullerene, or "bucky ball", is a soccer ball shaped molecule with 60 carbon

atoms bonded together in pentagons and hexagons [6]. This discovery sparked interest within the science community, which led to a surge of research, experiments, conferences and workshops. In 1990, at a carbon-carbon composites workshop, Smalley proposed the existence of a tubular fullerene [8]. In August of 1991, Mildred Dresselhaus followed up in an oral presentation in Philadelphia, at a fullerene workshop, on the symmetry proposed for carbon nanotubes capped at either end by fullerene hemispheres. Experimental evidence of the existence of carbon nanotubes came in 1991 when Sumio Iijima imaged multiwalled carbon nanotubes (MWCNTs) using a transmission electron microscope (TEM) as shown in Figure 2 [9].
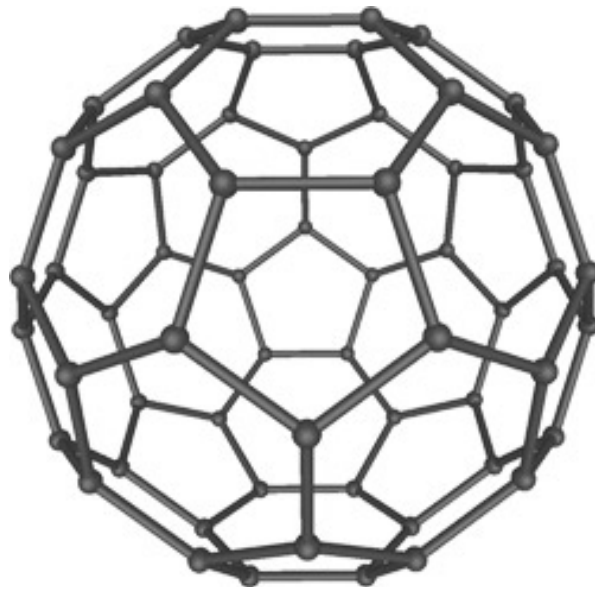
Figure 1 – Model of the C60 fullerene. It is composed of 60 carbon atoms arranged in 20 hexagons and 12 pentagons [5].
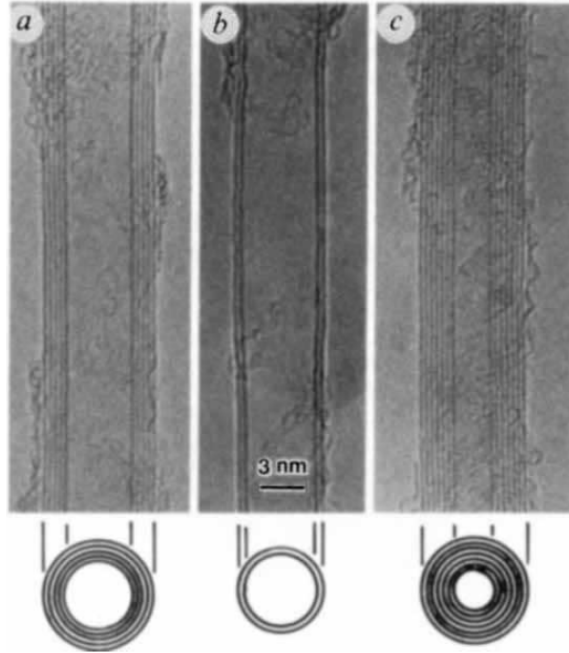
Figure 2 – TEM image of Iijima's CNT discovery showing the structure of multi-wall (a, c) and single-wall (b) CNTs [9].

1.2.1 Graphene

As illustrated in Figure 3, graphene is a single sheet of carbon atoms. Multiple layers of graphene stacked vertically form graphite. Within a single layer of graphene, the carbon atoms form sp^2 hybridized bonds, wherein each atom is connected evenly to three carbons (120°) in the xy plane, and a weak π bond is present in the z axis [10]. The sp^2 set defines a hexagonal lattice typical of a sheet of graphene illustrated in Figure 3. The p$_z$ orbital is responsible for a weaker van der Waals bond. The C-C sp^2 bond length is 1.42 Å and the spacing between layers of graphene is 3.35 Å [10]. The free electrons in the p$_z$ orbital move within this cloud and are no longer associated to a single carbon atom. This phenomenon lies behind the reason why graphite can conduct electricity [10].

The unique sp^2 bonds between carbon atoms found in graphene yield excellent electronic properties, such as high electron mobility (200,000 cm^2 V^{-1}s^{-1}) [11] and low

resistivity (10^{-8} $\Omega \cdot m$) [12]. Because graphene can achieve excellent electron mobility (compared to that of room temperature Si at 1400 cm^2 $V^{-1}s^{-1}$ [2]), it is a promising material for future electronics with operating frequencies beyond several GHz. However, such performance is obtained only over an infinitesimal portion of an epitaxial grown substrate. For commercial applications, controllable electron/hole conduction through this material is needed, along with grain sizes of several inches and defect levels less than 99.99966% [4]. If graphene can be fabricated to meet these requirements, then it can be a viable replacement for commercial silicon based devices and allow microchips to be operated at frequencies beyond several tens of GHz.
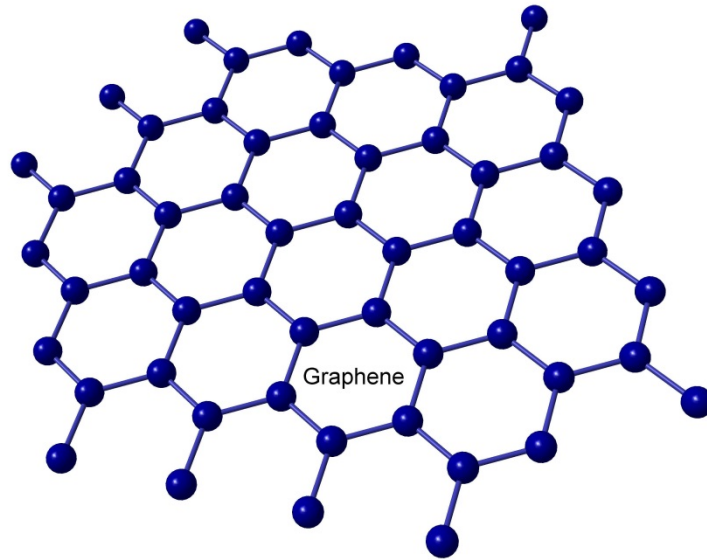
Figure 3 – The image above is an illustration of a sheet of graphene. The dots represent carbon atoms with the connecting lines representing covalent bonds [11].

7

1.2.2 Carbon Nanotubes

CNTs also have the same type of chemical bonds as graphene (sp^2) and are ideal conductors as well. CNTs can be thought of as tubes formed from rolled up sheets of graphene, with relatively small diameters (~ 1 – 10 nm) compared to their lengths (100 nm – several microns). For this visualization, graphene is best represented as a hexagonal lattice, as shown in Figure 4. According to Figure 4, each pair of integers (*n,m*) represents a possible tube structure. With a_1 and a_2 signified as the unit cell base vectors, the chiral vector **C** can be expressed as $C = na_1 + ma_2$, where $n \geq m$ [7]. Based on the integers (*n,m*), the resulting CNT can be of zigzag, armchair, or chiral configuration, and examples of these nanotubes are presented in Figure 5.
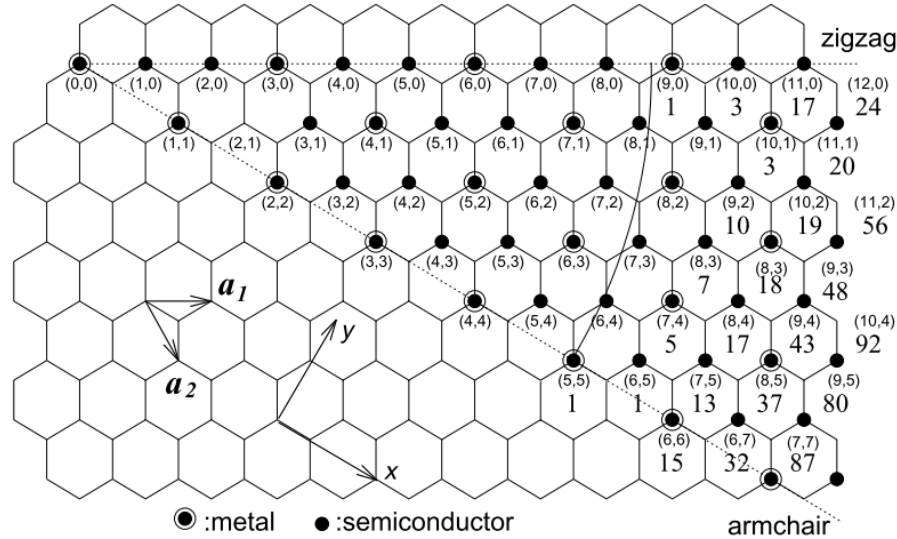
Figure 4 – Possible vectors specified by the pairs of integers (*n,m*) for general CNTs, including zigzag, armchair, and chiral nanotubes. The number below integer pairs represents the number of distinct cap formations that can be joined continuously to the CNT denoted by (*n,m*). The encircled dots denote metallic nanotubes while the small dots are for semiconducting nanotubes [13].

Nanotube dimensions, such as diameter, can be derived from hexagonal coordinates (*n,m*) [10]. The tube diameter *d* can be calculated given (*n,m*), which define

the chiral vector C; the coordinates subsequently determine the rolling direction of the graphene sheet. Thus, the diameter of a carbon tubule can be expressed as:

$$d = \frac{a\sqrt{m^2 + mn + n^2}}{\pi} \qquad (1\text{-}5)$$

where $a = 1.42 \times \sqrt{3}$ Å corresponds to the lattice constant in the graphite sheet [7]. Note that the C–C distance is 1.42 Å for sp^2 hybridized carbon.

An interesting feature of CNTs is the correlation between electrical conductivity and hexagonal coordinates (n,m). It can be seen from Figure 4 that $m = 0$ for all zigzag tubes, while $n = m$ for all armchair tubes, and all other tubes are chiral [10]. In order to determine the armchair and zigzag structure in terms of (n,m) and the inclination angle θ, it is necessary to have the following conditions:

Zigzag: $\theta = 0$; $(n,m) = (p, 0)$, where p is integer

Armchair: $\theta = \pm 30°$; $(n,m) = (2p,-p)$ or (p, p).

The chiral angle θ (angle between **C** and the zigzag direction) is defined as

$$\theta = \tan^{-1}\left[-\frac{\sqrt{3}n}{2m + n}\right] \qquad (1\text{-}6)$$
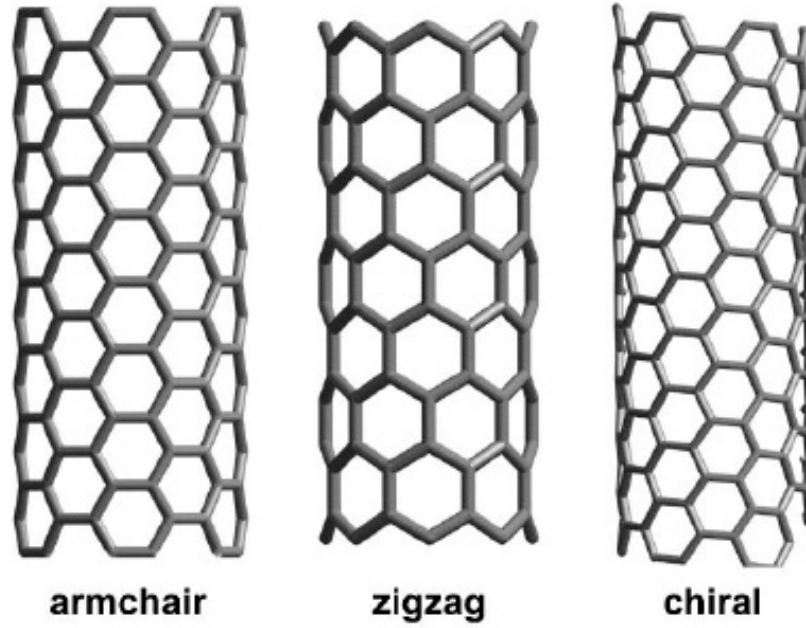
Figure 5 – Above are examples of different types of CNTs. The chirality, or orientation of the hexagons, determines the type of tube: armchair, zigzag or chiral [10].

Theoretical studies on the electronic properties of CNTs indicate that all armchair tubes are metallic, as well as specific zigzag tubes which conform to (1-7) [10].

$$\frac{(2m + n)}{3} = integer \quad (1\text{-}8)$$

Although there is no difference in the chemical bonding between the carbon atoms within the tubes and no doping or impurities are present, it is quite profound that CNTs can be either metallic or semiconducting depending on the choice of (m, n).

Being able to predict the chirality of a CNT before it is synthesized is a challenged faced by research [7], [14], [15]. It has yet to be determined what controls the chirality of CNTs as they are grown, which makes it difficult to grow a particular type of CNT (semiconducting or metallic). Some applications require metallic CNTs, whereas other applications require semiconducting CNTs. Ideal CNT electrical properties are applied to those that are completely free of defects. Much like the large scale production

10

issues graphene faces, if CNTs can be synthesized with a particular chirality and free of defects, they too may become critical components in high-speed microchips.

1.3 Problem Statement

The research problem investigated in this work is the characterization of carbon allotropes formed during the thermal decomposition of SiC. This growth method involves the extreme heating (1200 – 1700°C) of a SiC substrate while under moderate vacuum conditions (10^{-3} – 10^{-5} Torr). The attractiveness of this growth technique is the lack of catalyst metal needed to cause carbon allotrope formation. This growth method is beneficial because the grown nanostructures are conformal to all surfaces. The down side being no in situ measurement approaches can withstand the high temperature required to sublime the silicon (1200 - 1700°C). A variation to the conventional decomposition approach is investigated in this work; whereby a laser is used simultaneously to heat a sample for thermal decomposition and as a Raman spectroscopy source for in situ material characterization.

Thermal decomposition via laser excitation provides the ability to capture nanostructure characteristics while the material is growing. The down side of this method is the growth spot is limited to the spot size of the laser, ~4 μm. This research effort attempts to compare carbon nanostructure growth in both bulk vacuum furnace and laser excitation systems, in order to understand how furnace environment conditions (pressure and temperature) determine the residual carbon allotrope produced (graphene or CNTs). While the potential parameter space of growth parameters (temperature, vacuum,

11

background gas control) is immense, this work aims to add to the current body of knowledge for this growth technique.

1.4 Scope, Limitations and Assumptions

This effort in understanding growth parameters of carbon nanostructures is a continuation of work completed by Mitchel[16], Pochet [17], and Campbell [18], in support of AFRL's ongoing nanostructure device research [4].

The effect of water concentration will not be examined. It is assumed that at the temperatures investigated (1200 - 1700°C) any water molecules will have evaporated and exited the chamber through the vacuum pumps.

Chamber gas will also be excluded from this research. Gasses such as hydrogen and argon have been examined by previous work [19]–[21] as an aid to control the release and formation of SiO_2 during the CNT growth process. The vacuum chambers used in this research have the capability to flow in external gasses, but in order to simplify the growth process, water and external gasses will not be considered during experimentation.

1.5 Methodology

In order to grow 2D nanostructures, two growth methods will be used: the adaptive rapid experimentation and *in-situ* spectroscopy method (ARES) and the moderate vacuum graphite resistance furnace method. For the ARES method, a SiC wafer will be placed in a vacuum chamber and then targeted by a laser beam, as shown in Figure 6. The laser beam will heat the SiC wafer and thermally decompose the silicon carbide, leaving only the carbon atoms behind. The residual carbon atoms will then self-

assemble into 2D carbon nanostructures (either sheets of graphene or columns of nanotubes, depending on chamber settings). While the laser beam is exciting the SiC wafer, the reflected laser energy is sent to a detector system which converts the signal to a Raman spectrum, which assists future analysis [22].
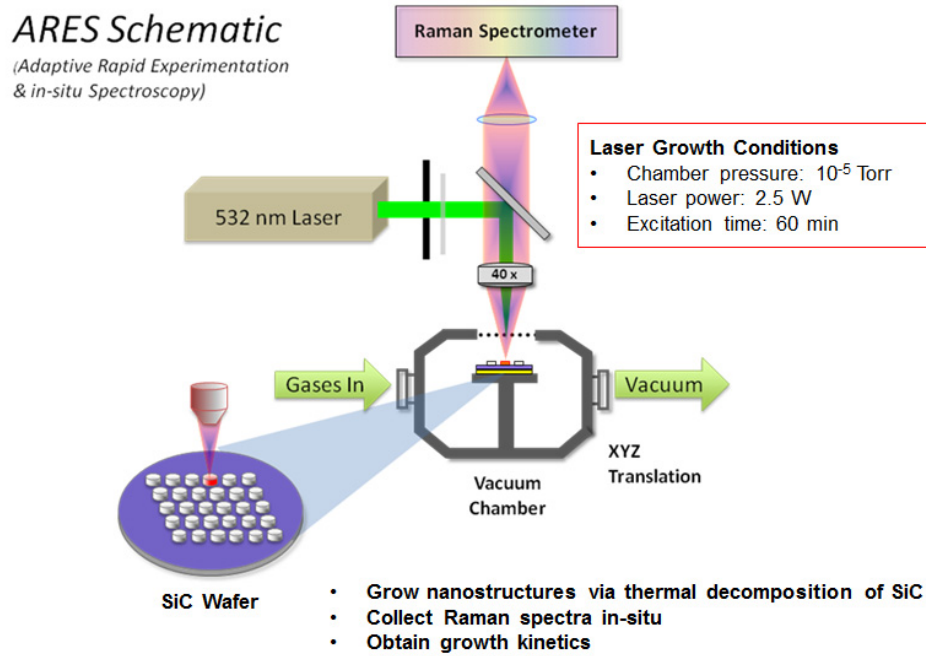
Figure 6 – ARES schematic, showing in situ Raman spectroscopy to study kinetics of carbon nanotube growth. Pillars of silicon carbide are heated using laser pulse to grow nanotubes. The same laser beam is also used to perform in-situ Raman spectroscopy [4].

The substrate's surface temperature in the ARES chamber is controlled by the operating power of the 532 nm laser, which for this research effort is 2.5 W. 2.5 W is the chosen upper limit of the laser output power due to the possibility of damaging the magnification lenses in the ARES system. By controlling the laser power, pressure, and water concentration, the ARES system is expected to grow material similar to that of the bulk vacuum furnace method. In order to determine what temperature the laser chamber is operating, growth temperatures in the bulk vacuum furnace will be swept from 1400-

13

1700°C in 50°C increments. Then, post growth Raman spectroscopy will be used to characterize the resultant material. For cases of the same growth characteristics, the Raman spectra from both methods are expected to produce identical peaks; the Raman spectra of each laser power within the ARES system will be used to aid in determining the substrate temperatures for a given laser power. While this method is less than ideal for determining substrate temperatures for a given laser power, subsequent hurdles prevented the estimation of substrate temperature based on shifts of the anti-stokes peaks in the laser spectrum.

For the Oxy-Gon graphite resistance furnace method, one or more SiC samples will be placed in the heat zone. A high a/c current will pass through the graphite resistor which will generate temperatures > 1400°C, resulting in the decomposition of SiC. The samples were exposed to a given temperature for a predetermined amount of time between 1 and 3 hours. Carbon nanostructures will grow on these samples in the same way as in the ARES system. The validity of this assumption comprises a portion of the desired thesis results.

The fabricated nanostructures from the furnace (graphene and CNTs) will undergo detailed characterization, including scanning electron microscopy (SEM) to verify physical features, and Raman spectroscopy to determine chemical composition and structural properties. Finally, the Raman spectra from both methods will be compared to determine the ARES system operating temperature.

Until this time, the ARES system was used strictly for CNT growth on Si pillars. During these investigations, temperatures ranging from 500°C to 1400°C were achieved by focusing the laser on a Si pillar which was coated with 2 − 3 nm of either Fe or Ni

[23]. An ethylene feed gas (5 sccm) was employed as a catalyst to initiate CNT growth. Chamber pressure and catalytic feed gas were then varied to investigate resultant tube chirality and growth rate. This thesis is the first to look at in-situ carbon nanostructure growth on SiC using Raman spectroscopy. Additionally, this work is the first to perform Raman spectroscopy on multiple wafer locations containing carbon nanostructures formed using the AFRL/RXA vacuum furnace.

1.6 Thesis Structure

The remaining chapters of this thesis provide more information on carbon nanostructure growth mechanics and methods used to study them. Chapter 2 discusses previous research on plasma etching, silicon carbide crystalline structure and Raman spectroscopy, which are topics beneficial in understanding applied methodology discussed in Chapter 3. The methodology chapter explains the two growth processes employed to grow the nanostructures, and details explaining how data was collected using Raman spectroscopy. Data collected from the Raman spectra are analyzed and discussed in Chapter 4. The conclusion chapter contains a summary of the conducted research and suggestions for future work.

II. Literature Review

2.1 Chapter Overview

The purpose of this chapter is to summarize literature reviewed in this research effort. The first section discusses the mechanics of thermally decomposing silicon carbide to yield carbon nanostructures. Specific growth characteristics for graphene and CNTs are also explored within this section. The last section covers the principles behind Raman spectroscopy and prior work characterizing various carbon allotropes using Raman spectroscopy.

2.2 Thermal Decomposition of Silicon Carbide

The basic unit of the silicon carbide crystal consists of tetrahedrons with a C (or Si) atom at the center, surrounded by four Si (C) atoms covalently bonded. These basic units are periodically repeated in closed-packed hexagonal layers, whose stacking sequence gives rise to the different polytypes [24]. Although they have different stacking sequences, the various polytypes have few similarities between them. For instance, each C (Si) atom is situated above the center of a triangle of Si (C) atoms and underneath a Si (C) atom belonging to the next layer in a tetrahedral formation. With reference to Figure 7, if the first Si-C layer is labelled A, the next layer that can be placed according to a closed packed structure will be placed either on B or C. The different polytypes are constructed by permutations of these three positions. The nomenclature for the various polytypes utilizes the number of layers in the stacking direction, before the sequence is repeated, combined with the letter representing the Bravais lattice type: cubic (C), hexagonal (H) or rhombohedral (R) [24]. The distance between neighboring silicon or

16

carbon atoms is ~3.08 Å, while the distance between the C atom to each of the Si atoms (Si-C bond length) is ~1.89 Å for all polytypes [24].
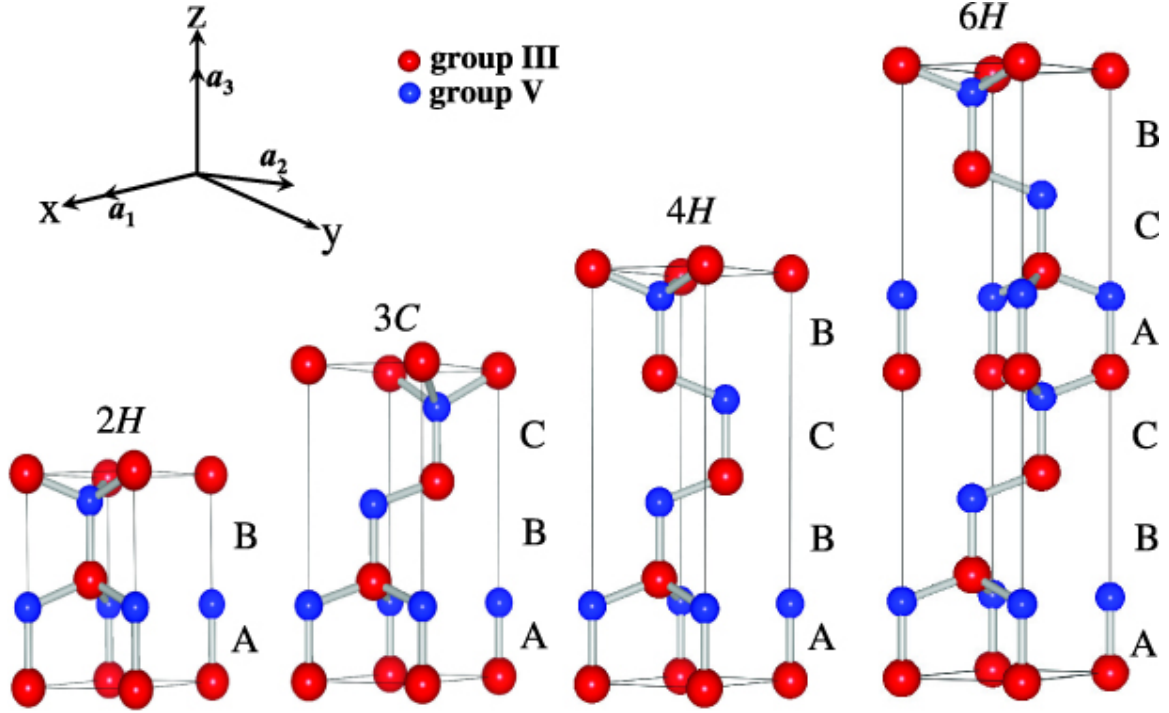
Figure 7 – The four most common polytypes of SiC – 2H, 3C, 4H and 6H [24]. In this illustration, the red spheres represent Si atoms and the blue spheres represent C atoms.

Thermal decomposition of SiC is a fairly new method of growing CNTs. M. Kusunoki first discovered that aligned CNTs were formed on the surface of SiC particle heated at 1700 using a laser system attached to a transmission electron microscope in 1997 [25]. A year later, Kusunoki then realized CNT films were produced by heating SiC in a vacuum electric furnace. In this process, a silicon carbide wafer is heated beyond the melting point of silicon (> 1414°C) in a vacuum chamber (< 10^{-3} Torr). As the wafer maintains a temperature of 1700°C, the silicon sublimes and exits the bulk material as a gas. The carbon atoms left behind self-assemble to form carbon nanostructures. This technique is capable of producing graphene and CNTs, with

chamber temperature and pressure being the determining factors of which material is produce.

Historically, the most common methods of producing CNTs are: arc-discharge, laser ablation, and chemical vapor deposition (CVD); a detailed description of these methods is found in appendix A. Common to these three methods is the requirement of a metal catalyst to interact with a carbon stock in order to initiate CNT growth. In each method, the metal catalyst remains in the fabricated CNTs as an impurity, and therefore diminishes electrical performance [13]. In contrast, the thermal decomposition method does not require a metal catalyst. As such, CNTs free of metal impurities are formed, which should theoretically exhibit more ideal CNT properties inherently needed for high speed devices [4].

In 1997 Kusunoki and others first reported growing CNTs via thermal decomposition of SiC wafers [25]. Since this discovery, much insight has been documented on this process regarding the chemical growth mechanics of carbon nanostructures [25]–[27]. Research has shown that regardless of the nanostructure type grown (CNTs or graphene), the governing chemical equations remains the same; it is only the environmental conditions (temperature and pressure) that determine which carbon allotrope will be produced.

In 1999, Kusunoki [25] described a theory of the formation mechanism of CNT film on a SiC crystal by the surface decomposition method. Figure 8 provides a schematic diagram of the physical process. The chemical equations in (2-1) to (2-3) provide insight toward the details of the decomposition process.

18

$$SiC_{(s)} + \frac{1}{2}O_{2(g)} \rightarrow SiO_{(g)} + C_{(s)} \tag{2-1}$$
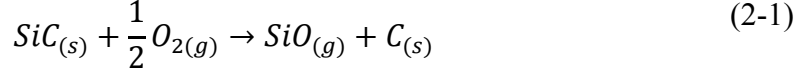
In (2-1), solid SiC is continuously oxidized to form SiO gas, without forming a passive SiO_2 film. The solid carbon formed in this equation is in the form of graphitic layers as illustrated in Figure 8(a). At over 1000°C, several graphite sheets are formed parallel to the (0001) SiC plane by the oxidation of Si [25]. Because of low chamber pressure (10^{-4} Torr), SiO molecules modify to form solid SiO_2 clusters, which disperse in all directions, after passing through broken thin graphite sheets, as presented in equation (2-2). Equation (2-2) describes the modification of the SiO molecule and is illustrated in Figure 8(b). This reaction takes place within the gas bubbles that lie on the SiC surface, and below the layers of graphite. At around 1300°C, carbon nanocaps are formed by generation of bubbles of a SiO gas on the SiC crystal [25]. The graphite sheets start to stand up on the (0001) SiC plane and begin to form CNTs.

$$SiO_{(g)} + \frac{1}{2}O_{2(g)} \rightarrow SiO_{2(s)} \tag{2-2}$$

Combining equations (2-1) and (2-2) yields the over-arching equation describing the CNT formation process, equation (2-3). Ultimately, when the temperature reaches 1500°C, CNTs grow towards the interior of the SiC crystal, decomposing the SiC single crystal.

$$SiC_{(s)} + O_{2(g)} \rightarrow SiO_{2(s)} + C_{(s)} \tag{2-3}$$
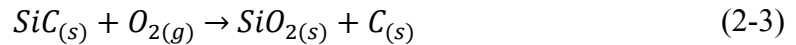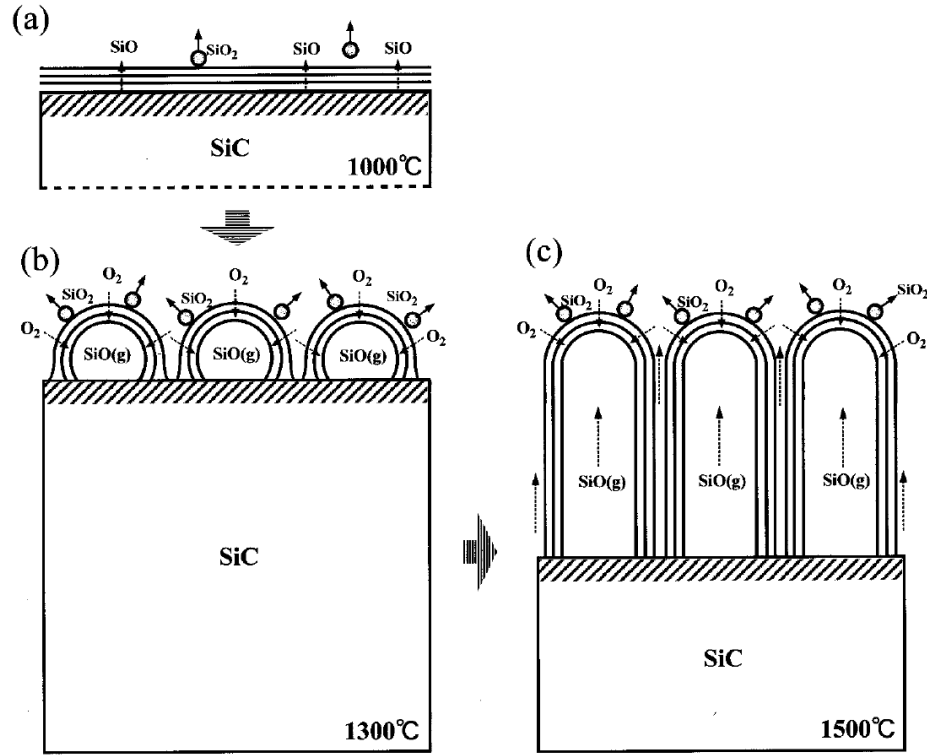
Figure 8 – Schematic diagram for the formation mechanism of the CNT film on a SiC crystal by the surface decomposition method by Kusunoki [25].

The equations suggested by Kusunoki coincide with research by Song and Smith [28]. Song and Smith reported on the interactions of oxygen with the 4H– and 6H–SiC surfaces at high temperatures. They propose the oxidation of SiC can be broken down into three distinct regions as shown in Figure 9. The three regions depend on O_2 pressure and SiC temperature.
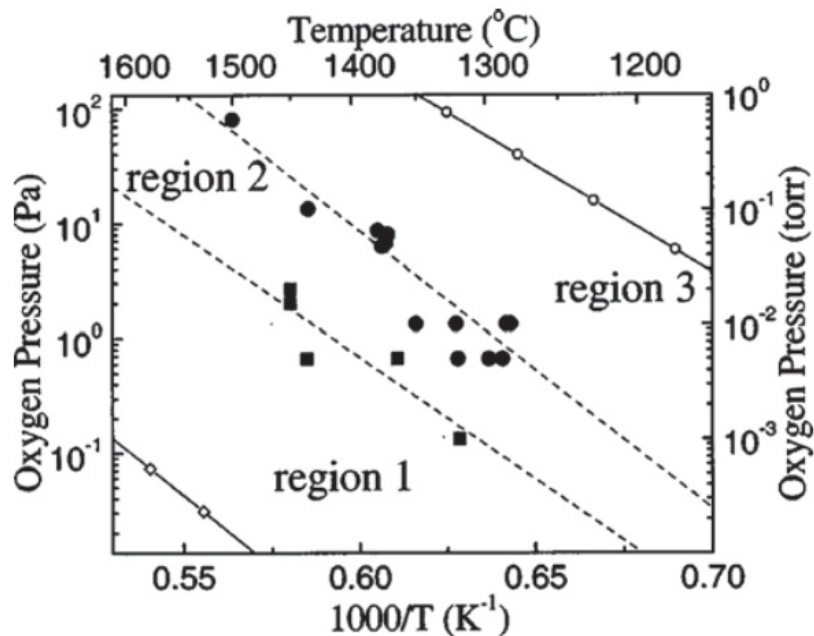
Figure 9 – Phase diagram relating oxygen pressure to SiC temperature. According to the authors, carbon nanostructures are found to grow in region 1. From the information found in this plot, a temperature range can be found for solid carbon growth [28].

As shown in Figure 9, regions 1 and 2 represent active oxidation zones, where SiC vaporizes as SiO or CO, which then yields graphitic carbon. Region 3 is the passive oxidation zone, where a SiO_2 layer is formed, preventing SiC to further oxidize [28]. In the CNT and graphene growth processes, Song and Smith suggest the SiC oxidation reaction must be controlled within the active oxidation zone [28].

2.2.1 Graphene Formation

This section focuses on the growth of graphene on SiC in a high vacuum (HV) chamber environment. The previous section provided information on general oxidation of SiC, and its effect on thermal decomposition. Of the various parameters involved with growing graphene in a vacuum chamber, this section focuses on controlling the sublimation rate of SiC.

De Heer *et al.* [29] discussed their approach of confinement controlled sublimation (CCS) of SiC to grow graphene. In this article, they propose the high temperature anneals remove impurities and produce graphene with few defects. However, they report that increasing the temperature also increases the Si sublimation rate, which also causes defects [29]. To correct this issue, De Heer *et al.* report that either an inert gas backpressure resides above the SiC surface, or residual Si gas confined to a small volume may control the rate of solid Si sublimation as shown in Figure 10.
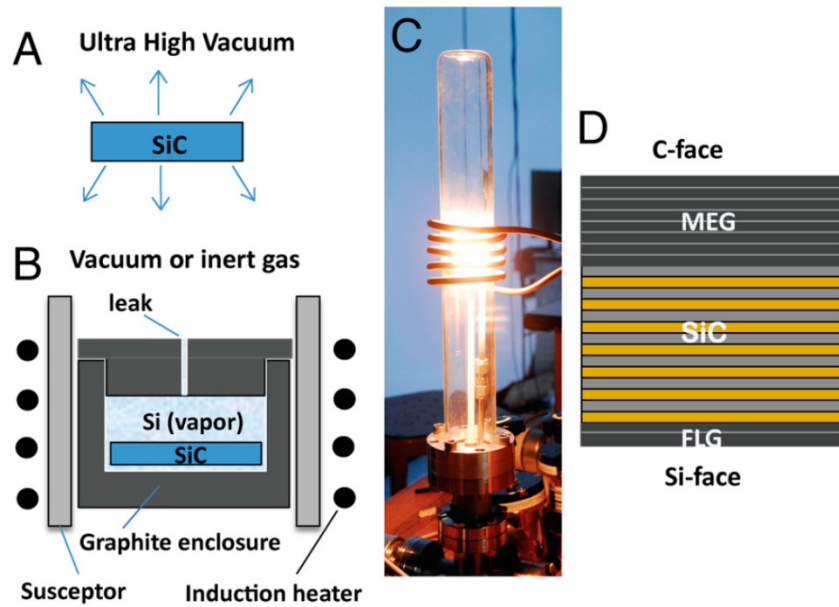
Figure 10 – The images above illustrates de Heer's attempt of controlling the sublimation of SiC by means of confined Si gas [29].

De Heer *et al.* suggest the popular method of decomposing SiC in UHV produces inferior graphene material. Figure 10(A) illustrates thermal decomposition of a SiC wafer in UHV. The sublimed Si is not confined to an enclosed volume, rather is removed from the SiC surface via vacuum pumps, which causes rapid, unstable graphene growth. Figure 10(B) shows the proposed CCS method. Sublimed Si gas is confined in a graphite

enclosure such that growth occurs in near thermodynamic equilibrium, dissimilar to common thermal decomposition techniques. Nanostructure growth rate is controlled by both the enclosure aperture (leak), and the background gas pressure. A photograph of the induction furnace is shown in Figure 10(C). Under CCS conditions, shown in Figure 10(D), few graphite layers (from 1 to 10 layers) grows on the Si terminated face, and multilayer epitaxial graphene (from 1 to 100 layers) grows on the C terminated face.

2.2.2 CNT Formation

Maruyama states zigzag CNTs are typically produced from thermally decomposing SiC [27]. Figure 11 illustrates the erosion of SiC as CNTs grow into the substrate. Boeckl [30] states CNTs grow 3 times faster on the C side vs the Si surface. However, the polished side of the wafer is the Si-face and can be patterned by photolithographic methods; whereas the C-face tends to have a rougher surface making it more difficult to sputter on metal in order to make a mask for patterning.
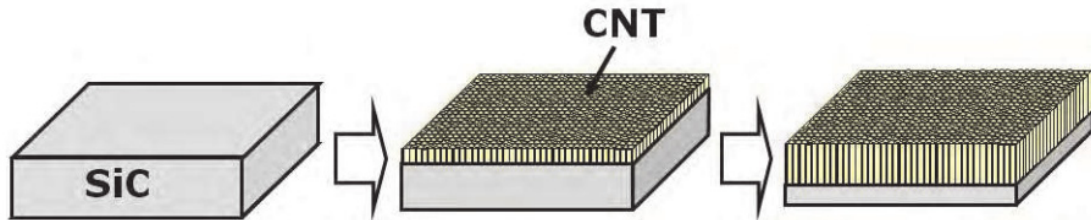
Figure 11 – Process diagram of CNT growth via decomposition of SiC [27].

Rummeli investigated CNT growth without a catalyst [31]. One of the methods mentioned is thermal decomposition of SiC. Rummeli states decomposition is achieved by annealing SiC in HV at temperatures between 1400 and 1700°C. He then goes on to say this process only works with trace amounts of oxygen at the decomposition site with local electron energy loss spectroscopy studies showing oxygen species near and at the

surface of the SiC [31]. This finding supports the notion of oxygen controlling the sublimation rate of Si [32].

2.3 Raman Spectroscopy

Raman spectroscopy is a material characterization technique based on the Raman scattering phenomenon of electromagnetic radiation by molecules. Raman spectroscopy is used to observe vibrational, rotational and other low-frequency modes in a system. When materials are irradiated with electromagnetic energy of a single frequency, i.e. laser source, the light is scattered by molecules by elastic and inelastic collisions. These collisions result in the energy of the laser photons being shifted up or down the energy spectrum. The shift in energy reveals information about the atomic vibrational modes in the system [33]. Elastic scattering (Rayleigh scattering) is generated by scattered light which has the same frequency as that of the radiation. Inelastic scattering (Raman scattering) is produced by scattered light which has a different frequency from that of the radiation.

Generally, a laser beam illuminates a sample then the scattered beam gets reflected into a lens which focuses the beam through a monochromator [34]. Wavelengths close to the laser line due to elastic Rayleigh scattering are filtered out while the rest of the collected energy is sent into a detector. This characterization technique is beneficial in this portion of the laboratory work because physical contact with the material is not required in order to collect data. As the sample is energized by the laser, Raman data is collected *in situ*.

2.3.1 Principles of Raman Spectroscopy

Vibrational spectroscopy is a technique applied to analyze the structure of molecules by examining the interaction between electromagnetic radiation and nuclear vibrations in molecules. Vibrational spectroscopy uses electromagnetic waves with wavelengths in the order of 10^{-7} m, than the X-rays with wavelengths in the order of 10^{-10} m. Typical electromagnetic waves in vibrational spectroscopy are infrared light [35]. Energies of infrared light match with vibrational energies of molecules [35]. Vibrational spectroscopy detects the molecular vibrations by the absorption of infrared light or by the inelastic scattering of light by a molecule. Vibrational spectroscopy can be used to examine gases, liquids and solids. It is widely used to examine both inorganic and organic materials. However, it cannot be used to examine metallic materials because they strongly reflect electromagnetic waves [35].

Commonly, the vibrational spectroscopy covers a wavenumber range from 200 to 4000 cm^{-1} [35]. In addition to molecular vibrations, crystalline solids also generate lattice vibrations. The lattice vibrations refer to the synchronous vibrations of all the atoms in crystal lattice. These vibrations exhibit lower frequencies, compared with those of common molecular vibrations, and have a wavenumber range of about 20 – 300 cm^{-1} [35]. Coupling between lattice and molecular vibrations can occur if the molecular vibrations lie in such a low wavenumber range. Molecular vibrations can be distinguished from the lattice vibrations because they are not as sensitive to temperature change as lattice vibrations.

The energies of molecular vibrations match with those of electromagnetic radiation in a wavelength range near visible light (10^{-4} – 10^{-6} m) [35]. The

electromagnetic radiation in near visible light is able to change the status of molecular vibrations and produce vibrational spectra of molecules. Vibrational spectroscopy characterizes the electromagnetic waves in terms of wavenumber (cm^{-1}), which is defined as the reciprocal of wavelength in the unit of cm^{-1}:

$$\tilde{\upsilon} = \frac{1}{\lambda} \tag{2-4}$$

In other words, the wavenumber ($\tilde{\upsilon}$) is number of waves in a 1 cm-long wave segment. It is useful to remember that the wavenumber is proportional to the frequency of the electromagnetic wave (υ) with a constant factor that is the reciprocal of the speed of light (c):

$$\tilde{\upsilon} = \frac{1}{c}\upsilon \tag{2-5}$$

The wavenumber represents radiation energy, as does wavelength [35]. Electromagnetic waves can be considered as photons. The photon energy is related to the photon frequency (υ_{ph}).

$$E = h\upsilon_{ph} \tag{2-6}$$

h is Planck's constant (6.626 x 10^{-34} J·s). Thus, the photon energy can be represented as its wavenumber:

$$E = hc\tilde{\upsilon} \tag{2-7}$$

The conversion constant (hc) is about 2.0 x 10^{-23} J cm s. For a wavenumber of 1000 cm^{-1}, the corresponding energy is about 2.0 x 10^{-20} J or 0.12 eV. Note that this is much smaller than the photon energy of X-rays, which is in the order of 10000 eV. The vibrational spectra for Raman data are in the wavenumber range from several hundreds to

thousands. This indicates that the vibrational energy of molecules are only in the order of 10^{-2} to 10^{-1} eV.

When a molecule interacts with an electromagnetic field, a transfer of energy from the field to the molecule can occur only when Bohr's frequency condition is satisfied; namely,

$$\Delta E = h\upsilon = h\frac{c}{\lambda} = hc\tilde{\upsilon}. \tag{2-8}$$

Here, ΔE is the difference in energy between two quantized states. Thus, $\tilde{\upsilon}$ is directly proportional to the energy of transition.

Given that

$$\Delta E = E_2 - E_1, \tag{2-9}$$

where E_2 and E_1 are the energies of the excited and ground states, respectively, then the molecule is said to "absorb" ΔE when it is excited from E_1 to E_2, and "emits" ΔE when energy reverts from E_2 to E_1.

Figure 12 shows the basic processes which occur for one vibration. At room temperature, most molecules, but not all, are present in the lowest energy vibrational level. Since the virtual states are not real states of the molecule but are created when the laser interacts with the electrons and causes polarization, the energy of these states is determined by the frequency of the light source used. The Rayleigh scattering has the most intense energy since most photons scatter in this matter [34]. It does not involve any energy change and consequently the light returns to the same energy state. The Raman scattering process from the ground vibrational state (E_0) leads to absorption of energy by the molecule and its promotion to a higher energy excited vibrational state

($E_0 + h\nu_m$). This is called Stokes scattering. However, due to thermal energy, some molecules may reside in this excited state ($E_0 + h\nu_m$). Scattering from this states to the ground state (E_0) is called anti-Stokes scattering and involves transfer of energy to the scattered photon. The relative intensities of the two processes depend on the population of the various states of the molecule. The populations can be worked out from the Boltzmann equation, but at room temperature, the number of molecules expected to be in an excited vibrational state will be small [34].
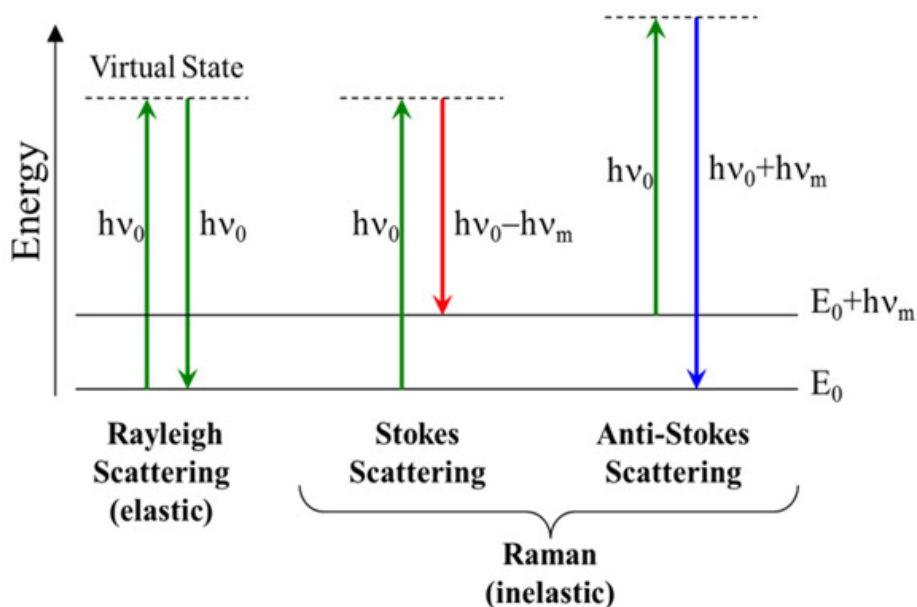
Figure 12 – Diagram of the Rayleigh and Raman scattering processes [36].

When compared to Stokes scattering, the number of molecules resembling anti-Stokes scattering will be weak; and will become weaker as the frequency of the vibration increases, due to decreased population of the excited vibrational states. Additionally, anti-Stokes scattering will increase relative to Stokes scattering as the temperature rises.

There is a basic selection rule which is required to understand this pattern. Intense Raman scattering occurs from vibrations which cause a change in the polarizability of the

electron cloud around the molecule. Usually, symmetric vibrations cause the largest changes and give the greatest scattering. This contrasts with infrared absorption where the most intense absorption is caused by a change in dipole, and hence, asymmetric vibrations which causes the most intense scattering phenomena [34].

Provided that there is no change in electronic energy, for example, by the absorption of a photon and the promotion of an electron to an excited electronic state, the energy of a molecule can be divided into a number of different parts or 'degrees of freedom'. Three of these degrees of freedom are taken up to describe the translation of the molecule in space and three to describe rotational movement except for linear molecules where only two types of rotation are possible. If N is the number of atoms in a molecule, the number of vibrational degrees of freedom, and therefore the number of vibrations possible, is $3N - 6$ for all molecules except linear ones where it is $3N - 5$. For a diatomic molecule, this means there will be only one vibration. In a molecule such as oxygen, this is a simple stretch of the O–O bond. This will change the polarizability of the molecule but will not induce any dipole change since there is no dipole in the molecule, and the vibration is symmetric about the center. Thus the selection rules discussed predict that oxygen gas will produce a band in the Raman spectrum and no band in the infrared spectrum.

2.3.2 Graphene Characterization via Raman Spectroscopy

Volumes of papers have been written discussing the benefits of using Raman spectroscopy to characterize graphene [37]–[41]. Of those released articles, it is Dresselhaus *et al.* [38] who deliver the most relevant insight into graphene, and other similar allotropes of carbon. As Figure 13 shows, the Raman spectrum of single layer

graphene consists of two dominant spectral features. Scanning from left to right, the first peak representing the longitudinal optical (LO) phonon mode is located ~ 1580 cm^{-1}; this peak is referred to as the G band. The second peak is a second-order dispersive Raman feature called the G' and is located ~ 2700 cm^{-1} [38].

Raman spectroscopy for the various sp^2 carbon materials, displayed in Figure 13, has been mainly used for sample characterization and these different carbon materials exhibit characteristic differences related to the small differences in their structures [41]. The fundamental sp^2 carbon material is mono-layer graphene which has the simplest and most fundamental spectrum showing the two Raman-allowed features that appear in all sp^2 carbon materials: the first-order G-band and the second-order symmetry-allowed G'-band, where the symbol G is used to denote "graphitic." The next most commonly observed feature is the D-band that is a defect-activated Raman mode. A clear message derived from Figure 13 is that every different sp^2 carbon material in this figure shows a distinct Raman spectrum, which can be used to understand the different properties that accompany each of these different sp^2 carbon structures. For example, 3D highly oriented pyrolytic graphite (HOPG) shows a different spectrum from that of single-layer graphene, which in turn is distinct from the Raman spectra characteristic of the various few layer-graphene materials, as displayed in Figure 14.
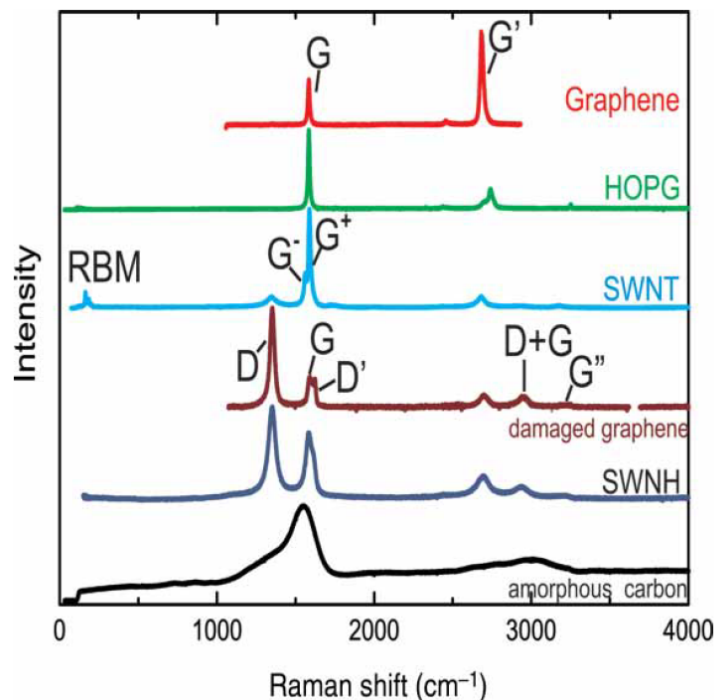
Figure 13 – Raman spectra from several sp^2 nanocarbon and bulk carbon materials. From top to bottom: crystalline mono-layer graphene, HOPG, an SWNT bundle sample, damaged graphene, single-wall carbon nanohorns (SWNH). The most intense Raman peaks are labeled in a few of the spectra [41].

The D-band occurs at about 1350 cm^{-1} at 2.41eV laser excitation energy (E_{laser}) and is directly proportional to the value of E_{laser} [41]. Since the graphite melting temperature is very high (over 4200 K) and since no actual carbon materials are defect-free, the D/G-band intensity ratio (I_D/I_G) provides a suitable metric for the degree of disorder in sp^2 carbon materials over a wide temperature range [38]. In the case of graphene, the (I_D/I_G) ratio and the lineshape of the G'-band can be used for identifying the number of graphene layers [41]. Figure 14, from Ferrari, compares the 514 nm Raman spectra of graphene and bulk graphite. The two most intense features are the G and G' peaks [39]. The linewidth of the G' band is narrower for graphene than it is for multilayer graphite. This observation supports the relationship of the number of graphitic layers being directly proportional to its requisite G' linewidth.
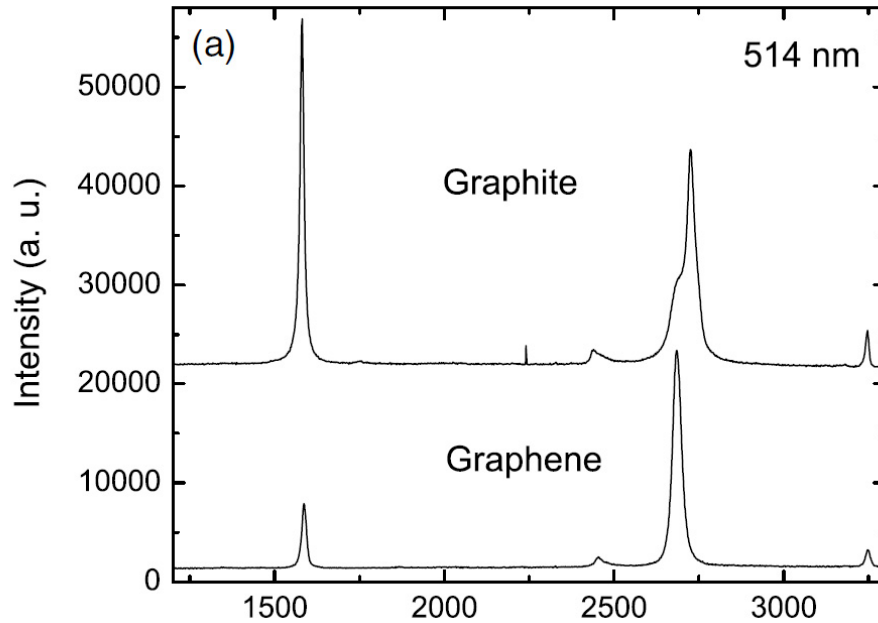
Figure 14 – Comparison of Raman spectra at 514 nm for bulk graphite and graphene. They are scaled to have similar height of the 2D peat at ~2700 cm^{-1}[39].

Figure 15 displays the Raman spectra of CNTs grown on a SiC substrate using the Oxy-Gon furnace. This previous work was conducted by Mitchel [16], and provides a baseline for current research to build upon. This research effort adds to the data set in that different surfaces will be examined for nanostructure growth. Mitchel performed thermal decomposition on smooth, flat SiC wafers. This research effort looks at SiC pillars as well as the etched substrate surface. Raman data collected from the Oxy-Gon furnace method will be compared to Raman results reported by Mitchel, to reveal if the same material is present from the different SiC features.
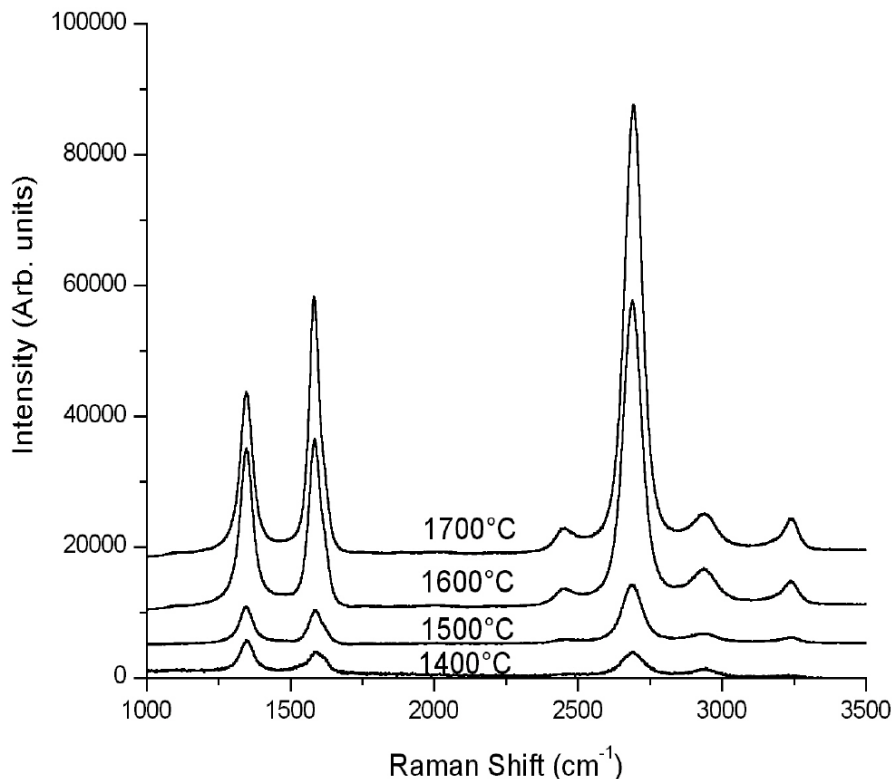
Figure 15 – Raman spectra of CNTs/SiC at 10^{-5} Torr for 30 minutes on Si-face 4H-SiC [16].

2.3.3 CNT Characterization via Raman Spectroscopy

Many areas of basic and applied nanotube research have an essential need to analyze SWNT samples to determine the structural species that are present. According to Weisman and Subramony, when Raman spectroscopy is employed, and the wavelength of the incident laser is close to a strong optical absorption feature of a nanotube species, relatively intense resonance Raman scattering is generated [42]. In the case of CNTs, a special Raman-active phonon mode related to the vibrations of a pentagonal ring (1469 cm^{-1}) is particularly critical for understanding the molecular structure [41]. This Raman spectrum, previously shown in Figure 13, shows the G-band vibrational mode, which arises from tangential and longitudinal C-C stretching motions, and the radial breathing

33

mode (RBM), which represents symmetric expansion and contraction of the nanotube cylinder. This vibrational mode is unique to carbon nanotubes and serves to identify their presence in a given sample. Since the RBM frequency is inversely proportional to the nanotube diameter, the diameter distribution of the nanotubes that are contained in a given sample can be estimated, as well as determining if the tubes are metallic or semiconducting [41]. When an isolated nanotube is observed, its Raman spectrum can be used to obtain its detailed structure, which reveals the hexagonal lattice orientation, the diameter and the chiral angle of the nanotube, as well as the nanotube (n,m) chirality assignment [41]. Although the G-band frequency is not sensitive to nanotube structure, its linewidth differs significantly for metallic and semiconducting species [42]. A limitation of Raman analysis, however, is that it reveals the spectra only of those species having electronic transitions close to the incident laser wavelength. To perform a full analysis, one may therefore need to collect Raman spectra using numerous lasers.

III. Methodology

3.1 Chapter Overview

The purpose of this chapter is to discuss the methodologies applied in this research effort. Significant processes include pre-processing the samples to prepare them for nanostructure growth, carbon nanostructure growth via thermal decomposition (i.e. graphite resistance furnace and laser excitation), and material analysis by means of Raman spectroscopy.

Growing nanostructures on a SiC substrate using the laser excitation growth process require a high degree of thermal isolation for the incident laser to adequately heat the substrates; this thermal isolation is achieved by patterning pillars onto the SiC surface. The pillar patterning step involves plating the wafer with nickel (Ni), patterning the Ni with a photolithographic mask, and then patterning the SiC wafer with the design determined by the Ni mask, using a RIE process. The SiC decomposition processes consist of placing the wafer in a vacuum chamber and heating the sample to a known temperature for a predetermined amount of time. Material analysis via Raman spectroscopy involves exciting a point of nanostructure material on a SiC wafer with a laser source, and capturing the scattered beam via photon detectors. Energy from the laser is absorbed by the material, and then re-emitted into the photon detector. The software collects the data and displays it as a Raman shift plot.

3.2 Sample Patterning

The end result of this step is a patterned SiC wafer with arrays of 10μm tall pillars, 10μm in diameter, spaced 50 μm apart. The process is illustrated in Figure 16.

The spacing is intended to result in thermal isolation between individual SiC pillars, and allows for hundreds of experiments to be performed on a 1 cm x 1 cm sample, when used in the laser excitation method. To begin the process, a chemical – mechanical polished (CMP) n-doped 4H – SiC wafer is diced into 1 cm x 1 cm samples. Next, a Torr ® Electron Beam Evaporation System deposited 2200 Å of nickel (Ni) on the polished SiC wafers. An AlphaStep IQ Surface Profiler verified the thickness of the Ni layer. A measured thickness of 1980 Å fell within the required tolerance of +/- 200 Å. After the thickness was verified, the samples are cleaned with 30 second rinses each of acetone, methanol, isopropanol, and de-ionized water (DIW). Once cleaned, the samples are then coated with 5 μm of 1805 photoresist (PR), spun at 3000 RPM for 30 seconds, with a 4 sec 500 RPM spread, and baked for 75 seconds on a hot plate set at 120°C.
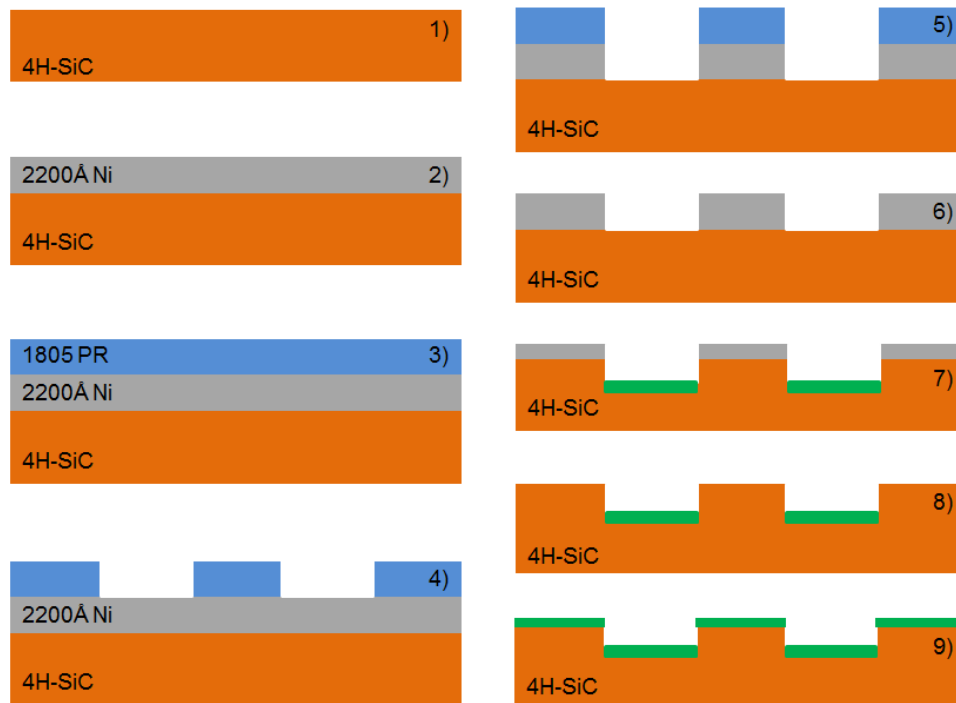
Figure 16 – Illustration of process diagram showing the steps required to pattern SiC wafers. The brown color represents SiC wafer, gray is Ni masking layer, blue is 1805 PR, and the green signifies the rough SiC surface left behind from the RIE.

36

Next, a SUSS Microtec MJB3 mask aligner is used to expose the samples, for 4 seconds under an ultraviolet (UV) lamp to one of two fabricated masks consisting of arrays of 10 micron diameter circles, spaced 50 μm apart. The first mask used was a uniform sheet of circles. This mask was satisfactory for the furnace growth method. However, samples made from this mask proved to be less than ideal for use in the laser excitation method. In order to keep track of individual experiments on a sample containing thousands of pillars, the pillars need to be identified in some fashion. Therefore, a new mask was fabricated which consisted of a grid pattern containing a 5-by-5 array of circles. After UV exposure, the samples are developed for 45 seconds using Microdeposit 351 developer, mixed at a ratio of 1:5 with DIW, and followed by a 30 second DIW rinse. Figure 17 displays the resulting samples with patterned circles of PR on top of the Ni layer.
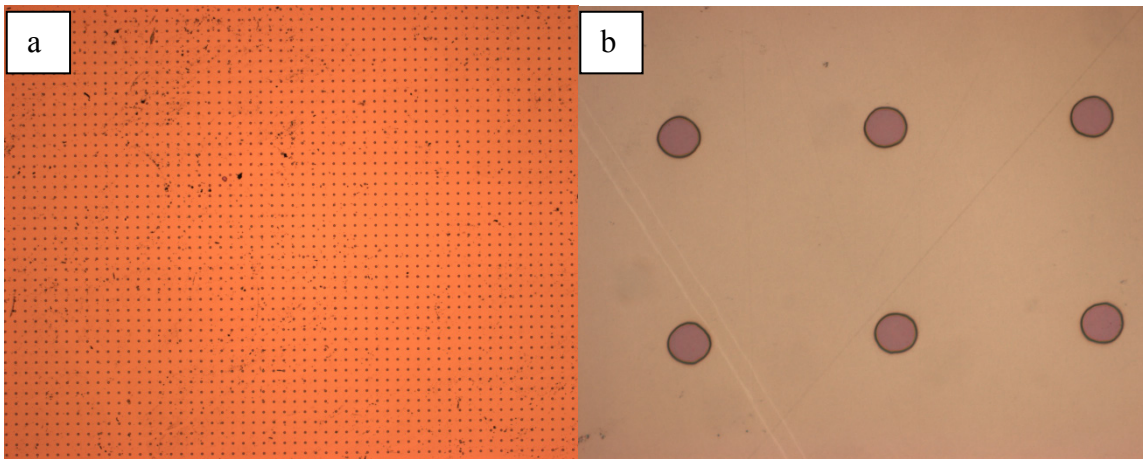
Figure 17 – Microscope images showing patterned PR layer on top of the Ni layer. Figures **(a)** and **(b)** display 5X and 100X magnifications, respectively.

With the PR properly exposed and developed, the samples are then submerged in Transcene ® TFG Nickel Etchant (Ni Etchant) to transfer the circle array from the PR to the Ni layer. Prior to etching, the Ni Etchant was heated to 50°C on a hot plate. To

achieve this temperature, 50 mL of Ni Etchant was poured into a 250 mL beaker and placed on a hot plate set at 100°C. The temperature of the liquid was verified by a glass thermometer placed inside of the beaker. After 15 minutes, the temperature of the Ni Etchant reached 50°C and the hot plate was set to 90°C to maintain this temperature. Next, individual samples were lowered into the Ni Etchant and slowly agitated for 4 - 4.5 minutes, then removed and rinsed with DI water. Figure 18 is an image captured from an optical microscope illustrating the undercutting from the Ni Etchant. The larger circle is the PR and the smaller circle is the Ni layer. The difference in diameters of these two features is due to the undercutting of the Ni Etchant on the Ni layer. From this finding, it was decided not to use a mask with circles less than 10 µm.
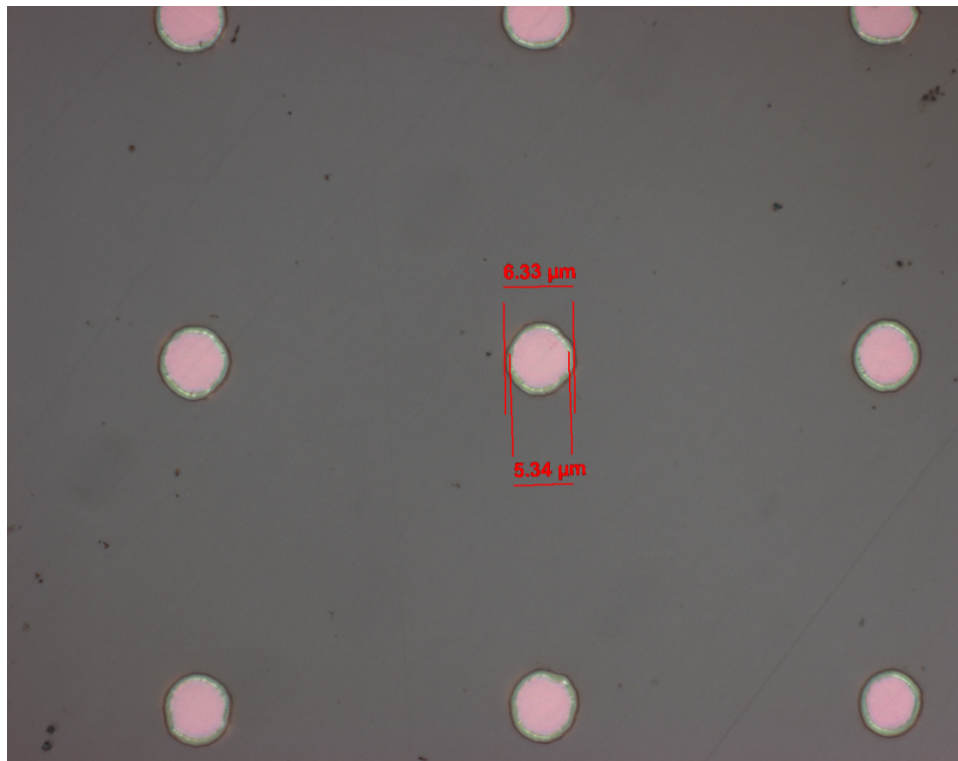
Figure 18 – Optical microscope image displaying the patterned Ni layer before the PR has been removed. The dimensions reveal a 1 micron over-etch.

After the Ni is patterned, the remaining PR is removed with 30 second rinses each of acetone, methanol, isopropanol, and DI water. Once the remaining PR is removed, as shown in Figure 19, the samples are placed back into the AlphaStep IQ Surface Profiler to confirm the correct Ni thickness is left behind. With the Ni layer at a sufficient thickness (~1980 Å), the wafers are ready for the next step of reactive ion etching.

Figure 19 – Optical microscope image showing patterned Ni layer after the PR has been removed.

RIE took place in a Trion Reactive Ion Etch chamber. The chamber was set with the following parameters: power = 250 watts, pressure = 85 mTorr, CF_4 gas flow = 25sccm, O_2 gas flow = 5sccm. Three, 1 hour etch sessions were conducted and resulted in an overall etch depth of 7.0-8.0μm, as shown in Figure 20(a). Once this depth was achieved, the Ni layer was no longer needed and was removed in 50°C of Ni Etchant for

eight minutes on a hot plate. After the Ni was removed, as shown in Figure 20(b), the

wafers were cleaned with 30 second rinses each of acetone, methanol, isopropanol, and

DIW. The broad array of pillars on the SiC surface is shown in Figure 21(a).
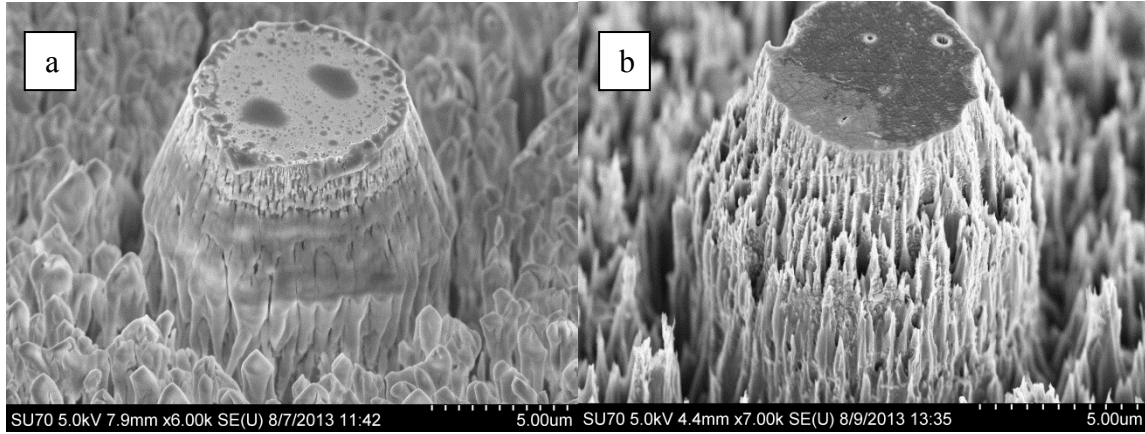
Figure 20 – SEM image of SiC pillar etched in CF_4 showing (a) pre- and (b) post Ni layer removal. Note: the images shown pre- and post- are not of the same pillar, but are representative of the pillars produced during the as-mentioned fabrication step.   The roughened etched surface is a by-product of micro-masking.
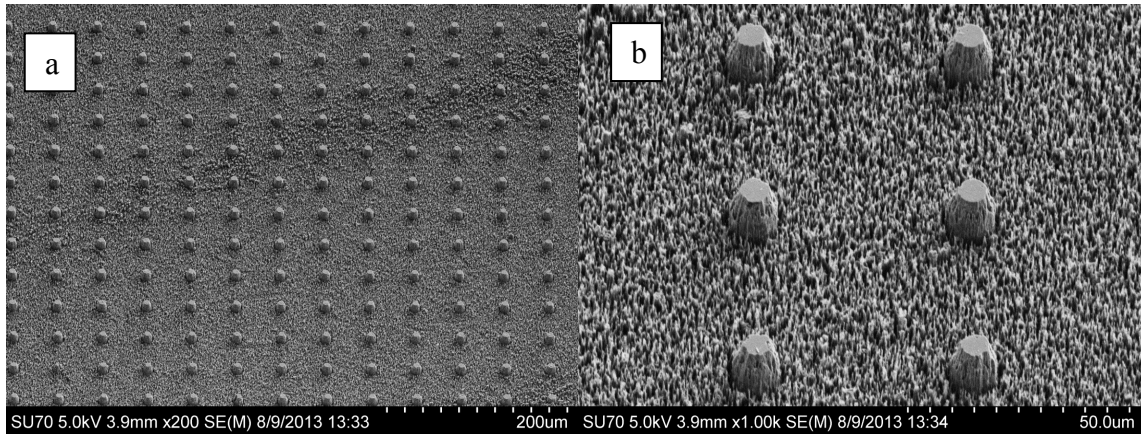
Figure 21 – SEM image of pillar array. (a) 200x magnification, 45 degree tilt on SEM axis.   This image illustrates the uniform separation between pillars.   (b) 1000x magnification, 45 degree tilt on SEM axis. This image illustrates the rough surface left on the surface from the CF_4-O_2 gas mix, where laser excitation generated requisite heat for decomposition.

This method produced pillars with smooth, flat tops. These pillars, as shown in

Figure 21(b), are ideal for furnace growth experiments.   However, initial SiC

decomposition attempts in the ARES system showed substantial growth off of the pillars as opposed to the top of individual pillars. This was in disagreement with the pre-conceived notion that the pillars would provide thermal isolation and thereby facilitate SiC heating and decomposition. Given success at forming carbon nanostructures on the roughened off-pillar surface, the pillars were roughened post-Ni removal with a short, 5 min RIE etch. This roughened pillar top is believed to aid in concentrating the laser emission on a small volume of SiC.

Since the laser excitation method has the capability to perform unique experiments on individual pillars, there is an inherent requirement to monitor experiment locations. An additional mask was used to create a grid pattern on the SiC wafer, shown in Figure 22, to facilitate identifying experiment locations. The grid pattern consists of 576 cells arranged in 24 rows by 24 columns. Within each cell is a 5 by 5 array of pillars. In total, there exists 14,400 individual pillars.
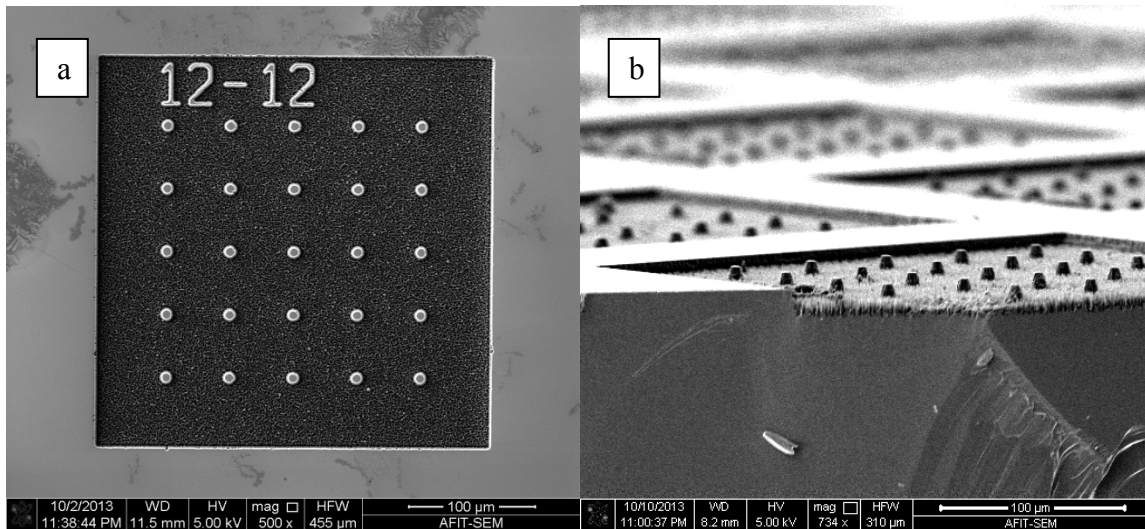
Figure 22 – SEM image of the grid pattern used for the laser excitation mask. (a) 500x magnification of cell 12-12. (b) 734x magnification image displaying etched grid pattern.

3.3 Carbon Nanostructure Growth

The SiC decomposition method used to grow nanostructures (CNTs and graphene) is based on research by Kusunoki [25], Mitchel [16], Pochet [17], and Campbell [18]. The basic thermal decomposition method involves heating a SiC substrate to 1700°C while maintaining a constant vacuum pressure between 10^{-3} and 10^{-6} Torr. The heat source for this research was derived from two different sources: graphite resistance furnace and excitation from a 532 nm, 2.5 W laser. The graphite resistance furnace, manufactured by Oxy-Gon Industries Inc, Epsom, NH, is overseen by AFRL/RXAN and the laser excitation apparatus is overseen by AFRL/RXAS.

3.3.1 Oxy-Gon Graphite Resistance Furnace

Carbon nanostructure growth via graphite resistance furnace is described in this section. The operating procedure for the furnace is found in Appendix B. In summary, the temperature in the heating volume is controlled by the current running through the furnace. The various temperatures investigated in this research are provided in Table 1 and typical ramp plots are displayed in Figure 23 and Figure 24. Both plots show the soft bake process as a flat line at 1250°C. The chamber pressure increases when the temperature increases, as depicted by the blue line. The percentage of current flow controls the rate at which the temperature increases. A turbo-molecular pump controls the pressure of the chamber. A roughing pump lowers the pressure to $10^{-2} – 10^{-3}$ Torr, which assists the turbo-molecular pump in bringing the pressure down to $10^{-5} – 10^{-6}$ Torr. Chilled water is circulated within the skin of the furnace to allow the exterior to stay at a temperature which is safe to touch. Figure 25 is an example of the Oxy-Gon furnace used in this research. The control module is on the left and the oven is on the right.
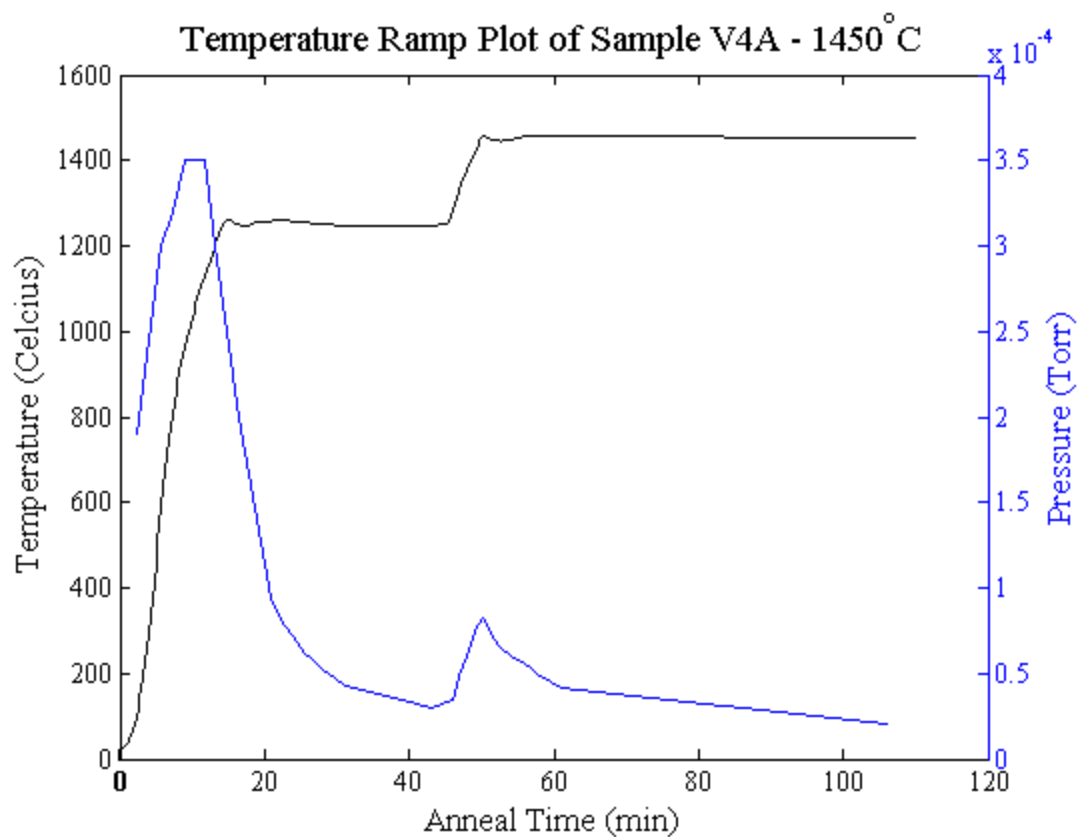
Figure 23 – Temperature ramp plot for sample V4A. The black line represents temperature and blue represents pressure.
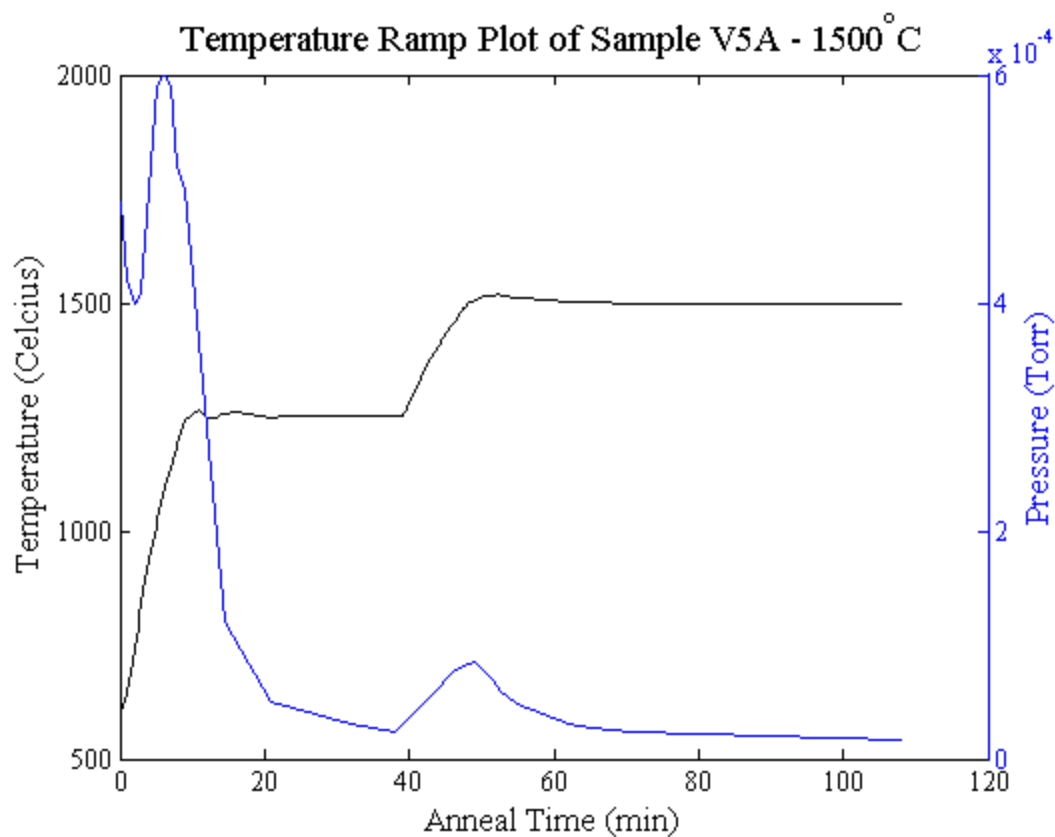
Figure 24 – Temperature ramp plot for sample V5A. The black line represents temperature and blue represents pressure.

Table 1 - List of temperatures used in vacuum furnace experiment

Sample	Temperature	Annealing Time (min)
4-1A	1700	180
5-1A	1650	60
5-1B	1600	60
5-3A	1550	60
5-3B	1500	60
5-4A	1450	60
5-4B	1400	60
5-5A	1350	60
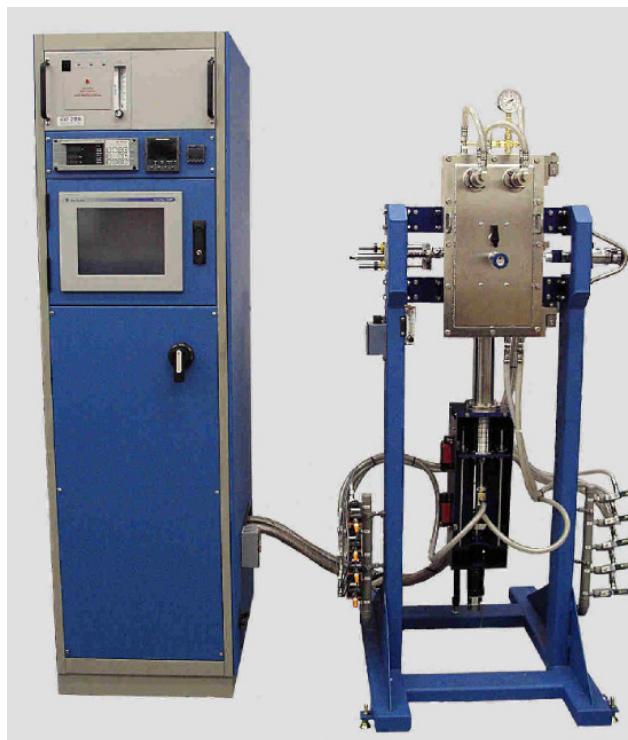
Figure 25 – Picture of an Oxy-Gon graphite resistance furnace. The left tower houses the user controls for the vacuum and electrical power systems. The oven chamber is on the right.

3.3.2 Laser Excitation Chamber

Carbon nanostructure via laser excitation is described in this section. A patterned SiC wafer is affixed to the sample holder by double sided copper adhesive. The sample holder is then mounted into the vacuum chamber, which has a volume of approximately 1 in^3. While in the chamber, a 50X magnification objective focuses the laser to a 4 μm^2 spot on the wafer. A roughing pump lowers the chamber pressure down to $10^{-3} - 10^{-5}$ Torr. Once the target pressure is reached, the laser is powered up to 2.5mW, and the wafer begins to heat. While it is heating, the scattered laser light is collected by an optical lens and sent to the Raman detector. The resulting Raman spectrum reveals *in situ* growth kinetics.

The setup and operation of the ARES system was controlled by AFRL. Table 2 displays a list of experiments that were conducted during the course of this research. Remembering the focus of this research, the purpose of the laser excitation method is to duplicate the environmental condition found in the Oxy-Gon furnace: pressure near 10^{-5} Torr, water concentration less than 5 parts per million (ppm), 60 minute growth time, and an absence of a chamber gas. With regard to these considerations, few experiments fit the criteria mentioned above. Of the experiments performed, only Trials 1, 2 and 12 most resembled the Oxy-Gon furnace chamber conditions.

Table 2 - List of laser excitation experiments

Trial	Location	Pressure (Torr)	Water Concentration (ppm)	Excitation Time (min)	Gas
1	Pillar	3.10E-06	1.94	80	Vac
2	Substrate	3.27E-06	2.41	86	Vac
3	Substrate	1.20E-05	7	56	Vac
4	Substrate	5.50E-05	11	68	Vac
5	Substrate	7.00E-05	20	95	Vac
6	Substrate	8.00E-04	2.15	100	Argon
7	Substrate	1.20E-03	1.76	69	Argon
8	Substrate	1.23E-03	1.69	38	Hydrogen
9	Substrate	2.60E-03	50	51	Vac
10	Substrate	6.00E-03	66	53	Vac
11	Pillar	unknown	2.8	15	Vac
12	Substrate	unknown	3.5	52	Vac
13	Substrate	unknown	3.5	24	Vac

3.4 Raman Spectroscopy

Significant insight comes from comparing the Raman spectra generated from the furnace oven growth process against the laser growth process. As described in Chapter II, Raman spectroscopy is a laser measurement technique used to observe low-frequency modes in a system, such as vibrational and rotational modes. It relies on inelastic scattering of monochromatic light from a laser in the ultraviolet, visible, or near infrared

range (300 – 900 nm wavelengths). For this laboratory work, 514 nm and 532 nm wavelength lasers are used to gather Raman scattering data. The 532 nm source is used in the ARES system and the 514 nm source is used in the stand-alone Renishaw device. In either system, the laser light interacts with molecular vibrations resulting in the energy of the laser photons being shifted up or down the energy spectrum. The shift in energy reveals information about the atomic vibrational modes in the system [33]. In this research effort, carbon – carbon bonds are the focus in Raman spectroscopy.

A Renishaw device, similar to the one shown in Figure 26, is used to collect Raman data on nanostructures grown in the vacuum furnace. First, the instrument is calibrated first with an internal, then again with an external Si source. A Raman peak of 520 cm^{-1} (+/- 1 cm^{-1}) verifies the instrument is calibrated correctly. Once calibrated, the SiC sample is placed on the stage under the microscope. A camera captures the image from the microscope which is displayed on a monitor in order for the user to focus the 4 μm^2 laser spot size on the surface of the sample. An example screen shot from the monitor is displayed in Figure 27. An extended scan mode is selected for a 10 second scan. The shutter opens, allowing the laser beam to illuminate the sample surface. The spectrum data is saved as a text file and plotted in Matlab where it is analyzed and presented in Chapter IV.

Figure 26 – An example of the Renishaw device used in this research. On the left is the sample stage with the optional safety cover open. The cabinet on the right contains the laser optical components [43].
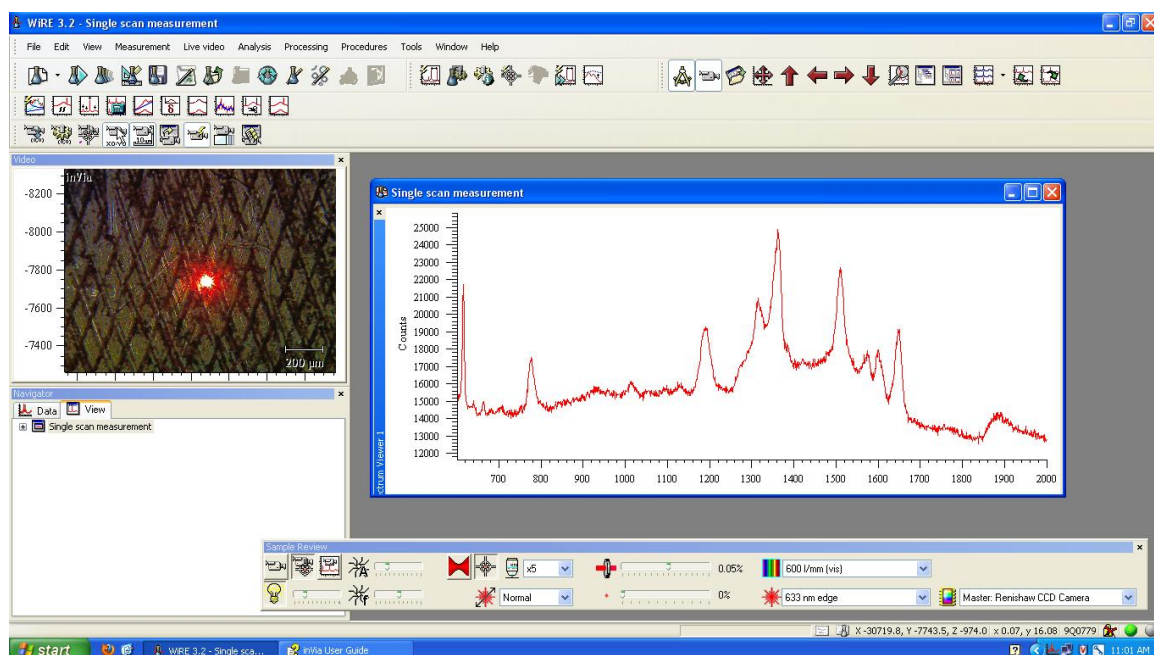
Figure 27 – Example of a screen shot from Raman software courtesy of Micro and Nanotechnology Laboratory at University of Illinois [44].

The collected Raman data will be used to compare the nanostructures grown via

Oxy-Gon furnace with structures grown via laser excitation. First, Raman data collected

from different annealing temperatures used in the Oxy-Gon furnace will be examined to reveal any trends relating material characteristics to temperature. Additionally, Raman spectroscopy will be used to compare material grown on pillar tops with material grown on the etched substrate. It is proposed that a comparison of Raman spectra will reveal thermal decomposition produces a conformal material covering all surfaces on the substrate. Second, in-situ Raman data collected from the laser excitation growth method will be examined to reveal any trends relating material characteristics to chamber pressure and excitation time. By varying the chamber pressure and maintaining consistent laser power, it is proposed that the Raman spectra will reveal a direct relationship between material growth and chamber pressure. Lastly, Raman spectra from the furnace method will be compared to spectra from the laser excitation method via superposition. If chamber conditions are identical between the two methods (temperature and pressure), it is anticipated for their respective Raman spectra to be identical as well. Results of D, G and G' peak position and line width comparisons are provided in the following chapter.

3.5 Summary

This chapter covered the main procedures required to accomplish this thesis work. It first discussed the pre-processing required to pattern the SiC wafers. Then the chapter talked about the two different methods used to grow nanostructures: furnace and laser excitation method. This chapter concluded with a discussion on how Raman spectroscopy was used to collect data. The Raman data is used in the next chapter to compare the two growth methods.

IV. Analysis and Results

4.1 Chapter Overview

The purpose of this chapter is to report on findings, based on collected data from the methods described in the previous chapter. The first section discusses key findings discovered during the pre-process sequence where the primary variant in achieving tall, crisp pillars was the thickness of the sacrificed Ni mask thickness. Next, nanostructures grown using the vacuum furnace are examined; characteristic growth variables such as temperature ramp and chamber pressure were varied, and are discussed. Characteristics of carbon nanostructures grown by the laser excitation method are discussed, with attention paid to background pressure and gas type. Finally, the last section compares the material grown by both methods. Data collected from Raman spectroscopy is inspected; similarities between the two growth methods are discussed with hopes of using the ARES growth data to form a growth matrix similar to that presented by Song and Smith [28]. While this was not achieved to the level initially desired, the data from the ARES growth runs highlights material grown on the substrate is similar to material grown a pillar, no graphitic material was produced, and chamber pressure may be the most significant factor to consider.

4.2 Sample Patterning

The initial step in this research was pre-processing SiC wafers to create arrays of 10μm tall pillars, 10μm in diameter. Several factors played a role in obtaining the optimum yield, dimensions and shape of the SiC pillars. It was observed that the thickness of the photolithographic mask and the thickness of the deposited Ni layer had a

direct impact on how well the pattern transferred to the SiC wafer. The size and shape of the pillars ultimately relied upon the combination of gasses, pressure and RF power selected in the RIE instrument, along with the Ni mask thickness.

For this research work, a total of three photolithographic masks were fabricated using AFIT's Heidelberg µPG 101 Tabletop Laser Pattern Generator. Mask 1 was developed on a 0.090 inch thick glass substrate, Mask 2 was on a 0.060 inch substrate, and Mask 3 was on a 0.090 inch substrate. Mask 1 was exposed to a pattern with 10µm circles, spaced 50µm apart. This mask was used to successfully pattern 20 SiC sample pieces, each approximately 1 cm x 1 cm. Mask 2 was exposed to a pattern with 12µm circles spaced 50µm apart, similar to the pattern used in Mask 1. However, when Mask 2 was used in the MJB3 mask aligner, it resulted in inconsistent pattern development.

When obtaining a blank mask for pattern creation, little thought went into the thickness of the blank photo mask glass plates. AFIT's cleanroom offers two choices: 0.060 and 0.090 inches. Both thicknesses of masks are 4 in x 4 in, and are the optimal size for a 3 inch diameter wafers. Since a 3 inch wafer comprises 44% of the area of the mask, as shown in Figure 28(A), when the mask and the wafer come in contact, the mask overhangs the wafer by 0.5 inch. This relatively small overhang results in a large moment of inertia ($I=bh^3/12$, b=over hang, h=thickness) which prevents mask deformation under minimal compression force. However, this research effort utilizes a 1 cm by 1 cm wafer sample. This area is only 1% of the total glass mask area. Therefore, when the glass mask comes in contact the SiC wafer sample, the mask overhangs each side by 1.8 inches, decreasing the moment of inertia created by the mask when compared to the 0.5 inch overhang. This sample-to-mask effective area ratio is illustrated in Figure

28. Additionally, Mask 2 is much more sensitive to compression forces (h^3) when it comes in contact with the wafer since it is thinner than the other two masks at 0.060 inches.
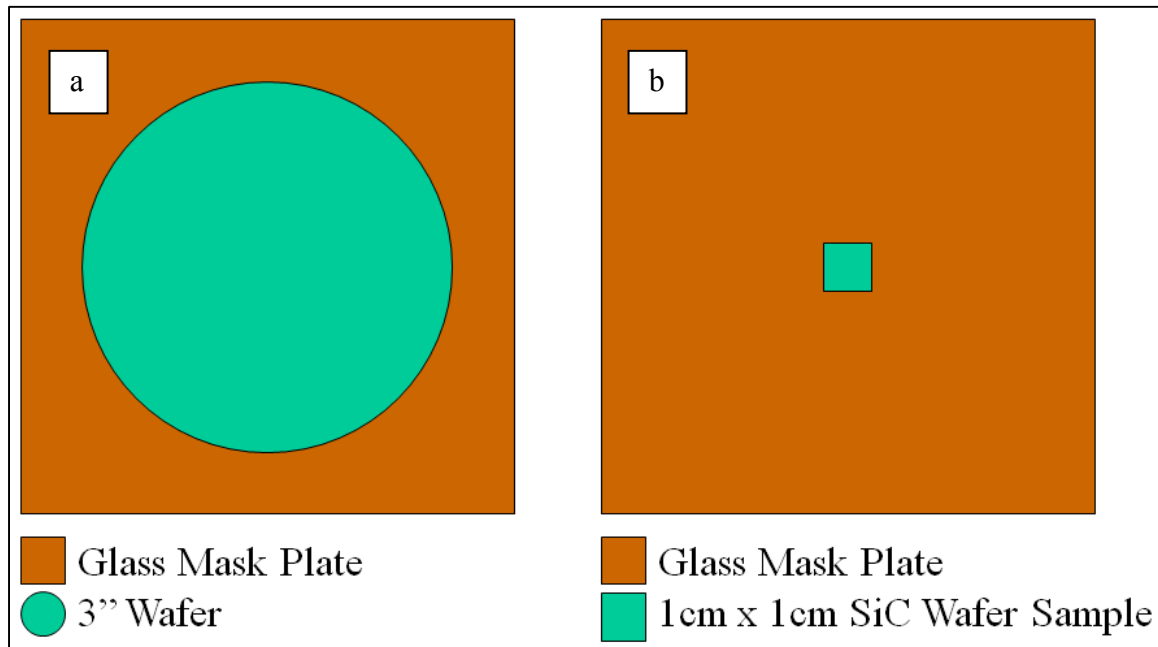
Figure 28 – The images above emphasize the relative areas of the glass mask to a 3 inch wafer and a SiC wafer sample used in this research.

Mask 2 was used to expose a set of five SiC wafer samples, coated with PR, to the 12μm pattern. While the samples were being developed in 351, it was observed that the pattern did not uniformly transfer to the PR on the wafer samples. Instead of a uniform array of circles, a diffraction-like pattern was observed. It was determined that the glass mask plate deformed while making minimal contact with the wafer sample. The stresses inside the glass mask plate, particularly in the area above the wafer sample, obstructed the UV light, preventing it from properly exposing the PR beneath it. As shown in Figure 29, the stress pattern on the mask appears as wavy lines on the surface. The refraction pattern blocks the UV light from passing through, and thereby gets transferred to the

wafer sample as unexposed areas of PR. Mask 3 was intentionally fabricated on a 0.090 inch glass mask to avoid this anomaly. This conclusion was in part formed through discussions with AFIT's cleanroom technicians. It should be noted that this phenomenon was previously observed by Campbell whose SEM image is shown in Figure 30.
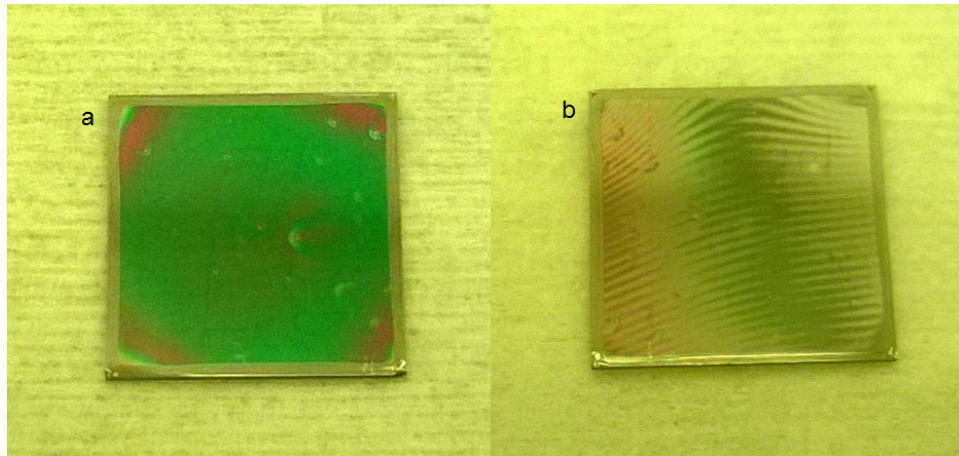
Figure 29 – Photograph of 1805 PR on SiC substrate. (a) was taken after the sample is exposed to a UV source. (b) was taken after the sample was developed in 351. The pattern displayed on the developed PR is caused by the use of a 0.060 inch thick mask.

The original reason for creating Mask 2 was to obtain larger SiC pillars, both in diameter and height. The diameter of the pillars is determined by the diameter of the patterned Ni layer. However, during the Ni etching process (wet etchant based), a degree of undercutting occurs by approximately $1 - 2$ μm, resulting in $8 - 6$ μm diameter circles. In order to compensate for this loss, 12 μm circles were used in Mask 2 in lieu of 10 μm circles found in Mask 1. With the diameter of the pillars being determined by the mask features, the height of the pillars can be considered next.
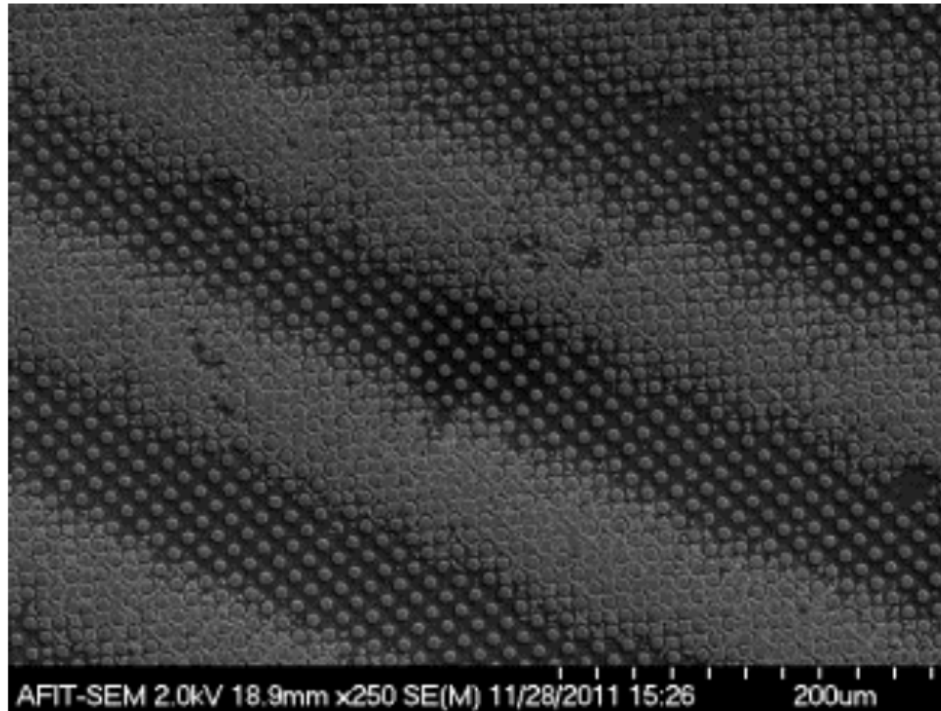
Figure 30 – SEM image captured by Campbell further illustrating the transfer of the diffraction pattern to a SiC substrate [18].

The height of the pillars is determined by two factors: 1) thickness of Ni layer and 2) etch parameters used during RIE (i.e.: power, duration, volatile gas mixture, plasma density). Keeping the etch parameters constant, it can be assumed that varying the Ni thickness will directly affect pillar height. Initially, Ni was deposited to a thickness of 2200Å and the average pillar height was measured to be 7 μm, as displayed in Figure 31. When placed in the RIE, the Ni layer acts as a mask, protecting the SiC material beneath it. While exposed to the etching plasma, both the Ni mask and SiC wafer react with the ions. Since the chosen gas mixture (CF_4) has a selectivity of 15:1 (SiC : Ni), the SiC is etched faster than the Ni mask. However, during the 3 hour etch time, the Ni is completely etched away, given the etchant selectivity ratio. This etch ratio was partially investigated by performing the RIE in 30 minute blocks; after each block, the sample was

54

studied using an optical microscope, profilometer, and SEM to determine the pattern states. When the Ni is etched away, further RIE is ceased and the resulting pillar height is ~7 μm. Given this failure to reach a 10 μm etch depth, it was proposed that increasing the Ni thickness would add more protection to the SiC and allow a deeper etch in the RIE.
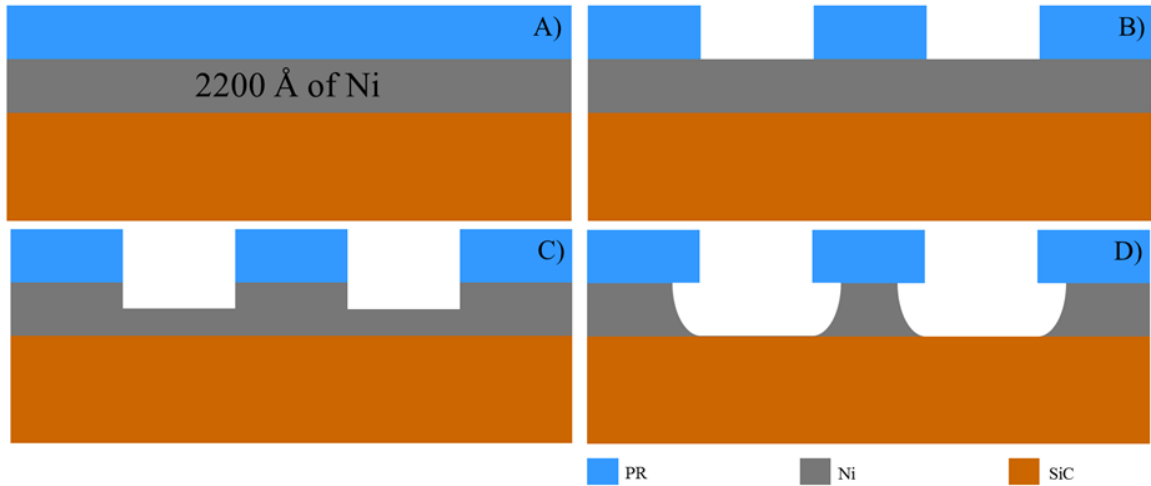
Figure 31 – The image above outlines the process of utilizing a 2200 Å thick Ni mask. The remaining Ni seen in **D)** is thick enough to allow suficient time in the RIE to create SiC pillars ~7 μm high.

A set of five SiC wafer samples were deposited with 4000 Å of Ni, in hopes of obtaining pillars greater than 7 μm in height. The samples then followed the same procedure to pattern the Ni into arrays of 10 μm circles: coat with 1805 PR, UV exposure to Mask 1, develop in 351, rinse in DIW, place in Ni Etchant, as illustrated in Figure 32. The average etch time required to pattern 2200 Å of Ni was 4.5 minutes in 50°C Ni Etchant. Therefore, in order to etch 4000 Å, an estimated etch time of six minutes was expected. Unfortunately, the Ni was too thick to be properly etched by the Ni Etchant, as the etch rate decreased with the additional Ni thickness.

After being held in the Ni Etchant for five minutes, a wafer sample was removed and examined under an optical microscope. Upon inspection, it was observed that several PR circles broke free from the Ni surface, before the Ni was etched down to the SiC wafer. From this observation, it was determined that because the Ni Etchant solution etches isotropically, the sidewalls of the patterned Ni completely under etched the protective PR pattern layer. Figure 32 illustrates what happens when the Ni deposition thickness is increased to 4000 Å.
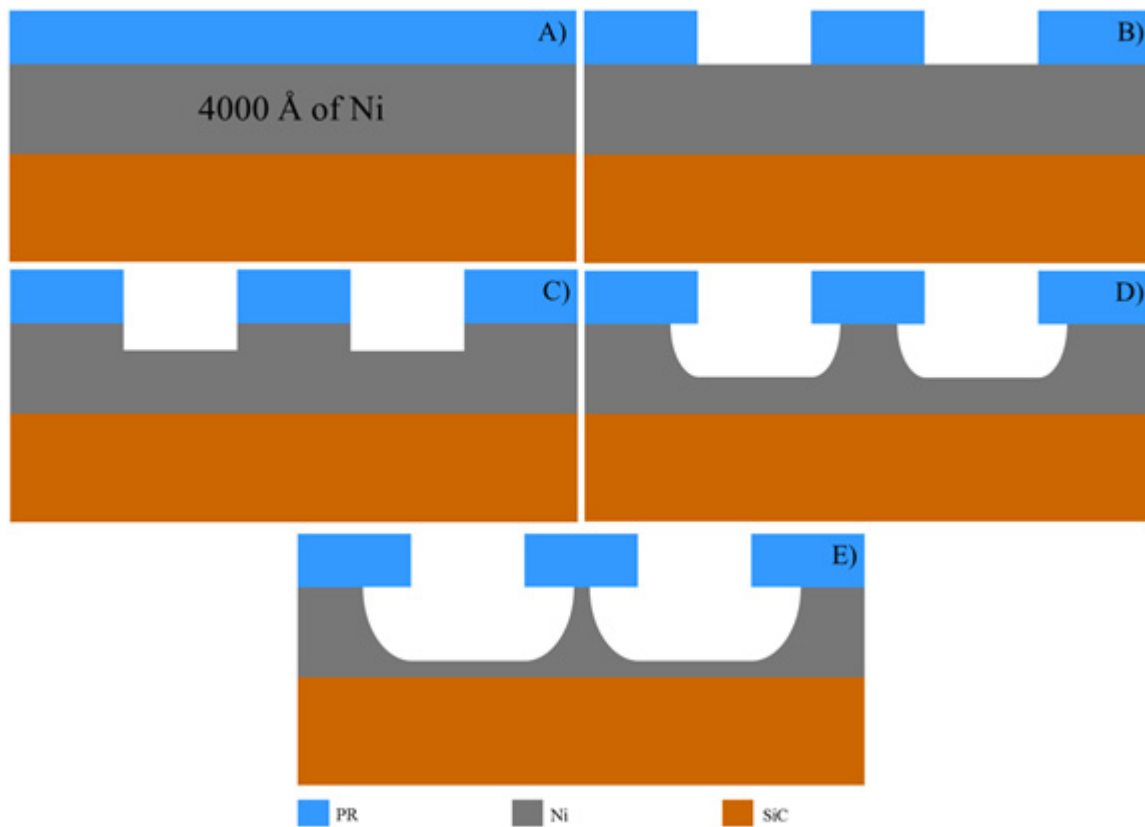
Figure 32 – The image above outlines the process of utilizing a 4000 Å thick Ni mask. Steps **A)** through **D)** are the same steps used in the thinner 2200 Å Ni layer. Step **E)** highlights the severe undercutting due to the isotropic etch pattern consistent with a wet etching technique.

The last element of the pre-processing step to be considered is the flatness of the SiC pillars. Prior to this work, only flat pillars were considered. When only utilizing the

vacuum furnace method to decompose SiC, flat-topped pillars are ideal. With flat pillars, it is easy to measure material growth via SEM, and the diameter of the pillars concentrate CNTs to a small area which is critical for field emission, as discussed by Campbell [18]. However, when the flat SiC pillars were used in the laser excitation system, the concentration of heat sufficient to thermally decompose the SiC was not achieved. Historical growth in the ARES system involves Si pillars on SiO_2; the SiO_2 enables each pillar to be thermally isolated. The hope in this work was for the tall SiC pillars to provide enough thermal isolation to enable thermal decomposition of SiC.

Prior to this research work, the ARES system employed silicon-on-insulator (SOI) wafers as its growth substrate [15]. With fabricated Si pillars resting on a foundation of SiO_2, the heat generated by the laser was able to concentrate within the specified pillar. The purpose of the SiO_2 is to inhibit the transfer of heat throughout the entire wafer. Although the spacing and dimension of the SiC pillars were designed to mimic the features found on the SOI samples (with the purpose of creating a thermal barrier), it was the insulating layer which proved essential for thermal isolation. The SiC material used in this research did not have an insulating layer. Subsequently, when a flat topped pillar was heated by the laser, there was no thermal barrier between the pillar and the rest of the substrate, and the heat dissipated throughout the SiC wafer. The laser did not generate enough heat to thermally decompose the SiC. Exploring other features on the wafer sample with the laser proved successful in producing carbon nanostructures.

Focusing the laser on the etched substrate, rather than the flat pillar tops, generated enough heat to thermally decompose the SiC wafer. The reasoning behind this finding is since the etched surface is composed of jagged features due to the micro-

masking effect, the laser beam reflects off of the surfaces and is focused into the substrate within an area ~ 4 μm. This method of containing laser energy led to the idea of creating pillars whose top surfaces resemble the jagged substrate, as illustrated in Figure 33. It was proposed that the rough pillar tops would concentrate the laser energy within the pillar in lieu of a layer of insulator below the SiC pillars. It was this realization that enabled SiC pillars to be a viable substrate in the ARES system.

Rough pillar tops were concluded to be essential in the laser excitation method because they concentrate the energy of the laser within the nano-scale surface roughness features, allowing temperatures to reach above 1400°C, requisite to thermally decompose the SiC and create carbon nanostructures. It is assumed that the flat top pillars allowed the energy from the laser to enter the material with little resistance, and the substrate dissipated the heat throughout the wafer.
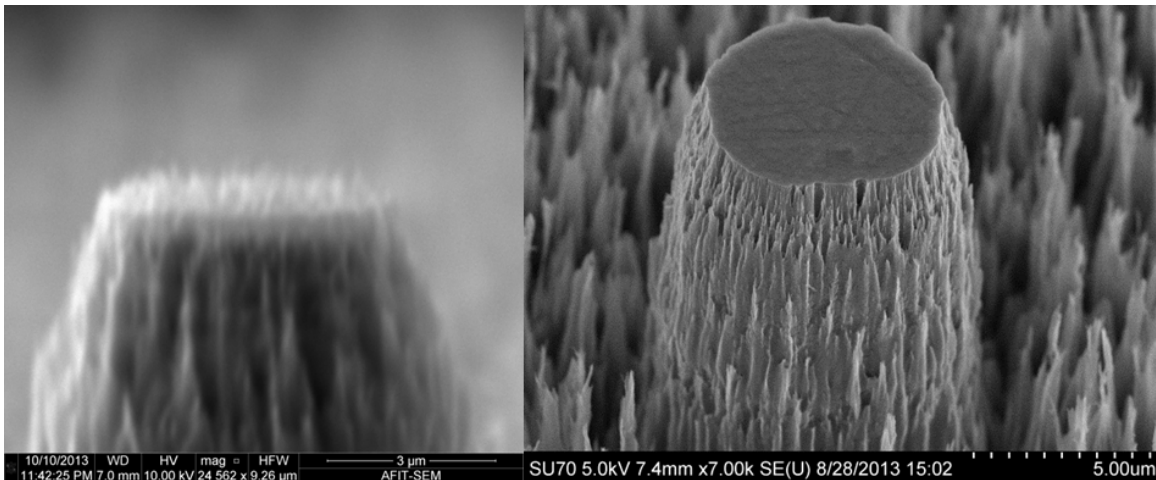
Figure 33 – The image on the left is of a SiC pillar with a rough top. The image on the right is of a flat topped pillar. The rough surface is caused by the micro-masking effect from the RIE process.

4.3 Carbon Nanostructure Growth

After the SiC wafers were patterned into arrays of pillars, they continued to the next step of growing carbon nanostructures using the vacuum furnace or laser excitation methods. Results from the Oxy-Gon vacuum furnace are reported in this section, and results from the laser excitation chamber are reported in the subsequent section.

4.3.1 Oxy-Gon Furnace Growth Results

Figure 34 is a cross section view of a SiC pillar captured via SEM with an 8000X magnification following a three hour growth at 1700°C. Once the wafer was allowed to cool to room temperature, the sample was taken into AFIT's clean room where it was manually cleaved in half. A cleaved half was then mounted on a sample holder and placed in the SEM. After the image was captured, the magnification was increased to 25000X in order to measure the thickness of nanostructure material grown on the flat surface of the pillar. Figure 35 displays the higher magnification image. A total thickness of 310 nm lends to a growth rate of 100 nm per hour; this growth rate was consistent with Si-face growth as reported by Boeckl *et al.* in [30].
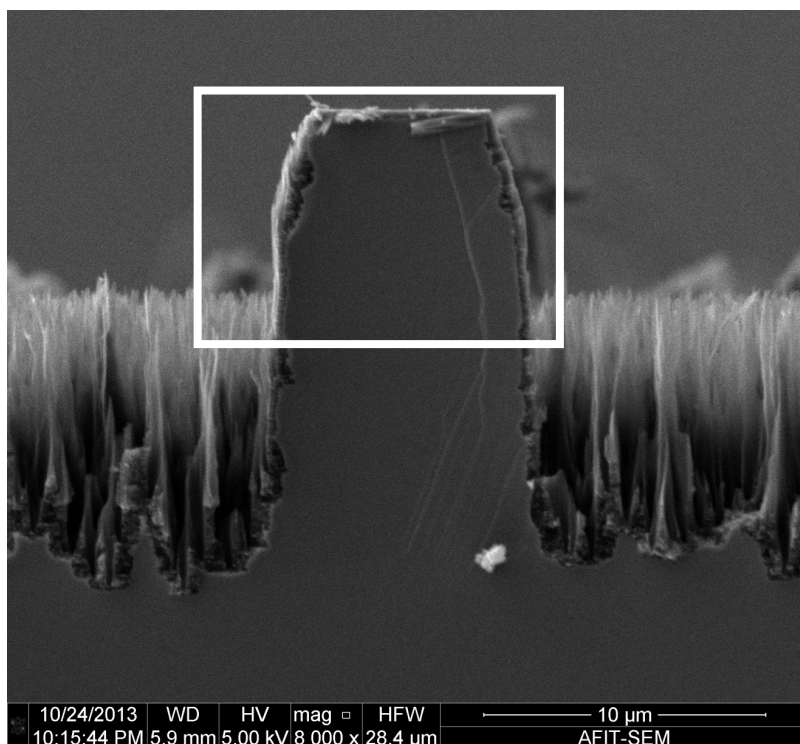
Figure 34 – SEM cross-sectional view of a SiC pillar after 3 hour growth at 1700°C under high vacuum conditions (10^{-5} Torr). The highlighted area is shown in **Figure 35**.
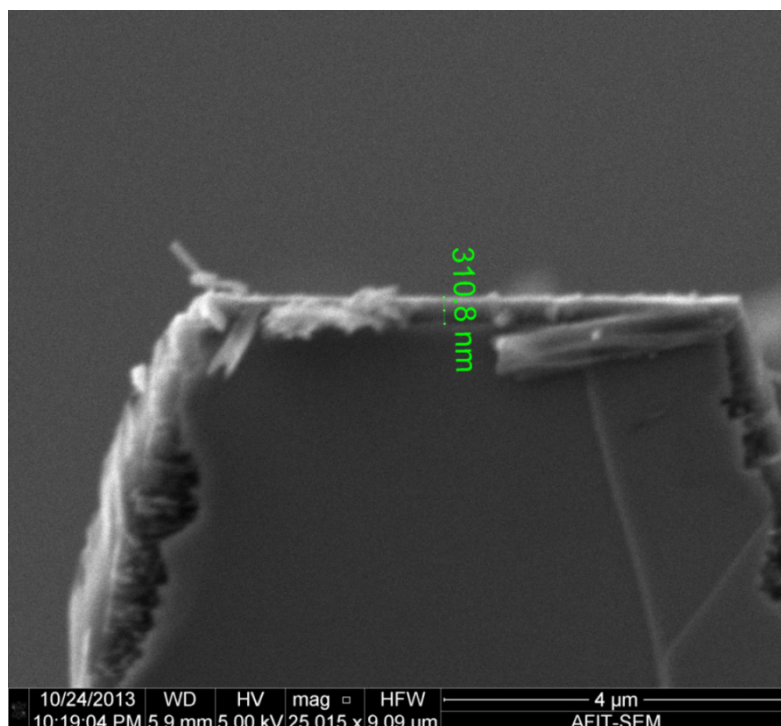
Figure 35 – 25000X magnification zoom of the previous figure. The nanostructure material thickness is 310 nm, produced from 3 hrs in the furnace. This suggests a growth rate of 100 nm per hour.

After the samples were examined under the SEM, they were then placed in the Renishaw Raman microscope to gain insight on the type of carbon allotrope grown on the surface. Figure 36 is the Raman spectrum obtained from a sample after a three hour anneal at 1700°C. Scanning from left to right, the prominent peaks are D, G and G'. The G peak is greater than the D peak supporting the presence of slightly ordered CNTs. The relatively strong G' peak is indicative of graphene layers. This supports the theory Kusunoki *et al.* suggest of graphene forming at temperatures lower than temperatures needed for CNT formation. As the temperature is ramped from room temperature to 1700°C, the temperature holds for 30 minutes at 1250°C to soft bake the surface. It is during this soft bake where it is theorized that layers of graphene form on the surface [27]. These layers of graphene are required for nanocap formation, which in turn are necessary for CNT growth on SiC wafers [27]. The strong G' peak found in the Raman spectrum indicates graphitic layers are present in the material.
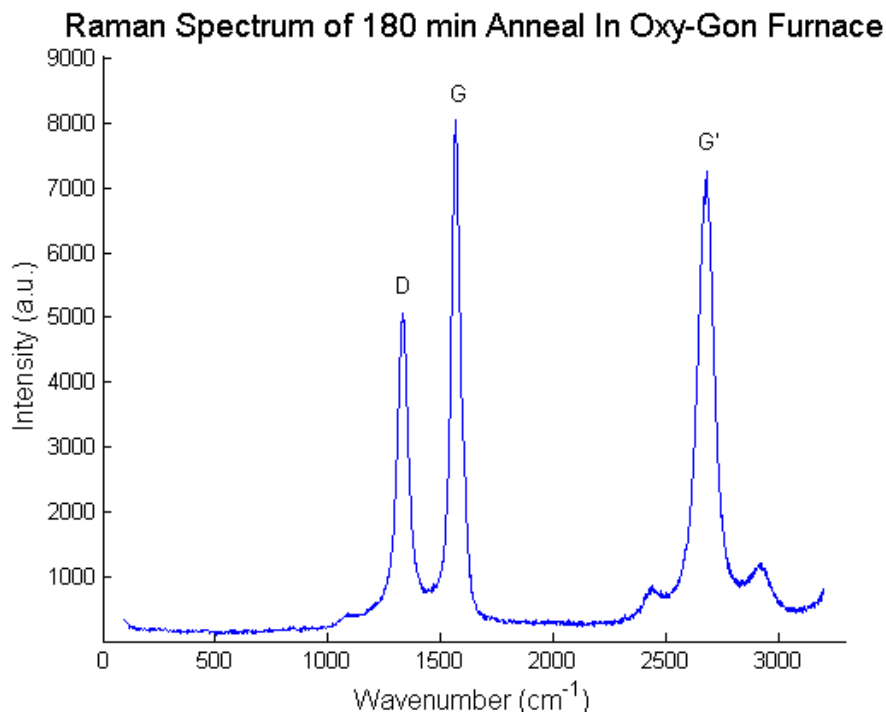
Figure 36 – Raman spectrum of material produced using the Oxy-Gon furnace. The three peaks represent the D, G, and G` bands (left to right). The G` band is an indication of layers of graphitic material. Note the wavenumber ranges from 0 to 3000 cm^{-1}.

Additional growths were performed for temperatures ranging from 1400 – 1650°C in 50°C increments in order to decipher the influence of temperature on the atomic structure of the resulting material. The Raman spectra arising from this range of growth temperatures are presented in Figure 37.

Initially, 1650°C was intended to be the subsequent annealing temperature; however, during the intended one hour annealing time, the vacuum furnace was left unattended and the temperature slowly ramped up to 1775°C. Taking the entire data set into consideration, it is observed from Figure 37 that the highest three temperatures grew material with highly ordered CNTs. Focusing on just the 1500°C and 1550°C temperatures, a large disparity is seen between the two spectra at the D, G and G' peaks. This disparity suggests, for this particular Oxy-Gon vacuum furnace, to yield ordered

CNTs, the temperature must be set at or above 1550°C. Of all the temperatures studied, 1600°C resulted in more refined nanostructures, having the largest G to D band ratio. Table 3 depicts this intensity comparison between the various temperatures.
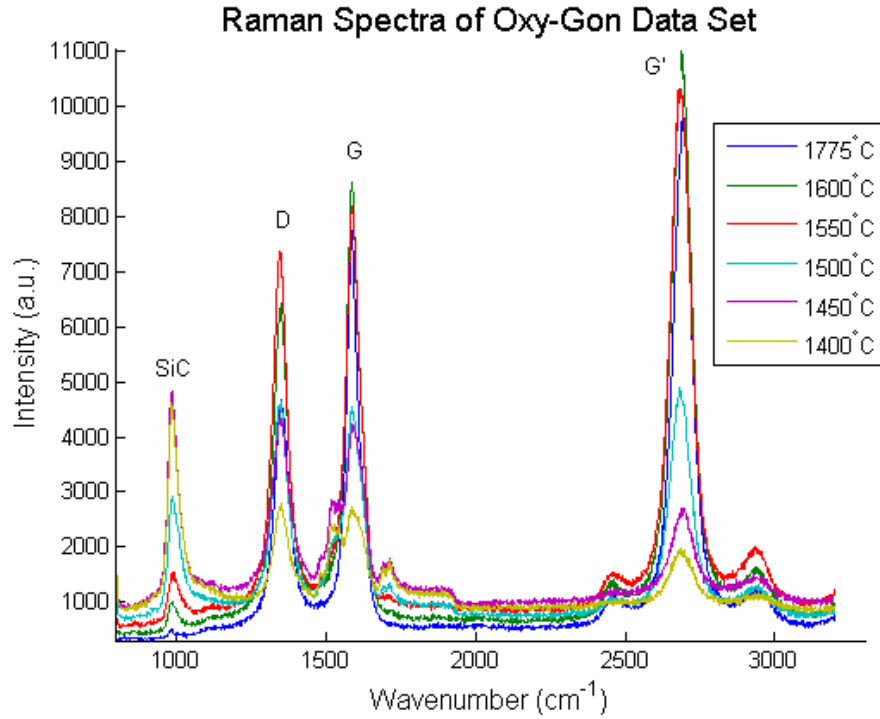
Figure 37 – The plot above displays the complete data set of the Oxy-Gon furnace experiments.

Error! Reference source not found. compares the Raman spectra from 1400°C, 1500°C and 1600°C temperature anneals, and highlights the spectra change as a function of temperature. Similar to Figure 37, the spectra suggest the greater the temperature anneal, the more efficient the system is at producing ordered carbon nanoparticles. The plot clearly shows the affect temperature has on material characteristics during growth. The characteristic carbon peaks (G and G') increase with temperature. The ratio of G to SiC peak intensity increases with temperature, suggesting carbon growth on the SiC surface increases with temperature as well.

Table 3 - Intensity comparison from Oxy-Gon furnace growth

Temp (°C)	I_D/I_G	I_{SiC}/I_G
1400	1.0230	1.6972
1450	1.0231	1.1407
1500	1.0232	0.6423
1550	0.8983	0.1861
1600	0.7480	0.1169
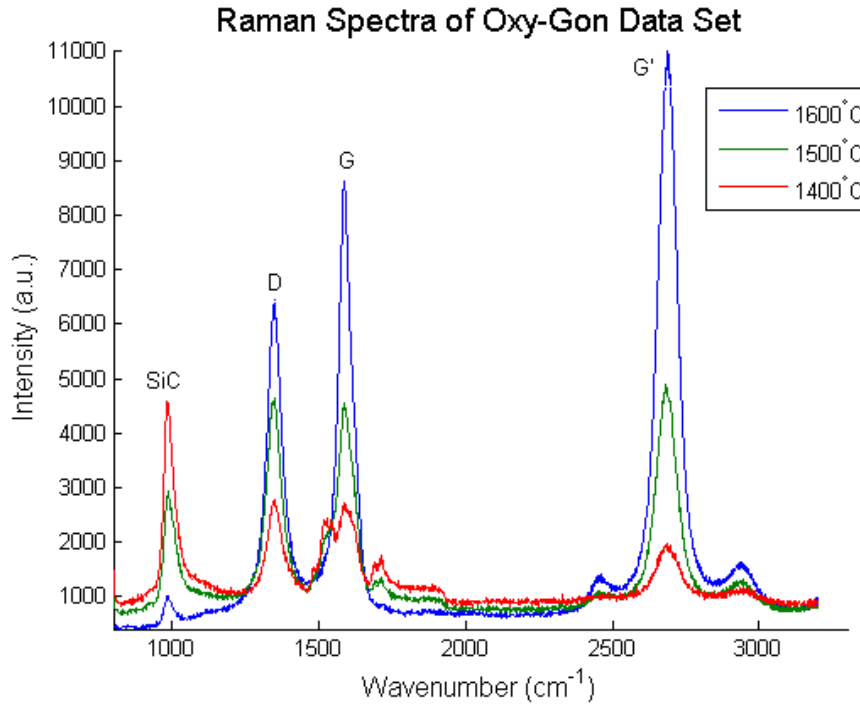
Figure 38 – Raman spectra of 1400, 1500 and 1600°C temperature settings.

One significant data set omitted from the previous figures is the bare SiC wafer. With the SiC wafer line included in the plot, as shown in Figure 39, material growth above the substrate can be easily seen. Noteworthy features of the characteristic SiC wafer line include a prominent peak at 1000 cm^{-1}, two jagged peaks on either side of the G band, and absolutely no G' peak. At the G' location (~2700 cm^{-1}) the SiC wafer line is completely flat, proving no graphitic layers are present.
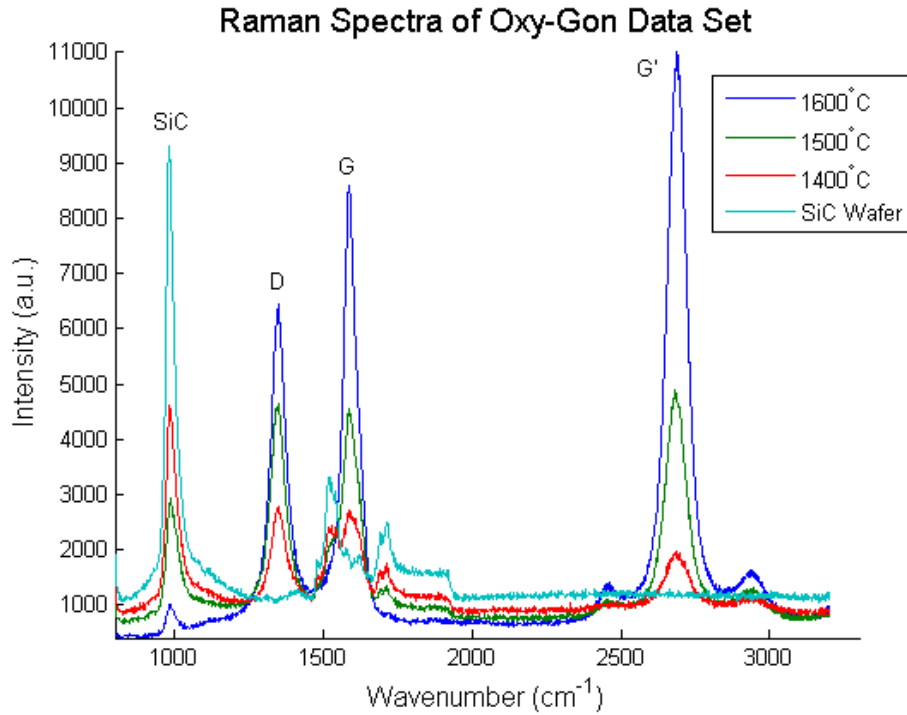
Figure 39 – Raman spectra of 1400, 1500 and 1600°C temperature anneals and the spectrum from a bare wafer with no nanostructure growth. The SiC peak at 1000 cm^{-1} shrinks as the annealing temperature increases.

The Raman data presented in this chapter thus far has been collected from the substrate level of the wafer, not from a pillar location. Summarizing previous remarks, the purpose of the pillars in the vacuum furnace method is to visually observe material growth after the wafer has been cleaved in half. A unique feature of the vacuum furnace method is the ability to conformally grow material on the substrate. The same carbon-rich material is present on top of the pillars as on the etched substrate level of the SiC wafer, as suggested in Figure 40. The figure displays two Raman spectra obtained from different areas on the SiC wafer. The blue line represents material found on the etched substrate, and the black line represents material on top of a SiC pillar. The two lines

65

almost completely overlap, with the only discrepancy being the intensity of the G' peak.

At the G' peak location, the pillar intensity is greater than the substrate intensity.
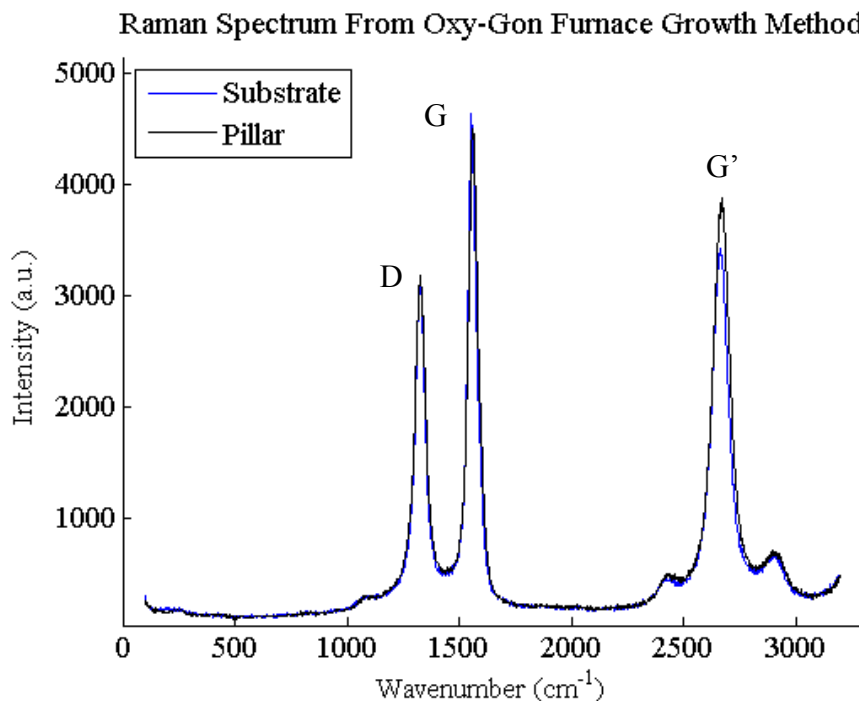
Figure 40 – Comparison of spectra taken from two different areas. The blue line is from the substrate and the black line is from the top of a flat pillar. Since the spectra overlap, it shows the material is consistent throughout the substrate.

4.3.2 Laser Induced Growth Results

This section reports on the data collected from the second growth method examined in this research: laser excitation. As displayed in Table 2, a total of 13 different experiments were conducted in the ARES system. Of those 13, four trials proved to be of significant interest for this research effort. As listed in Table 4, Trials 1, 2, 6, and 12 are deemed as experiments of interest. Trials 1, 2 and 12 are considered relevant due to their having similar chamber settings to the Oxy-Gon furnace. Chamber pressure between $10^{-4} - 10^{-6}$ Torr, minimal water concentration (< 5 ppm), 60 minute growth time, and an absence of chamber gas are comparable to furnace conditions. Trial

66

6, on the other hand, is highlighted in this section due to its impressive ratio of SiC intensity to the G band (I_{SiC}/I_G). All trials were performed in different locations on the same SiC wafer.

Table 4 – Results from experiments of interest from ARES system

Trial	Location	Pressure (Torr)	Water Concentration (ppm)	Excitation Time (min)	Gas	I_D/I_G	I_{SiC}/I_G
1	Pillar	3.10E-06	1.94	80	Vac	0.9193	0.8852
2	Substrate	3.27E-06	2.41	86	Vac	0.9635	0.9333
6	Substrate	8.00E-04	2.15	100	Argon	0.9234	0.6985
12	Substrate	unknown	3.5	52	Vac	0.9322	0.7975

Figure 41 displays the Raman data collected from Trial 1. The 'Growth Time' axis serves as a means to track material growth versus time. Similar to the vacuum furnace Raman data, nanostructure growth is indicated by peaks in the G band location (~ 1580 cm^{-1}) and the D band (~ 1350 cm^{-1}). The plot of the growth evolution shows the gradual increase of the G and D band intensities over time. A comparison of initial and final Raman spectra for Trial 1 is presented in Figure 42. The blue line represents the Raman spectrum from 10 minutes of laser excitation. The green line represents the final Raman spectrum produced at the conclusion of the experiment. The G and D peaks found in the final Raman spectrum show significant growth compared to the initial spectrum. The SiC peak found at 1000 cm^{-1} does not seem to diminish with time. This can be due to the thin layer of carbon allotrope formed along with the penetration depth of the 514 nm laser. It can be presumed that if the surface is severely jagged, then it may allow for laser energy to scatter within the SiC, outside of the growth zone region. The scattered laser energy may then exit the SiC wafer without interacting with the small growth area (~ 4μm).
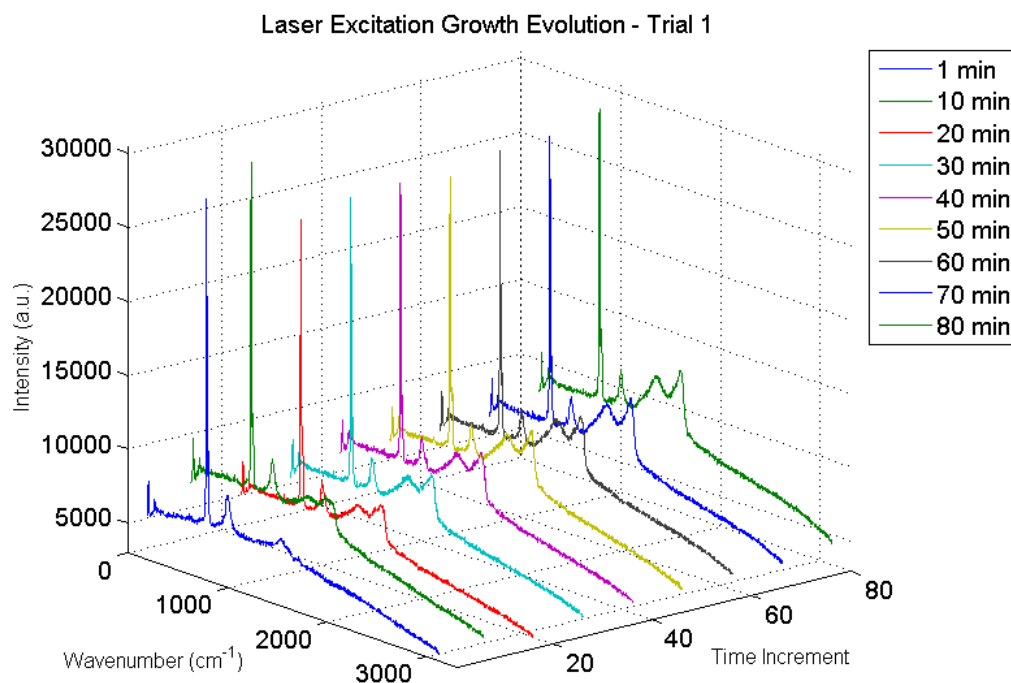
Figure 41 – Laser excitation growth of Trial 1.
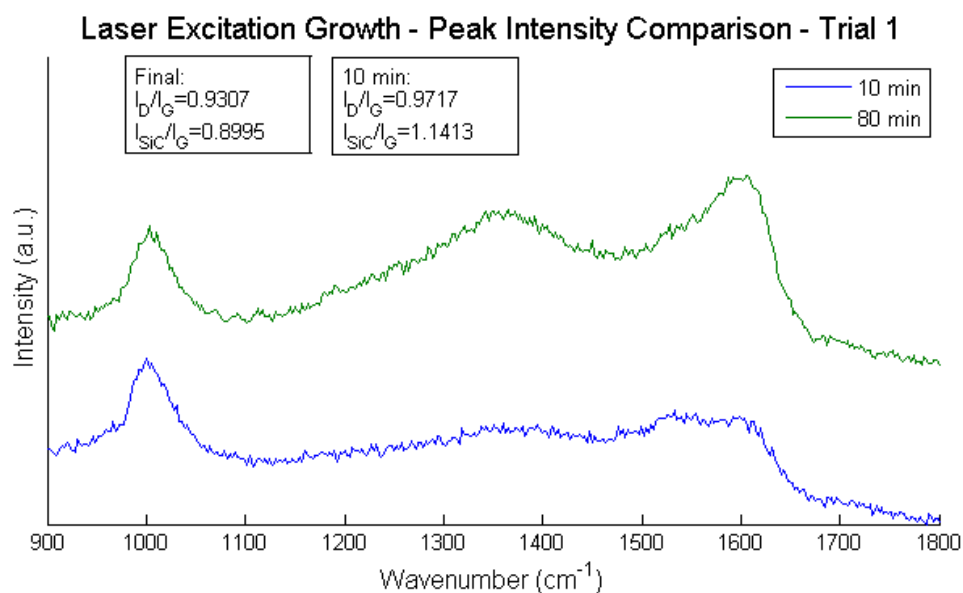
Figure 42 – Comparison of 10 min and final spectra of Trial 1.

Figure 43 displays the Raman data collected from Trial 2. Similar to Trial 1, the

plot of the growth evolution shows the gradual increase of the G and D band intensities

68

over time. A comparison of initial and final Raman spectra for Trial 2 is presented in Figure 44. The blue line represents the Raman spectrum from 10 minutes of laser excitation. The green line represents the final Raman spectrum produced at the conclusion of the experiment. The G and D peaks show significant growth compared to the initial spectrum. The major difference between the setup for Trial 1 and Trial 2 is the location where the laser is focused upon. Trial 1 performed growth on a pillar, whereas Trial 2 grew material on the etched substrate. The largest disparity between the two trials can be seen when the SiC peak intensity is compared to the G band intensity.

Figure 43 – Laser excitation growth of Trial 2.

69
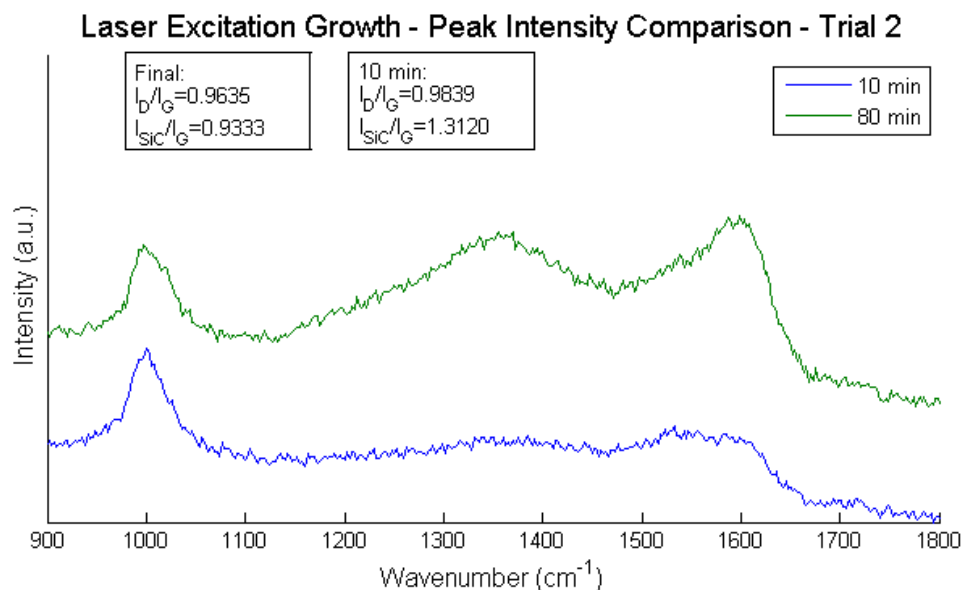
Figure 44 – Comparison of 10 min and final spectra of Trial 2.

Since this is the first time the decomposition of SiC via laser excitation is being reported on, there lies a need for a novel approach to monitor material growth. Unlike the Oxy- Gon method, material growth is limited to a single 4 μm spot, which proves nearly impossible to cleave in half for cross-section viewing in an SEM. Therefore, a peak intensity comparison (I_{SiC}/I_G) is used to determine the amount of carbon material present on a sample. The values of this comparison are displayed in the last column of Table 4. Trial 1 has a growth value of 0.8852 and Trial 2 has a value of 0.9333. This suggests Trial 1 grew carbon material more efficiently than Trial 2, given their excitation times are nearly equal (80 min for Trial 1 and 86 min for Trial 2).

Laser excitation growth data for Trial 12 is displayed in Figure 45. The experimental setup for Trial 12 is different from those of Trials 1 and 2 in several ways. First, unlike Trials 1 and 2, the chamber pressure during the experiment is unknown. Unfortunately this information was not recorded during this trial. Secondly, Trial 12 did not run as long as the other two trials. Trial 12 ran for a total of 52 minutes, whereas the

70

other trials ran at least 80 minutes. The shorter excitation time, however, did not appear to affect the amount of nanostructure growth. From looking at the final G and D bands in Figure 46, it appears their intensities, relative to the SiC peak intensity, are much larger than the peaks found in Trials 1 and 2. The significant nanostructure growth in the shorter amount of time results in a larger growth rate, compared to the data found in the first two trials. The increase in growth rate may come from the difference in chamber pressure. Of the various parameters under consideration during this experiment, the chamber pressure may be the major factor affecting growth rate.

Similarities between the trials begin with excitation region. Trial 2 and Trial 12 are both performed on the etched substrate. Water concentration between the three different trials varies by 1.6 ppm. Within the scope of this research, this variance is negligible.
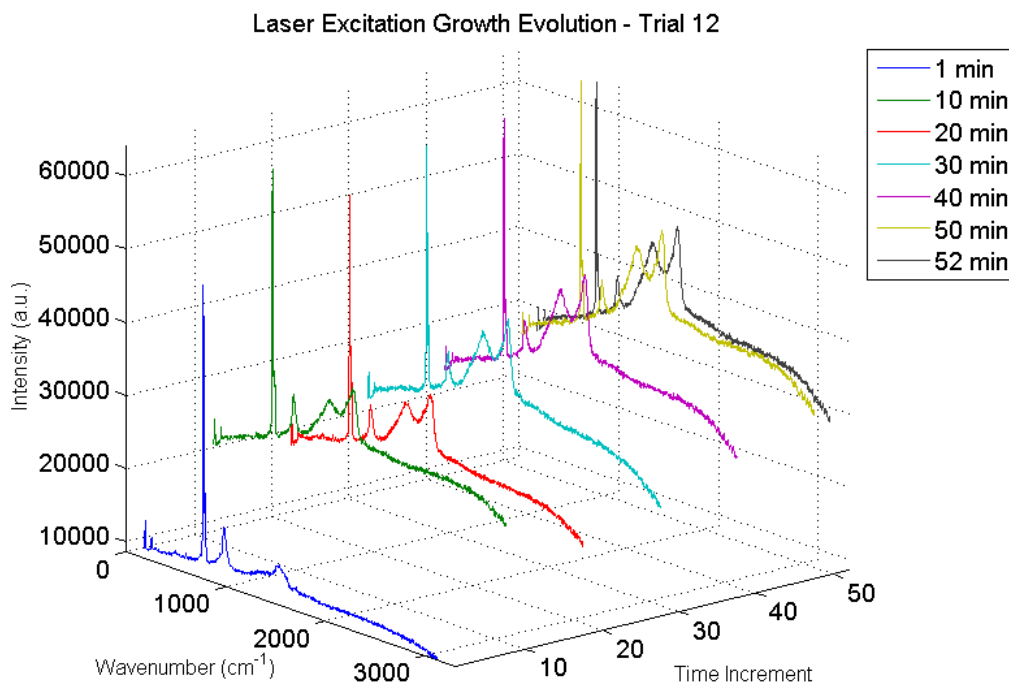
Figure 45 – Laser excitation growth of Trial 12.
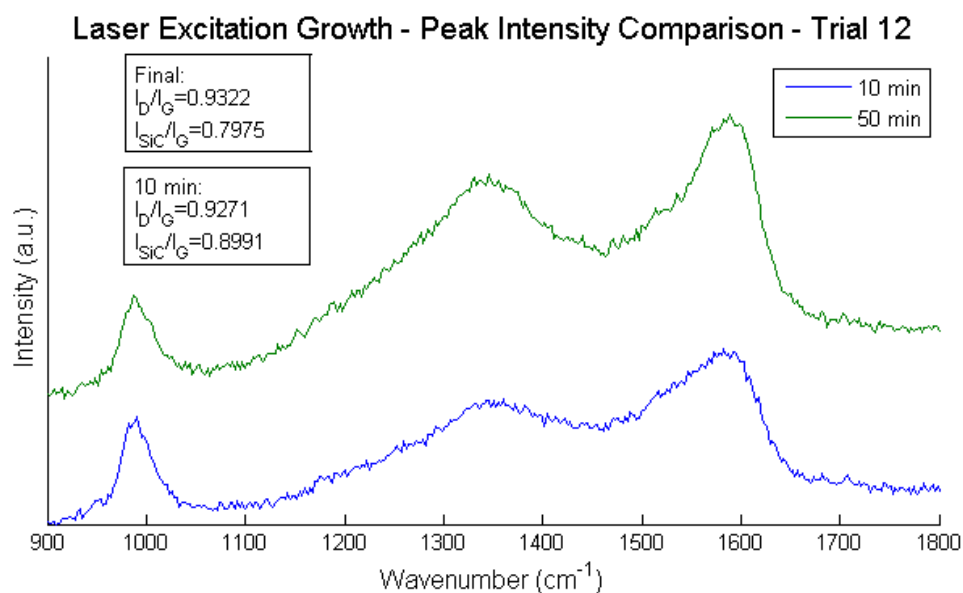
Figure 46 – Comparison of 10 min and final spectra of Trial 12.

Of the 13 laser excitation experiments conducted, Trial 6 has the lowest growth

value (I_{SiC}/I_G = 0.6985), which indicates the largest amount of carbon material present.

Raman data collected from Trial 6 is displayed in Figure 47. Trial 6 is different than the other experiments in that Ar gas was introduced to the system at a pressure of 8 x 10^{-4} Torr; which is two orders of magnitude greater than the other trials discussed thus far. According to previous research [21], [23], [27], [45]–[47], the applied Ar back-pressure limits the rate at which silicon atoms are released from the bulk SiC, which in-turn, varies the growth rate of carbon nanostructures. In this case, the increase of pressure, in addition to the introduction of Ar, provides an ideal environment for nanostructure production in the ARES system. A comparison of initial and final Raman spectra for Trial 6 is presented in Figure 48 which shows the D and G band intensities begin and finish with the same ratios ($I_D/I_G = 0.9234$ at 10 and 100 min).

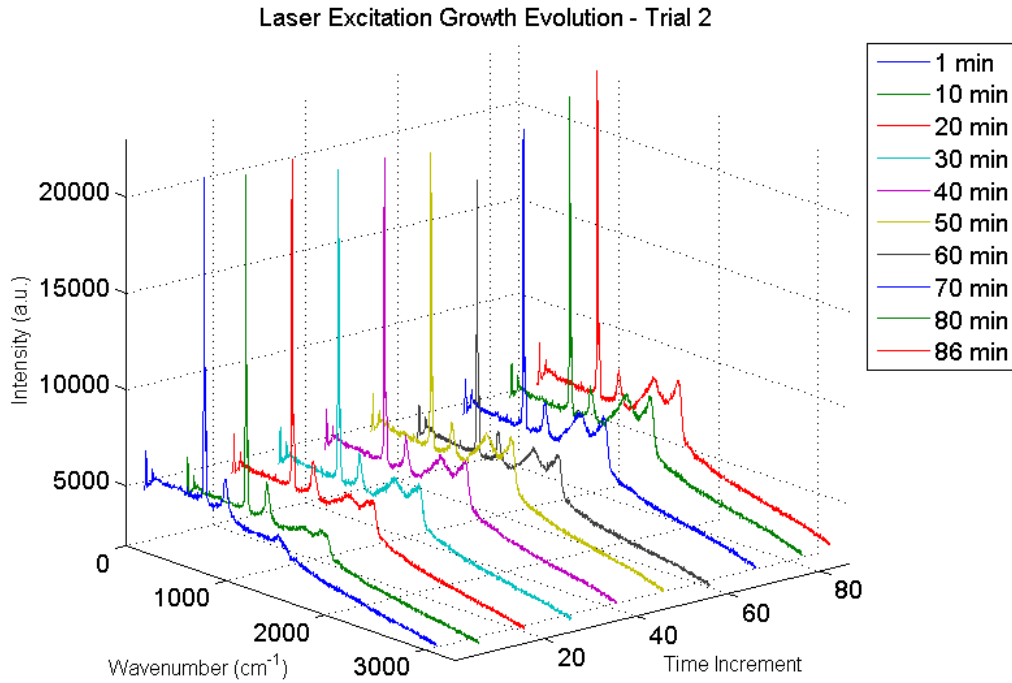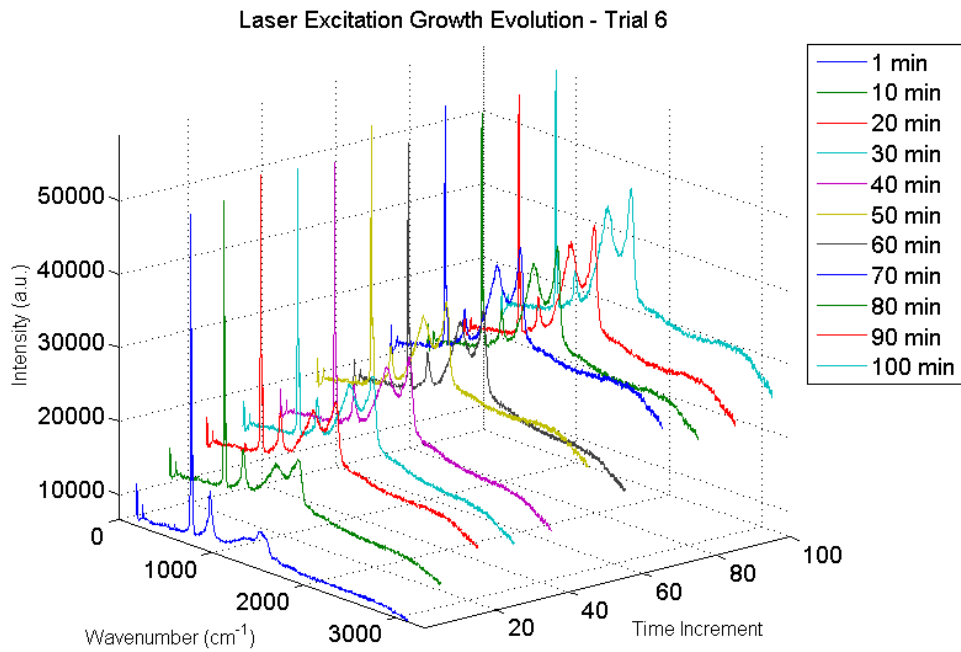

Figure 47 – Laser excitation growth of Trial 6.
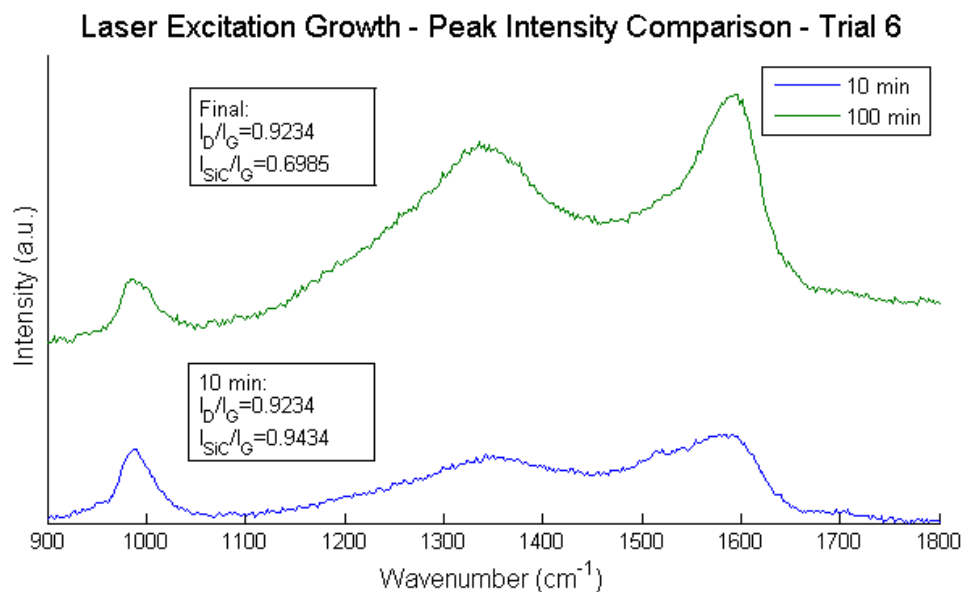
Figure 48 – Comparison of 10 min and final spectra of Trial 6.

4.4 Raman Spectrum Comparison

From comparing Raman data collected during this research to spectra found in reported literature, it is concluded that the material grown in the Oxy-Gon furnace is multi-wall carbon nanotubes (MWCNTs). Figure 49 displays a Raman spectrum from Torres *et al.* [48], whereby they produced MWCNTs via CVD. Raman data presented by other research teams ([49]–[51]) report similar MWCNT spectra.
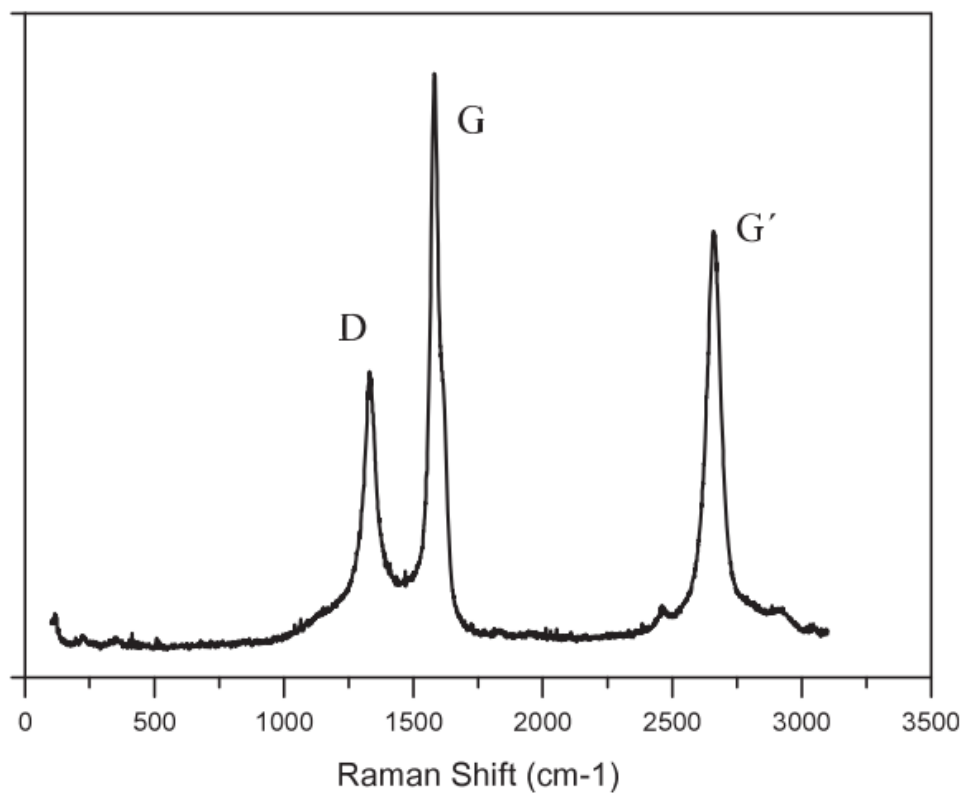
Figure 49 – Raman spectra of MWCNT obtained from micro-Raman Horiba instrument with a He–Ne laser emitting at 632.8 nm wavelength [48].

V. Conclusions and Recommendations

5.1 Chapter Overview

The purpose of this research is to utilize the laser-induced growth technique to investigate growth parameters of bulk nanostructure films. This work reports the results and findings for various parameter sets implemented during growth runs, and provides insight into the physical mechanism influencing the growth process. In this work, the background vacuum pressure and temperature used in the decomposition process were varied to investigate their impact on the type and quality of carbon allotrope formed on the SiC substrate.

5.2 Conclusions of Research

The first approach investigated was the Oxy-Gon graphite resistance furnace. Post-growth characterization of this method was performed using both SEM and Raman spectroscopy. SEM results showed the nanostructure material was present on all surfaces (pillar tops and etched surfaces). Material thickness was measured with SEM software tools and a growth rate of 100 nm per hour was reported. Post-growth Raman spectroscopy results suggested carbon nanohorns were produced beneath a layer of graphitic material. This finding provides a more precise description of the type of nanotubes grown in the Oxy-Gon furnace.

The second growth approach used a high-intensity laser to apply heat to a micro-meter scale spot size on the SiC substrate. Data collected from these experiments suggested etched SiC surfaces degraded by micro-masking proved ideal to grow nanomaterial. SiC pillars with smooth tops did not heat up enough to initiate

nanostructure growth. Allowing SiC to obtain jagged surface features from the RIE process proved critical in growing carbon nanostructures. Further Raman data showed there were no graphitic layers present in the resulting material. An absence of the G' peak proves this point.

Comparing the Raman spectra from the two growth methods reveals dissimilar materials are produced. This finding is evidenced by the absence of the G' peak in the laser excitation data. The 30 min soft bake process allows the SiC sample to grow nanocaps which are believed to be necessary in CNT growth. It is during this soft bake process that layers of graphitic material are produced. Due to the instantaneous heating of the SiC wafer by the laser, the ARES method bypasses the soft bake process. Since there is no soft bake process, layers of graphene are not produced, yet there must be a mechanism to grow nanocaps to facilitate CNT growth. From this conclusion, a question on the growth method is formulated. If nanocaps are not formed in the ARES system, then what process initiates the growth of the nanostructures?

5.3 Recommendations for Future Research

This research effort added to the data set of carbon nanomaterials grown via thermal decomposition of SiC. Though this growth method successfully produced material utilizing two different systems, there is more knowledge to be gained from further research. The SiC pillar diameter, for example, can be explored to determine what size generates the most heat. It is assumed the smaller the volume the laser has to excite, the higher the resulting temperature will be. Laser power can be investigated in an attempt to duplicate the soft bake growth conditions in order to grow graphitic

77

material on the SiC substrate. While this work ignored the presence of oxygen from the growth mechanics, this variable can be explored to further understand the effect it has on nanostructure growth.

Appendix A: Growth Methods of Nanotubes

Introduction

There are four effective methods of growing CNTs: laser ablation, carbon arc-discharge, chemical vapor deposition (CVD), and thermal decomposition of silicon carbide (SiC). The first two methods produces randomly oriented CNTs, and the third method produces CNTs mixed with a large amount of carbon nanocapsules and amorphous particles [26]. In order to grow CNTs free of impurities the fourth method can be considered; thermal decomposition of SiC.

The following paragraphs discuss the growth mechanisms behind four of the CNT growth techniques. The first section of this chapter discusses the history behind the discovery of the carbon nanotubes. The subsequent sections provide an overview of popular growth techniques used in the past. A total of four techniques are reviewed, with the final technique being the one that was used to grow nanostructures in this research effort.

History of Carbon Nanostructures

The history of the CNT begins in 1985 with work completed by Harry Kroto of the University of Sussex and Richard Smalley of Rice University. Kroto and Smalley were experimenting with carbon plasma, trying to duplicate environments found in outer space. While analyzing their data, they stumbled upon molecules consisting of exactly 60 carbon atoms [8]. Further experiments determined a spherical structure, leading to the conclusion that carbon 60 (C_{60}) is made of 12 pentagons and 20 hexagons arranged to form a truncated icosahedron [6], much like an American soccer ball. They named this molecule Buckminsterfullerene in honor of Richard Buckminster Fuller who is a noted

architect known for his use of geodesic domes, such as the Epcot Center at Disneyland [7].

In 1990, at a carbon-carbon composites workshop, Smalley proposed the existence of a tubular fullerene [7]. He envisioned a C_{60} molecule that could be made into a tube by elongating a C_{60} molecule. Sumio Iijima focused his research on that proposition [9] and in 1991 provided experimental evidence of the existence of carbon nanotubes [3]. Using transmission electron microscope (TEM) images of soot found in an arc discharge chamber, Iijima discovered what he believed to be concentric graphitic based tubes. One of his TEM images is shown below in Figure 50.
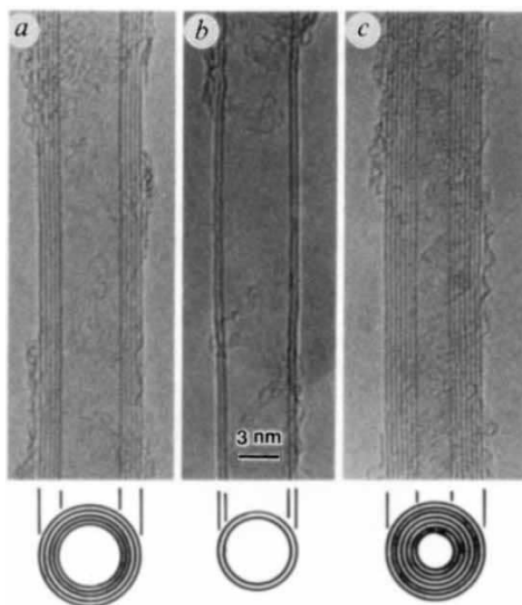
Figure 50 - TEM image of Iijima's CNT discovery showing the structure of multi-wall (a, c) and single-wall (b) CNTs [9].

Laser ablation

Laser ablation of carbon stock was the first method used to produce fullerenes of carbon. In 1985, Kroto and Smalley were blasting graphitic materials when they first

discovered molecules comprised completely of carbon [8]. As illustrated in Figure 51 below, an intense pulse of laser light is directed on a carbon surface in a stream of helium gas. The evaporated material condenses on a cold collector rod which collects the fullerenes. In order to achieve CNTs, a metal catalyst must be incorporated into the carbon target.
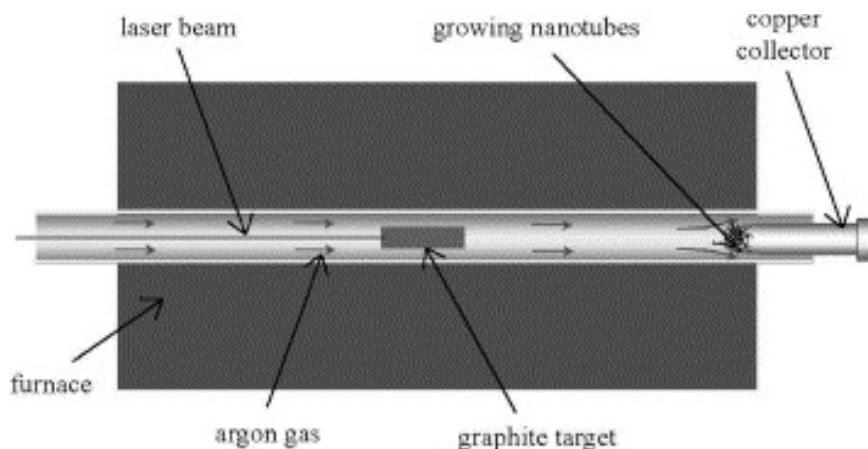
Figure 51 - The laser ablation method is shown above [7].

This method demands high energy consumption which makes it less than ideal for mass production. It also yields randomly oriented CNTs collected on the cold rod. In order to collect samples from this technique, CNTs must be scraped off the collecting rod and processed to remove any impurities and amorphous material left behind from the metal catalyst [6]. Another method that uses a metal catalyst is the carbon arc discharge method.

Arc discharge

After discovering the CNTs found from the laser ablation technique, researchers simplified the process and developed the arc discharge method to produce carbon nanomaterial. In a process similar to the laser ablation method, a piece of carbon stock is energized in a pressurized environment, and to ensure proper CNT growth, a metal

catalyst must be introduced to the carbon stock. As illustrated in Figure 52 below, an

anode and cathode are placed in a vacuum chamber. High electrical current arcs between

the two terminals and CNTs are formed on the cathode. A consistent air gap of a few

centimeters is required for proper CNT growth. While the anode loses material during

this process, the linear motion feedthrough system moves the anode closer to the cathode

maintaining a continuous growth process.
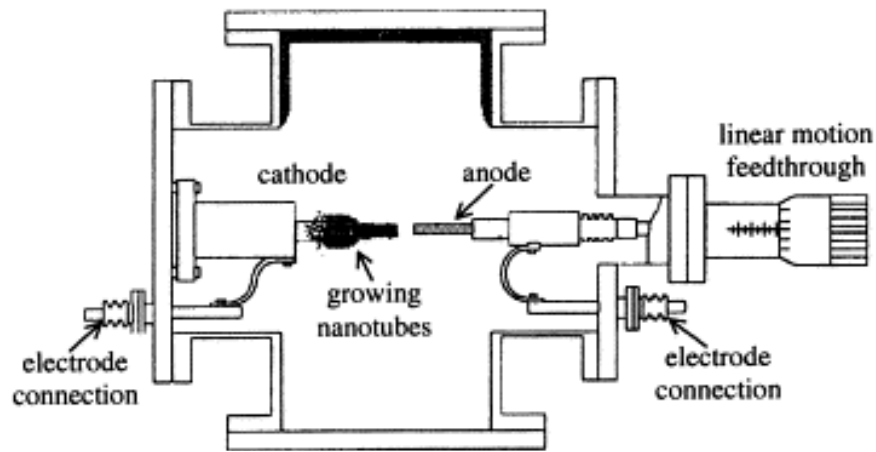
Figure 52 - The arc discharge method is illustrated above. A high current arcs from the
anode to the cathode. The cathode is attached to a carbon block incorporated with a
metal catalyst [7].

This method produces highly unorganized CNT formations found only at the base

of the cathode. The entire inside of the chamber is coated with amorphous carbon and

metallic particles. Much like the laser ablation technique, the CNTs produced must be

further processed in order to use them for nanostructure applications. One method that

requires much less processing is the growth of CNTs via CVD.

Chemical vapor deposition

Fundamentally different from plasma-based synthesis, CVD relies on thermal

energy only and an active catalyst such as iron, nickel, or cobalt. The metal catalyst

breaks down the carbon feedstock to produce CNTs. As shown in Figure 53 below,

gaseous carbon feedstock is flowed over transition metal nanoparticles at medium to high temperature (550 to 1200˚C) and reacts with the nanoparticles to produce CNTs [6].
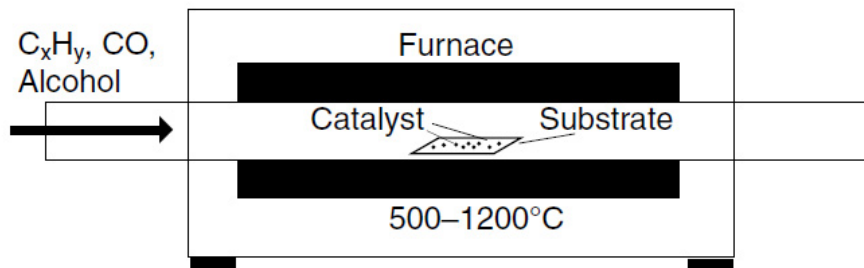
Figure 53 - Schematic of a CVD furnace.

Similar to the laser ablation and arc discharge methods described above, the CNTs produced by the CVD method contain metallic impurities which interfere with electrical and mechanical properties. In order for CNTs to have the opportunity to reach their theoretical limits of electrical and mechanical properties, they must be free of metallic impurities. One such method is available and is no more complicated than the other methods previously described, thermal decomposition of silicon carbide.

Thermal decomposition

Thermal decomposition of SiC is a fairly new method of growing CNTs. M. Kusunoki first discovered this technique in 1998 [25]. In this process, illustrated in Figure 54, a silicon carbide wafer is heated beyond the melting point of silicon (> 1414°C) in a vacuum chamber. Then, as the wafer maintaining its temperature (1500 – 1700°C), the carbon atoms left in the wafer self-assemble to form CNTs. This technique is also capable of forming graphene by varying the temperature and pressure of the chamber.

ARES Schematic
(Adaptive Rapid Experimentation & in-situ Spectroscopy)

Raman Spectrometer

Laser Growth Conditions
- Chamber pressure: 10^{-5} Torr
- Laser power: 2.5 W
- Excitation time: 60 min

532 nm Laser

40 x

Gases In

Vacuum

XYZ Translation

Vacuum Chamber

SiC Wafer

- Grow nanostructures via thermal decomposition of SiC
- Collect Raman spectra in-situ
- Obtain growth kinetics
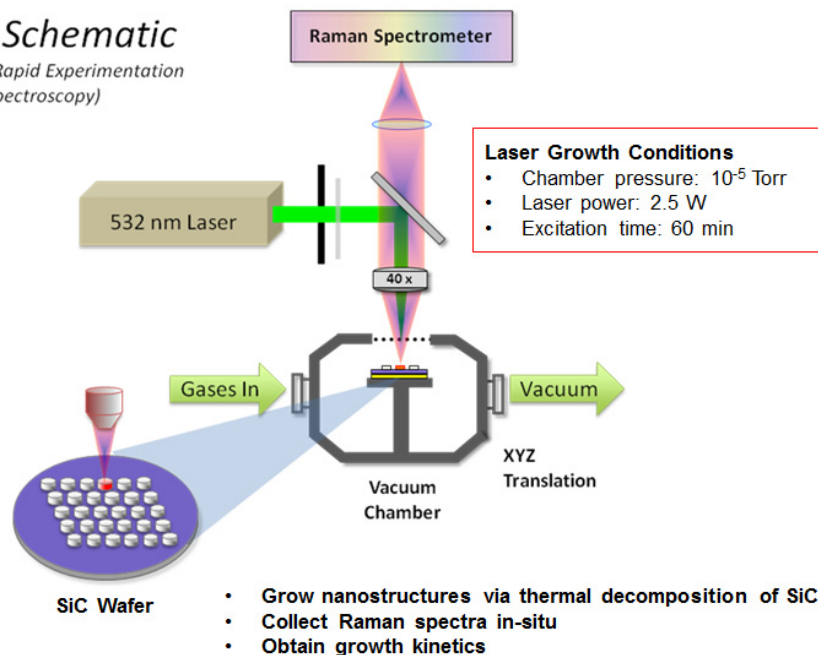
Figure 54 – ARES schematic, showing in situ Raman spectroscopy to study kinetics of carbon nanotube growth. Pillars of silicon carbide are heated using laser pulse to grow nanotubes. The same laser beam is also used to perform in-situ Raman spectroscopy [4].

Unlike the first three methods described above, this technique does not require a metal catalyst. Therefore, CNTs free of metal impurities are formed, and very little processing needs to be accomplished. This method does not consume any more time or energy than the others. CNTs produced by the thermal decomposition method will be used in this research effort. The ability to perform in-situ Raman spectroscopy is another benefit of using this method.

Summary

Several growth methods have been introduced in this literature review. They each have their pros and cons. However, since thermal decomposition of SiC does not require a metal catalyst, and therefore will produce nanostructures free of metal impurities, I will use this method during my research. This method is even more beneficial towards this

research effort in that it has the capability to grow both CNTs and graphene. I have yet to find another growth method with this capability.   Changing from growing CNTs to graphene will only require a change in chamber pressure, a change in growth temperature, and a change in gas flow.

Appendix B: Background material on reactive ion etching

Patterning semiconductor materials can be accomplished in two primary ways: wet etching and dry etching. Wet, or chemical, etching requires a corrosive liquid (typically an acid) to chemically react with the surface to be etched. When used with appropriate masking materials, chemical etching exhibits minimal surface damage and isotropic profiles [52]. Dry, or physical, etching requires a high velocity object to impact a surface in order to physically remove material, much like a chisel on cement. When accompanied by appropriate masking material, physical etching may exhibit high bombardment-induced damage to the surface (roughness), and anisotropic profiles [52].

Reactive ion etching, also known as plasma etching, uses a physical method to assist chemical etching or creates reactive ions to participate in chemical etching [52]. A plasma is an ionized gas composed of equal numbers of positive and negative charges and a different number of un-ionized molecules [53]. Plasma etching is based on the generation of plasma in a gas at low pressure. Chemical reactions occur between chamber gasses and the material to be etched, weakening the material, allowing for an easier physical removal. A strong physical force from the charged particles within the plasma impacts the surface, much like a chisel, removing particles from the material [54]. RIE results in moderate etch rates, moderate selectivity, varying bombardment-induced damage, and anisotropic etch profiles. The anisotropic profiles create straight, vertical walls, ideal for pillars required in many device designs. For details behind the mechanics of plasma etching, May and Sze [52] provide a good explanation:

"Plasma etching proceeds in five steps. First, the etchant species is generated in the plasma. The reactant is then transported by diffusion through a stagnant gas layer to the surface. Next, the reactant is adsorbed on the surface. A chemical reaction (along

with physical effects such as ion bombardment) follows to form volatile compounds. Finally, the compounds are desorbed from the surface, diffused into the bulk gas, and pumped out by the vacuum system [52]"

Etching SiC can be performed by wet or by dry techniques. While both processes have their advantages, the preferred method of etching SiC is by means of a reactive plasma for two key reasons. First, plasma etching of SiC can be performed at room temperature. Wet chemical etching of SiC requires an alkaline solution to be heated to > 600°C [55]. The chemical stability of SiC lends to its resistance to chemical etching [56]. Second, and more importantly, plasma etching results in anisotropic etch patterns which are ideal for controlling feature sizes at the sub-micron level. One drawback to using plasma to etch SiC is that a significant amount of micro-masking can occur, resulting in a relatively rough surface in areas where the material has been etched away. Commonly, the source of this micro-masking effect arises from either the aluminum cathode in the RIE apparatus [57], or the metallic masking layer on the substrate re-depositing on the surface.

In order to use plasma to etch a substrate, a masking layer is utilized to create device features on the substrate. A Ni masking layer is used in this research effort because of its high density (8908 kg/m^3 [58]) and ease to sputter on SiC. During the reactive ion etching, however, the Ni masking layer is pulverized by the ions, and re-deposits on the SiC substrate. This micromasking effect creates a rough, pitted surface on the substrate. One way to avoid this effect is to use a different masking layer.
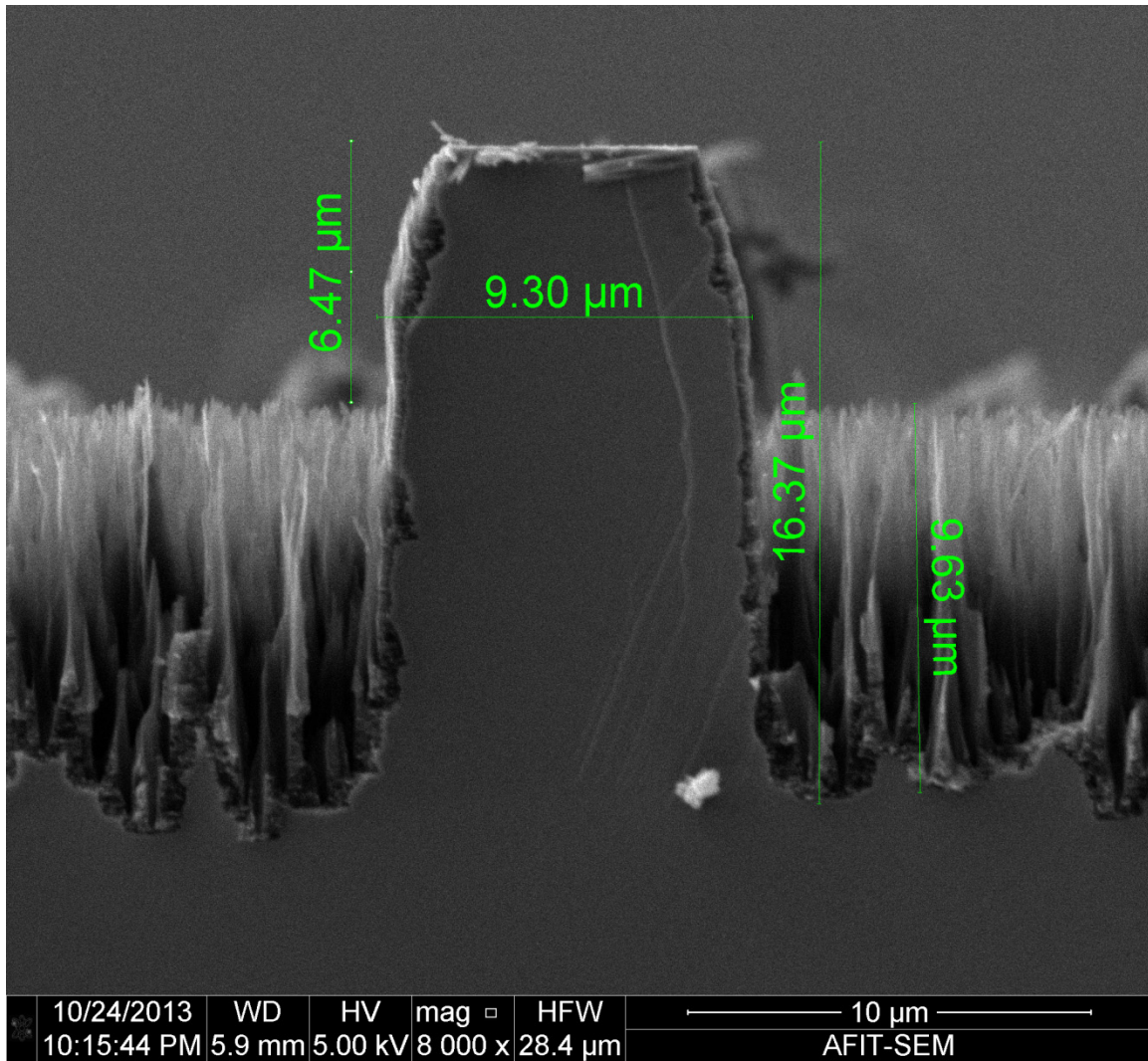
Figure 55 – Cross-section SEM image of a fabricated SiC pillar. The jagged features are a result of the micro-masking effect and create a variation in the height of the pillars ranging from 6 – 16 μm.

Residue free etching of SiC can be obtained in several ways: cover the Al electrode with graphite, introduce hydrogen to the gas mix as evidenced by Yih [57], or by using a non-metallic mask such as aluminum nitride (AlN) as shown by Senesky [59]. Using these techniques, however, may result in slower etch times.

It has been shown by Senesky [59] that aluminum nitride (AlN) (density = 3255 kg/m^3 [58]) can be used as a masking layer. Also, according to Yih [57]: Very limited

information has been reported on SiC etching in chlorine-based plasmas, which has the potential for using non-metallic etch mask materials (e.g. SiO_2) and obtaining residue – free etching. SiC etching in fluorine-based high density electron cyclotron resonance (EDR) plasma was reported recently with promising results for high etch rate, anisotropic profile, and residue-free (smooth) surface topography.

Appendix C: Oxy-Gon Furnace Operating Procedure

The following steps are performed using AFRL/RXAN's Oxy-Gon graphite resistance heating furnace to decompose the SiC samples to form CNTs (courtesy of Dr. John Boeckl, AFRL/RXAN)

System Start-up (process selection switch in STANDBY):
1. Verify house compressed air supply is open (the vent and vacuum valves are air pressure activated).
2. Turn ON the Main Power switch (the handle is on the lower front of the main panel).
3. Turn ON the Roughing Pump (green button). The Roughing Pump will pull on the turbo-molecular pump – to ~ 10^{-3} Torr on TC1 (approx. 15 min).
4. Turn ON the ion gauge controller to read TC1 (the left switch on the gauge panel).
5. Turn ON the turbo-molecular (green button); it will pull on itself.
6. If the chamber is under vacuum, turn the process selection switch to VENT GAS, otherwise go to step 8.
7. Turn ON the low-N_2 tank and regulator; open the ball valve on the furnace to 25 to vent the chamber and allow it to open.
8. When the chamber vents, turn OFF the low-N_2 tank and regulator.
9. OPEN the chamber, load the samples on the graphite cylinder, and secure the chamber door.

Chamber Evacuation Process:
10. Turn the process selection switch to STANDBY; then to ROUGH.
11. Run the roughing pump until chamber is in the mid 10^{-2} Torr range (read TC2); this will take several minutes, and the pressure will slightly increase at TC1 (~15 min).
12. Turn process selection switch to HI VACUUM; turbo-molecular pump will pull on the chamber, roughing pump pulls on the turbo-molecular pump; TC2 will drop quickly; TC1 increases, then drops more slowly.
13. Turn ON the ion gauge filament when TC2 is in the 10^{-3} Torr range. Continue pumping until it is in the ~ 10^{-4} Torr range (note: ion gauge will not light if the pressure is too high).
14. OPEN the H_2O outlet and inlet hand valves (note: do this only if the chamber is under vacuum or filled with an inert gas).
15. Ensure the yellow H_2O handles are open and that the flow meters are turning.
16. Turn ON Heat Zone (green button).

Nanocap Formation Process (Soft Bake):
17. Ramp up Heat Zone to 1250°C by setting A to 33% (adjust power controller by pressing AUTO/MAN and directional arrow simultaneously; adjust A when ~ 10°C below target value).
18. Decompose samples for 30 minutes (adjust AUTO/MAN controller as needed).

Decomposition Process:

19. Ramp up AUTO/MAN power controller to obtain target temperature of 1700°C (set A to 39%; then adjust A when ~ 1690°C).
20. Decompose the sample for desired time (adjust AUTO/MAN controller as needed).
21. At the desired time, ramp down AUTO/MAN controller to 1%.
22. After 5 minutes into ramp down, set AUTO/MAN controller to 0%, and turn OFF the Heat Zone (red button).
23. When the temperature is ≤ 150°C, CLOSE the H_2O inlet and outlet hand valves. (note: chamber cools quicker with H_2O).
24. Turn OFF the ion gauge filament (same switch used to turn it on).
25. Turn ON the low-N_2 tank and regulator; open the ball valve on the furnace to 25.
26. Turn the process selection switch to VENT GAS to backfill the chamber.
27. When the chamber temperature is ~30°C, CLOSE the low-N_2 tank and regulator; OPEN the chamber; UNLOAD the samples; secure the chamber door.
28. If additional runs will be completed in the same day, load the new sample and return to step 10.

System Shutdown:

29. Turn process selection switch to STANDBY; then to ROUGH.
30. Turn ON the ion gauge controller to read TCs.
31. Run the roughing pump until TC2 reads ~10^{-2} Torr, then turn the process selection switch to HI VACUUM until TC2 reads ~10^{-3} Torr.
32. Turn the process selection switch to STANDBY; turn OFF the turo-molecular pump (red button).
33. Turn OFF the roughing pump (red button).

Bibliography

[1]   R. Serway and J. Jewett, *Principles of Physics: A Calculus-Gased Text, Volume 1*, 4th ed. Cengage Learning, 2005, p. 1150.

[2]   R. S. Muller, T. I. Kamins, and M. Chan, *Device Electronics for Integrated Circuits*, 3rd ed. New York: John Wiley & Sons, Ltd, 2003, p. 528.

[3]   A. K. Geim and K. S. Novoselov, "The rise of graphene.," *Nat. Mater.*, vol. 6, no. 3, pp. 183–191, 2007.

[4]   C. Lee and J. Harrison, "RXAN BOECKL FY14 LRIR PROPOSAL (Lee)." 2012.

[5]   M. T. Ahmadi, J. Karamdel, and R. Ismail, "Modelling of the Current-Voltage Characteristics of a Carbon Nano Tube Field Effect Transistor," in *ICSE 2008 Proc.*, 2008, vol. 7, no. 2, pp. 576–580.

[6]   M. J. O' Connell, *Carbon Nanotubes Properties and Applications Edited by*. Taylor & Francis Group, 2006.

[7]   P. Harris, *Carbon Nanotube Science: Synthesis, properties and applications*. Cambridge, 2009, p. 315.

[8]   H. W. Kroto, J. R. Heath, S. C. O'Brien, R. F. Curl, and R. E. Smalley, "C60: Buckminsterfullerene," *Nature*, vol. 318, pp. 162–163, 1985.

[9]   S. Iijima, "Helical microtubules of graphitic carbon," *Lett. to Nat.*, vol. 354, pp. 56–58, 1991.

[10]   M. Terrones, "SCIENCE AND TECHNOLOGY OF THE TWENTY-FIRST CENTURY : Synthesis, Properties, and Applications of Carbon Nanotubes," *Annu. Rev. Mater. Res.*, vol. 33, no. 1, pp. 419–501, Aug. 2003.

[11]   K. I. Bolotin, K. J. Sikes, Z. Jiang, M. Klima, G. Fudenberg, J. Hone, P. Kim, and H. L. Stormer, "Ultrahigh electron mobility in suspended graphene," *Solid State Commun.*, vol. 146, no. 9–10, pp. 351–355, Jun. 2008.

[12]   J.-H. Chen, C. Jang, S. Xiao, M. Ishigami, and M. S. Fuhrer, "Intrinsic and extrinsic performance limits of graphene devices on SiO2," *Nat. Nanotechnol.*, vol. 3, pp. 206–209, 2008.

[13]   M. S. Dresselhaus, G. Dresselhaus, and P. Avouris, *Carbon Nanotubes: Synthesis, Structure, Properties, and Applications*. 2001.

[14] P. G. Collins, "DEFECTS AND DISORDER IN CARBON NANOTUBES," in *Oxford Handbook of Nanoscience and Technology: Frontiers and Advances*, A. V. Narlikar and Y. Y. Fu, Eds. Oxford: Oxford University Press, 2009.

[15] R. Rao, D. Liptak, T. Cherukuri, B. I. Yakobson, and B. Maruyama, "In situ evidence for chirality-dependent growth rates of individual carbon nanotubes.," *Nat. Mater.*, vol. 11, no. 3, pp. 213–6, Mar. 2012.

[16] W. C. Mitchel, J. Boeckl, D. Tomlin, W. Lu, J. Rigueur, and J. Reynolds, "Growth of Carbon Nanotubes by Sublimation of Silicon Carbide Substrates," in *Quantum Sensing and Nanophotonic Devices II*, 2005, vol. 5732, pp. 77–83.

[17] M. C. Pochet, "CHARACTERIZATION OF THE FIELD EMISSION PROPERTIES OF CARBON NANOTUBE FILMS FORMED ON SILICON CARBIDE SUBSTRATES BY SURFACE DECOMPOSITION," Air Force Institute of Technology, 2006.

[18] J. Campbell, "FIELD EMISSION OF THERMALLY GROWN CARBON NANOSTRUCTURES ON SILICON CARBIDE," Air Force Institute of Technology, 2012.

[19] L. Latu-Romain, M. Ollivier, V. Thiney, O. Chaix-Pluchery, and M. Martin, "Silicon carbide nanotubes growth: an original approach," *J. Phys. D. Appl. Phys.*, vol. 46, no. 9, p. 092001, Mar. 2013.

[20] W. Lu, J. J. Boeckl, and W. C. Mitchel, "A critical review of growth of low-dimensional carbon nanostructures on SiC (0 0 0 1): impact of growth environment," *J. Phys. D. Appl. Phys.*, vol. 43, no. 37, p. 9, Sep. 2010.

[21] J. Boeckl, W. C. Mitchel, E. Clarke, R. L. Barbosa, and W. J. Lu, "Structural Evaluation of Graphene/SiC (0001) Grown in Atmospheric Pressure," *Mater. Sci. Forum*, vol. 645–648, pp. 573–576, Apr. 2010.

[22] R. Lv and M. Terrones, "Towards new graphene materials: Doped graphene sheets and nanoribbons," *Mater. Lett.*, vol. 78, pp. 209–218, Jul. 2012.

[23] R. Rao, N. Pierce, D. Liptak, D. Hooper, G. Sargent, S. L. Semiatin, S. Curtarolo, A. R. Harutyunyan, and B. Maruyama, "Revealing the Impact of Catalyst Phase Transition on Carbon Nanotube Growth by in Situ Raman Spectroscopy," *ACS Nano*, vol. 7, no. 2, pp. 1100–1107, 2013.

[24] F. Bechstedt and A. Belabbes, "Structure, energetics, and electronic states of III–V compound polytypes," *J. Phys. Condens. Matter*, vol. 25, no. 27, p. 273201, 2013.

[25] M. Kusunoki, T. Suzuki, K. Kaneko, and M. Ito, "Formation of self-aligned carbon nanotube films by surface decomposition of silicon carbide," *Philos. Mag. Lett.*, vol. 79, no. 4, pp. 153–161, 1999.

[26] M. Kusunoki, T. Suzuki, C. Honjo, H. Usami, and H. Kato, "Closed-packed and well-aligned carbon nanotube films on SiC," *J. Phys. D. Appl. Phys.*, vol. 40, no. 20, pp. 6278–6286, Oct. 2007.

[27] T. Maruyama and S. Naritsuka, "Initial Growth Process of Carbon Nanotubes in Surface Decomposition of SiC," in *Carbon Nanotubes - Synthesis, Characterization, Applications*, no. 1, S. Yellampalli, Ed. Intech Open, 2011, pp. 29–46.

[28] Y. Song and F. W. Smith, "Phase diagram for the interaction of oxygen with SiC," *Appl. Phys. Lett.*, vol. 81, no. 16, p. 3061, 2002.

[29] W. a de Heer, C. Berger, M. Ruan, M. Sprinkle, X. Li, Y. Hu, B. Zhang, J. Hankinson, and E. Conrad, "Large area and structured epitaxial graphene produced by confinement controlled sublimation of silicon carbide.," *Proc. Natl. Acad. Sci. U. S. A.*, vol. 108, no. 41, pp. 16900–5, Oct. 2011.

[30] J. Boeckl, W. C. Mitchel, W. J. Lu, and J. Rigueur, "Structural and Electrical Characteristics of Carbon Nanotubes Formed on Silicon Carbide Substrates by Surface Decomposition," *Mater. Sci. Forum*, vol. 527–529, pp. 1579–1582, 2006.

[31] M. H. Rummeli, P. Ayala, and T. Pichler, "Carbon Nanotubes and Related Structures : Production and Formation," in *Carbon Nanotubes and Related Structrues*, D. Guldi and N. Martin, Eds. Weinheim: Wiley-VCH Verlag GmbH & Co., 2010.

[32] M. H. Rümmeli, A. Bachmatiuk, F. Börrnert, F. Schäffel, I. Ibrahim, K. Cendrowski, G. Simha-Martynkova, D. Plachá, E. Borowiak-Palen, G. Cuniberti, and B. Büchner, "Synthesis of carbon nanotubes with and without catalyst particles.," *Nanoscale Res. Lett.*, vol. 6, no. 1, p. 303, Jan. 2011.

[33] D. J. Gardiner, *Practical Raman Spectroscopy*. Springer - Verlag, 1989, p. 276.

[34] W. E. Smith and G. Dent, "Introduction, Basic Theory and Principles," in *Modern Raman Spectrosopy - A Practical Approach*, vol. 5, John Wiley & Sons, Ltd, 2005, pp. 1–21.

[35] Y. Leng, *Materials Characterization: Introduction to Microscopic and Spectroscopic Methods*. Singapore: John Wiley & Sons, Ltd, 2008, p. 337.

[36] J. R. Ferraro, K. Nakamoto, and C. W. Brown, *Introductory Raman Spectroscopy*. Academic Press, 2003, p. 434.

[37] L. G. Cancado, A. Jorio, E. H. M. Ferreira, F. Stavale, C. A. Achete, R. B. Capaz, M. V. O. Moutinho, A. Lombardo, T. S. Kulmala, and A. C. Ferrari, "Quantifying Defects in Graphene via Raman Spectroscopy at Different Excitation Energies," *Nano Lett.*, vol. 11, pp. 3190–3196, 2011.

[38] M. S. Dresselhaus, a. Jorio, and R. Saito, "Characterizing Graphene, Graphite, and Carbon Nanotubes by Raman Spectroscopy," *Annu. Rev. Condens. Matter Phys.*, vol. 1, no. 1, pp. 89–108, Aug. 2010.

[39] a. C. Ferrari, J. C. Meyer, V. Scardaci, C. Casiraghi, M. Lazzeri, F. Mauri, S. Piscanec, D. Jiang, K. S. Novoselov, S. Roth, and a. K. Geim, "Raman Spectrum of Graphene and Graphene Layers," *Phys. Rev. Lett.*, vol. 97, no. 18, p. 187401, Oct. 2006.

[40] D. S. Lee, C. Riedl, B. Krau, K. Von Klitzing, U. Starke, J. H. Smet, M. Festkörperforschung, and D.- Stuttgart, "Raman spectra of epitaxial graphene on SiC and of epitaxial graphene transferred to SiO 2," *Nano Lett.*, vol. 8, no. 12, pp. 4320–4325, 2008.

[41] R. Saito, M. Hofmann, G. Dresselhaus, and A. Jorio, "Raman spectroscopy of graphene and carbon nanotubes," *Adv. Phys.*, vol. 60, no. July, pp. 413–550, 2011.

[42] R. B. Weisman and S. Subramoney, "Carbon Nanotubes," *Electrochem. Soc. Interface*, vol. Summer, no. Cvd, pp. 42–46, 2006.

[43] "UM Chemistry - Tech Services - Raman Spectroscopy." [Online]. Available: http://www.umich.edu/~techserv/raman/.

[44] "Micro and Nanotechnology Laboratory at University of Illinois." [Online]. Available: http://mntl.illinois.edu/equipment/raman.htm.

[45] M. Balat, G. Flamant, G. Male, and G. Pichelin, "Active to passive transition in the oxidation of silicon carbide at high temperature and low pressure in molecular and atomic oxygen," *J. Mater. Sci.*, vol. 27, pp. 697–703, 1992.

[46] R. Püsche, M. Hundhausen, and L. Ley, "Temperature induced polytype conversion in cubic silicon carbide studied by Raman spectroscopy," *J. Appl. Phys.*, vol. 96, no. 10, pp. 5569–5575, 2004.

[47] W. Wesch, "Silicon carbide: synthesis and processing," *Nucl. Instruments Methods Phys. Res. B*, vol. 116, pp. 305–321, 1996.

[48]   C. Torres-Torres, N. Peréa-López, H. Martínez-Gutiérrez, M. Trejo-Valdez, J. Ortíz-López, and M. Terrones, "Optoelectronic modulation by multi-wall carbon nanotubes.," *Nanotechnology*, vol. 24, no. 4, p. 045201, Feb. 2013.

[49]   M. Zdrojek, W. Gebicki, C. Jastrzebski, T. Melin, and A. Huczko, "Studies of multiwall carbon nanotubes using Raman spectroscopy and atomic force microscopy," *Solide State Phenom.*, vol. 99, no. 265, pp. 2–5, 2004.

[50]   A. Mathur, M. Tweedie, S. S. Roy, P. D. Maguire, and J. a McLaughlin, "Electrical and Raman spectroscopic studies of vertically aligned multi-walled carbon nanotubes.," *J. Nanosci. Nanotechnol.*, vol. 9, no. 7, pp. 4392–6, Jul. 2009.

[51]   E. F. Antunes, a. O. Lobo, E. J. Corat, and V. J. Trava-Airoldi, "Influence of diameter in the Raman spectra of aligned multi-walled carbon nanotubes," *Carbon N. Y.*, vol. 45, no. 5, pp. 913–921, Apr. 2007.

[52]   G. S. May and S. M. Sze, *Fundamentals of Semiconductor Fabrication*, Internatio. New Delhi, India: John Wiley & Sons, Ltd, 2004.

[53]   Q.-Z. Luo, N. D'Angelo, and R. L. Merlino, "Shock formation in a negative ion plasma," *Phys. Plasmas*, vol. 5, no. 8, p. 2868, 1998.

[54]   T.-R. Hsu, *MEMS & Microsystems Design, Manufacture, and Nanoscale Engineering*, 2nd ed. Wiley, 2008, p. 576.

[55]   J. Sugiura, W. J. Lu, K. C. Cadien, and A. J. Steckl, "RIE of SiC-1985.pdf," *J. Vac. Sci. Technol.*, vol. 4, no. Jan/Feb, pp. 349–354, 1985.

[56]   N. O. V. Plank, M. A. Blauw, and E. W. J. M. van der Drift, "The etching of silicon carbide in inductively coupled SF 6 / O 2 plasma," *J. Phys. D. Appl. Phys.*, vol. 36, pp. 482–487, 2003.

[57]   P. H. Yih, V. Saxena, and A. J. Steckl, "A Review of SiC Reactive Ion Etching in Fluorinated Plasmas," *Phys. Status Solidi*, vol. 202, no. 1, pp. 605–642, 1997.

[58]   M. Winters, "WebElements: the periodic table on the WWW," *The University of Sheffield*, 2013. [Online]. Available: http://webelements.com. [Accessed: 12-Jun-2013].

[59]   D. G. Senesky and A. P. Pisano, "Aluminum Nitride as a Masking Material for the Plasma Etching of Silicon Carbide Structures," in *2010 IEEE 23rd International Conference on MEMS*, 2010, pp. 352–355.

REPORT DOCUMENTATION PAGE

The public reporting burden for this collection of information is estimated to average 1 hour per response, including the time for reviewing instructions, searching existing data sources, gathering and maintaining the data needed, and completing and reviewing the collection of information. Send comments regarding this burden estimate or any other aspect of the collection of information, including suggestions for reducing this burden to Department of Defense, Washington Headquarters Services, Directorate for Information Operations and Reports (0704-0188), 1215 Jefferson Davis Highway, Suite 1204, Arlington, VA 22202-4302. Respondents should be aware that notwithstanding any other provision of law, no person shall be subject to an penalty for failing to comply with a collection of information if it does not display a currently valid OMB control number.
PLEASE DO NOT RETURN YOUR FORM TO THE ABOVE ADDRESS.

1. REPORT DATE (DD-MM-YYYY)	2. REPORT TYPE	3. DATES COVERED (From – To)
27-03-2014	Master's Thesis	May 2012 – March 2014

TITLE AND SUBTITLE	5a. CONTRACT NUMBER
Carbon Allotrope Dependence on Temperature and Pressure During Thermal Decomposition of Silicon Carbide	5b. GRANT NUMBER
	5c. PROGRAM ELEMENT NUMBER

6. AUTHOR(S)	5d. PROJECT NUMBER
Anderson, Munson J., Captain, USAF	5e. TASK NUMBER
	5f. WORK UNIT NUMBER

7. PERFORMING ORGANIZATION NAMES(S) AND ADDRESS(S)	8. PERFORMING ORGANIZATION REPORT NUMBER
Air Force Institute of Technology Graduate School of Engineering and Management (AFIT/ENY) 2950 Hobson Way, Building 640 WPAFB OH 45433-8865	AFIT-ENG-14-M-07

9. SPONSORING/MONITORING AGENCY NAME(S) AND ADDRESS(ES)	10. SPONSOR/MONITOR'S ACRONYM(S)
Air Force Research Laboratory, Materials and Manufacturing Directorate Attn: Dr. John J. Boeckl 3005 Hobson Way, Bldg 651 WPAFB OH 45433-7707 DSN: 785-4474 x3219 John.boeckl@wpafb.af.mil	AFRL/RXAN
	11. SPONSOR/MONITOR'S REPORT NUMBER(S)

12. DISTRIBUTION/AVAILABILITY STATEMENT
DISTRUBTION STATEMENT A. APPROVED FOR PUBLIC RELEASE; DISTRIBUTION UNLIMITED.

13. SUPPLEMENTARY NOTES
This material is declared a work of the U.S. Government and is not subject to copyright protection in the United States.

14. ABSTRACT
Bulk CNT and graphene films form on SiC using a metal-catalyst-free thermal decomposition approach. In this work, the background vacuum pressure and temperature used in the decomposition process are varied to investigate their impact on the type and quality of carbon allotrope formed on the SiC substrate. The carbon nanostructure growth is performed using two approaches, both of which involve intense heating ($1400\text{-}1700^\circ$C) of SiC under moderate vacuum conditions ($10^{-2} - 10^{-5}$ Torr). The first growth method uses a conventional graphite resistance furnace capable of annealing wafer-scale samples over 1700°C under vacuum. Using this approach, post-growth characterization is performed using both SEM and Raman spectroscopy. The second growth approach heats an illuminated area of the SiC substrate under vacuum conditions, resulting in a micro-meter scale growth process. Unique to this micro-scale approach is that in-situ Raman spectroscopy is performed yielding instantaneous characterization of the resultant carbon nanostructure. This work focuses on using the laser-induced growth technique to refine ideal growth parameters of bulk nanostructure films. This work reports results and findings for various parameter sets implemented during growth, providing insight into the physical mechanism of the growth process.

15. SUBJECT TERMS
Silicon carbide, carbon nanotubes, thermal decomposition, Raman, graphene

16. SECURITY CLASSIFICATION OF:			17. LIMITATION OF ABSTRACT	18. NUMBER OF PAGES	19a. NAME OF RESPONSIBLE PERSON
a. REPORT	b. ABSTRACT	c. THIS PAGE			Maj Michael Pochet, AFIT/ENG
U	U	U	UU	113	19b. TELEPHONE NUMBER (Include area code) (937) 785-3636, ext 4393 Michael.pochet@afit.edu